CHALMERS
UNIVERSITY OF TECHNOLOGY

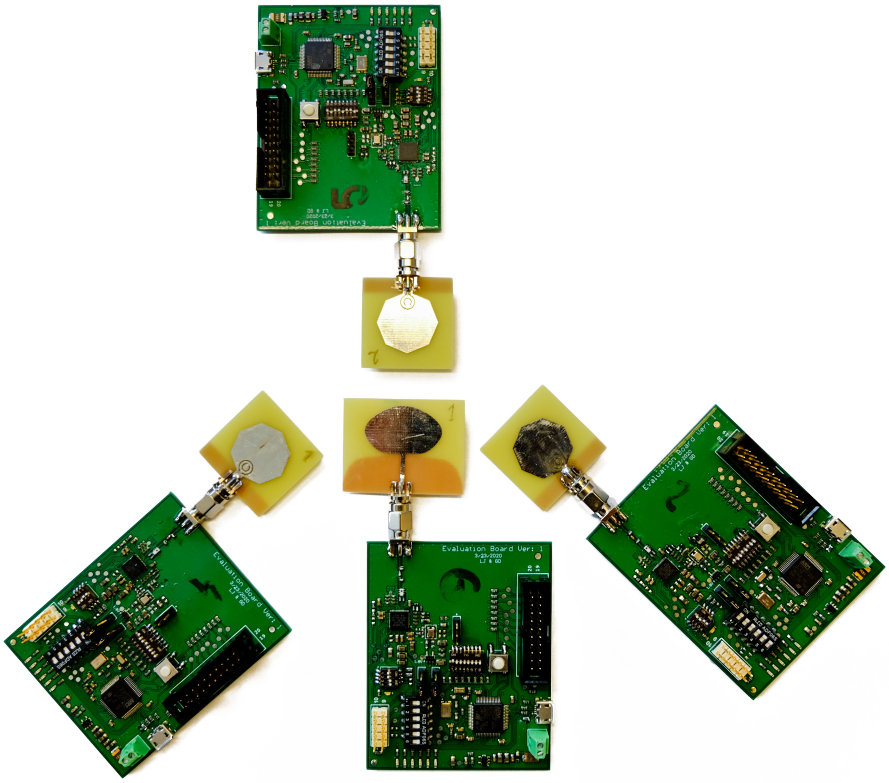

Impact of Hardware Components on the Precision of an UWB Positioning System

Master's thesis in Wireless, Photonics and Space Engineering

GUSTAF DAHL
LUDVIG JOHANSSON

Department of Space, Earth and Environment
CHALMERS UNIVERSITY OF TECHNOLOGY
Gothenburg, Sweden 2020

Master's thesis 2020

Impact of Hardware Components on the Precision of an UWB Positioning System

Gustaf Dahl
Ludvig Johansson

CHALMERS
UNIVERSITY OF TECHNOLOGY

Department of Space, Earth and Environment
Chalmers University of Technology
Gothenburg, Sweden 2020

Impact of Hardware Components on the Precision of an UWB Positioning System
Gustaf Dahl
Ludvig Johansson

Supervisor: Verner Ljung & Steinar Thorvaldsson, Syntronic
Examiner: Jan Johansson, Department of Space, Earth and Environment

Master's Thesis 2020
Department of Space, Earth and Environment
Chalmers University of Technology
SE-412 96 Gothenburg
Telephone +46 31 772 1000

Cover: UWB positioning system consisting of modular PCB units together with band-reject and reference antennas.

Typeset in LaTeX
Printed by Chalmers Reproservice
Gothenburg, Sweden 2020

Impact of Hardware Components on the Precision of an UWB Positioning System
Gustaf Dahl, Ludvig Johansson
Department of Space, Earth and Environment
Chalmers University of Technology

Abstract

The project of establishing the impact of hardware has on the precision of an UWB positioning system was approached with broad scope. Attempting to isolate the influence antennas- and oscillators has on the positioning precision requires a good understanding of the hardware setup for the complete system. An UWB positioning evaluation system was therefore designed and manufactured on PCBs, allowing it to be modified in order to test the system performance with different antennas and oscillators. Oscillators with three levels of frequency stability were chosen to be evaluated. Two patch antennas, one possessing high directivity and one featuring band-reject properties, were designed and manufactured as well. These components effect on precision were evaluated by performing positioning in both Line-Of-Sight (LOS)- and Non-Line-Of-Sight (NLOS) environments using different configurations of the hardware. The results of the tests were then evaluated using several metrics in an attempt to observe differences in the precision of the hardware configurations.

Due to limited testing and intrinsic uncertainties of the evaluation system no clear conclusions on the isolated impact of the antennas and oscillators could be made, nevertheless some trends could be identified. The results of the NLOS test indicate that the band-reject properties and increased frequency stability had a positive impact on precision. This effect was primarily demonstrated by the significant increase in the number of position estimates acquired, ranging from approximately 7 up to 30 estimates depending on the hardware configuration. The higher directivity antenna generated almost no position estimates in the NLOS test making it less suitable. The LOS tests produced similar results for most hardware configurations with a mean absolute deviation of the position estimates in the vicinity of 0.036 m.

A second hardware iteration, testing in a controlled environment and further analysis of the distribution of position estimates are recognized as future improvements. To support this, a lengthy discussion on these subjects and future work is included.

Keywords: UWB, positioning, indoor, navigation, evaluation system, precision, antenna, oscillator.

Acknowledgements

This thesis work could not have been done without the help from several people contributing with both their knowledge and enthusiasm.

We would like to thank the Syntronic Research and Development team in Gothenburg for welcoming us in to their group and allowing us to carry out this project. Especially our supervisors Verner Ljung and Steiner Thorvaldsson at Syntronic for helping us stay on track and supporting us throughout. We are very grateful for our examiner Jan Johansson, Department of Space, Earth and Environment at Chalmers, who took on this master thesis work and contributed with both useful discussions and guidance along the way.

A big thanks to the people from RISE who helped us along the way. Stefan Nord who broaden our insight into how UWB positioning systems can be applied. Mats Cedheim and Martin Forsberg who assisted us with the measurement and characterisation of antennas along with their openness and willingness to explain and teach their methods. Lastly, we would also like to thank Viktor Dahl for aiding us with software related issues and Martin Johansson who, with short notice, contributed equipment that enabled this project to be carried out.

Gustaf Dahl & Ludvig Johansson, Gothenburg, June 2020

Abbreviation

ADS - Asymmetrical Double-Sided
AUT - Antenna Under Test
BJT - Bipolar Junction Transistor
CMOS - Complementary Metal Oxide Semiconductor
CSRR - Complementary Split Ring Resonator
DC - Direct Current
EIRP - Effective Isotropic Radiated Power
FCC - Federal Communication Commission
FF - Fidelity Factor
FSLP - Free Space Path Loss
GNSS - Global Navigation Satellite System
IC - Integrated Circuit
LNA - Low-Noise Amplifier
LOS - Line of Sight
MAD - Mean Absolute Deviation
NLOS - Non Line of Sight
PCB - Printed Circuit Board
RF - Radio Frequency
RSS - Received Signal Strength
SMA - Subminiature Version A
SMD - Surface-Mounted Device
SNR - Signal-to-Noise Ratio
SPI - Serial Peripheral Interface
TCXO - Temperature Controlled Crystal Oscillator
TL - Transmission Line
ToF - Time of Flight
TWR - Two-Way Ranging
UWB - Ultra Wideband
WGN - White Gaussian Noise

Contents

List of Figures

List of Tables

1

Introduction

As industry, transportation and logistics moves towards autonomy, the desire to accurately position vehicles and robots increases. In general, methods of remote positioning is associated with satellite positioning and *Global Navigation Satellite System* (GNSS), a technique that is irreplaceable in many scenarios. However, it has its limitations in certain situations where visibility towards satellites is poor, i.e. indoors, dense city areas, tunnels, etc. *Ultra Wideband* (UWB) positioning is a technique well suited for creating local indoor positioning systems, applicable both in electromagnetically complex environments and kinematic situations.

UWB technology is a standardized wireless communication protocol, defined by its wide bandwidth. Its popularity stems from the ease of deployment in wireless sensor networks, being an unlicensed protocol due to the low output power allowed in such systems. The wide bandwidth is attractive for applications where high data transfer is desired, yet it is also an advantageous feature in positioning purposes which will become clear at a later stage.

The ability to precisely position an object wirelessly in a cost effective and easy to integrate manner will appeal to industry and transportation sectors among others. The study undertaken within this project focuses on the *precision* aspect. The aim is to investigate the relation between *radio frequency* (RF) hardware components and the positioning precision of the system.

The aim of the project will be approached with a broad scope in mind that will include the process of designing and manufacturing the hardware for a complete UWB positioning evaluation system. The design is based around the transceiver IC DW1000 from the semiconductor company Decawave [1], who specilizes in UWB positioning solutions. The design of the evaluation system will be adapted to serve the purpose of assessing the impact of different antenna designs and oscillators.

In order to determine the impact of these hardware choices, a test setup evaluating precision will devised. The test setup will emphasize repeatability and environments encountered in applied scenarios. The ambition is to be able to provide detailed insights regarding design choices, especially concerning antennas and oscillators, with regards to positioning precision.

1.1 Project Outline

The project concerns 3-dimensional positioning using UWB signals, or more specifically, evaluation of the impact of RF-components on positioning precision. To fully understand the connection between hardware performance and precision, the characteristics of the UWB signals has to be understood as well. Chapter 2 will begin with discussing the definition of the UWB signal and the regulations it faces, seguing into an analysis of the relation between time duration and bandwidth. Next, the actual method of ranging and positioning is explained with less generality and more focused on the equipment used in the project. This forms the basis for examining the issues faced in UWB positioning, such as time synchronization, multipath- and non-line-of-sight propagation and low signal power and their relation to positioning precision. In order to alleviate these issues, knowledge of how the system operates is required and considering the niche of the project - a deeper knowledge of the RF hardware is essential. This knowledge will allow connections to be made between the issues presented and the performance of the hardware being evaluated, specifically antennas and oscillators.

Chapter 3 concerns the methodology carried out during the project and include descriptions of the process of designing and manufacturing the evaluation board and antennas. These sections covers the problems faced during this process and how they were solved both in part and fully. Further on, initial testing and verification is presented and the chapter ends with a detailed description of the final test setup and the evaluation process, serving as the measure of the impact the RF hardware has on positioning precision.

The results of the test procedures are presented graphically in Chapter 4 along with statistics to support the evaluation. Interesting features and deviations from the norm are commented on as well. Chapter 5 incorporates a thorough discussion of the advantages and disadvantages of the test setups and the evaluation process and how they influenced the acquired results. The resulting impact of the evaluated hardware is further analyzed and some concluding remarks on hardware recommendations is attempted.

Due to the broad scope of this thesis, several ”loose ends” remain which necessitates a discussion of alternative design choices, further testing and suggestions to improve positioning precision. This will hopefully serve as useful information for future studies on the subject of high precision UWB positioning systems.

2

Theory

The purpose of this chapter is to provide the reader with a theoretical foundation of remote positioning using electromagnetic waves and more specifically, UWB signals. Initially, the concept of UWB and its key features are explained. The method of wireless ranging and positioning using time measurement is then discussed, focusing on the technique applied within this project. Further on, the challenges faced when performing positioning is detailed, thus identifying the issues that needs to be resolved to increase precision. Performance metrics for the components subject to evaluation are then considered and their relationship to positioning precision are sorted out.

2.1 Ultra Wideband Signals

UWB technology is regulated by the IEEE 802.15.4a protocol and is therefor standardized. However, it can be intuitively characterized by its wide bandwidth and the most important requirements that must be met are:

- A center frequency f_c in the range of $2.1 - 10.6GHz$
- A fractional bandwidth of $\Delta f = B/f_c = 0.2$, or at least a bandwidth of $500MHz$.
- A maximum *effective isotropic radiated power* (EIRP) of $-41.3dBm$. This is the power radiated from the antenna of an UWB device, and the power limit is on the level of what is generally considered background noise.

Figure 2.1 provides an illustration of the EIRP limitation as a function of frequency. It can be seen that the limitation extends outside the UWB spectrum, mainly restraining the radiated power at the lower end to avoid interfering with GNSS signals.

The broad range of operating frequencies and the the wide bandwidth makes the UWB signal potentially problematic, hence the low level of allowed output power which limits the UWB signals ability to interfere with other frequency bands within the range. However, instead the UWB signal is often interfered as the low power signal is difficult to detect among the other much stronger signals. This leads in to the discussion about the environment the UWB signals often are found within and the challenges faced when attempting to accurately position a device in such an environment. In order to understand how the UWB signal and the receiver copes

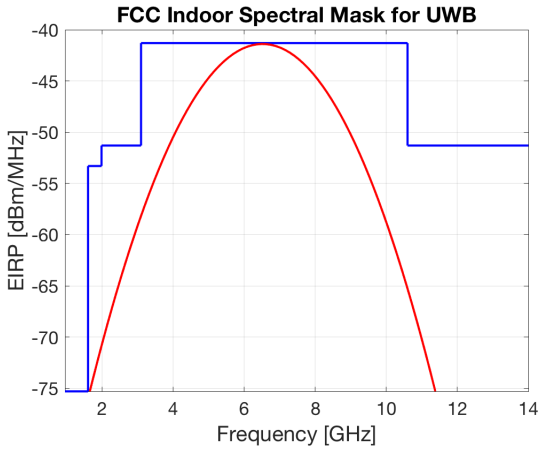

Figure 2.1: *Blue curve* indicates the FCC spectral mask and the *red curve* is a Gaussian distributed UWB signal fitted within the spectral mask.

with this situation and overcomes issues with interference, some knowledge about the physics behind an ultra wideband signal is necessary.

The term *ultra wideband* has a direct link to frequency domain analysis of a signal. While the frequency domain analysis provides a direct relation to transmission of data and signal power, many of the benefits of using UWB are more evident when performing the signal analysis in the time domain.

For the purpose of the following discussion, bandwidth is regarded as *frequency variance* Δ_ω^2 around a center frequency ω_c. Consider the objective of measuring the radiation from a source at a particular frequency interval. If the measuring instrument has a bandwidth far greater than the interval of the radiation, then the desired radiation will be hard to distinguish from the surrounding noise. With this in mind, the UWB signal has a large frequency variance and therefore terrible frequency resolution. However, there is a relation between the variance in frequency ω and time t - the *time-frequency uncertainty principle*.

$x(t)$ is an signal with arbitrary waveform such that it forms a Fourier pair with $X(\omega)$ as seen in Equation 2.1

$$X(\omega) = \int_{-\infty}^{\infty} x(t)e^{j\omega t}dt. \tag{2.1}$$

Thus, the energy contained within the signal can be written according to Parseval's theorem which gives the relation seen in Equation 2.2

$$E = \int_{-\infty}^{\infty} |x(t)|^2 dt = \frac{1}{2\pi}\int_{-\infty}^{\infty} |X(\omega)|^2 d\omega. \tag{2.2}$$

The temporal and spectral centers, t_c and ω_c respectively, can be interpreted as the first moment of the functions $x(t)$ and $X(\omega)$ described by Equation 2.3

$$t_c = \frac{1}{E}\int_{-\infty}^{\infty} t|x(t)|^2 dt \tag{2.3a}$$

$$\omega_c = \frac{1}{2\pi E}\int_{-\infty}^{\infty} \omega|X(\omega)|^2 d\omega. \tag{2.3b}$$

From which it follows that the second moment represents the variance in both temporal and spectral domain as expressed in Equation 2.4

$$\Delta_t^2 = \frac{1}{E}\int_{-\infty}^{\infty} (t-t_c)^2|x(t)|^2 dt \tag{2.4a}$$

$$\Delta_\omega^2 = \frac{1}{2\pi E}\int_{-\infty}^{\infty} (\omega-\omega_c)^2|X(\omega)|^2 d\omega. \tag{2.4b}$$

Multiplying the terms in Equation 2.4 results in what is called the *time-bandwidth product* $\Delta_t^2\Delta_\omega^2$. Sorting out the math on the right-hand side of Equation 2.4 using the differential- and duality property of Fourier transforms and the Cauchy-Schwartz inequality, the time-frequency uncertainty principle can be derived resulting in the expression in Equation 2.5

$$\Delta_t^2\Delta_\omega^2 \geq \frac{1}{4}. \tag{2.5}$$

From 2.5 it is clear that a large spectral variance Δ_ω^2 yields a small temporal variance Δ_t^2, which is the case for UWB signals. An intuitive interpretation of this is that it is difficult to determine at what frequency a certain event occurred, for example the radiation from a source, while it is easy to specify at what time the radiation reached the receiver. Figure 2.2 displays a typical Gaussian UWB pulse in the time domain, on the order of nanoseconds long.

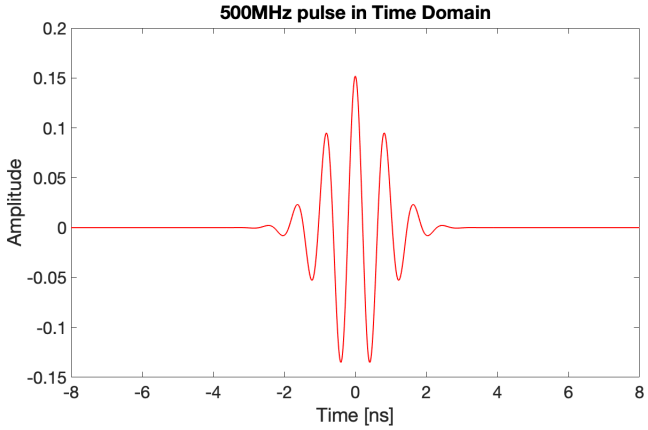

Figure 2.2: UWB pulse in the time domain. 500 MHz bandwidth corresponds to 2 ns long pulse.

2.2 Ranging, Trilateration and Positioning

The basis of positioning is combining more than one range (distance) measurement. The combining- as well as the ranging process varies depending on available equipment, environment and precision requirement. Measuring time is the method applied within this project and therefore constitutes the content of this section.

2.2.1 Time of Flight

Determining the *time of flight* (ToF) of a signal requires that the transmitter sends a timestamped signal of the time of transmission τ_{tx} to the receiver which timestamps the time of reception τ_{rx}. Assuming the signal propagated with the speed of light c the range can be calculated according to Equation 2.6

$$d = (\tau_{rx} - \tau_{tx})c = \tau_f c. \tag{2.6}$$

Figure 2.3 illustrates Equation 2.6.

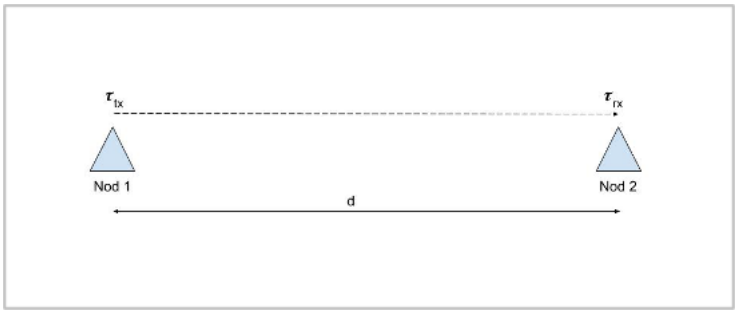

Figure 2.3: Concept of time of flight measurement.

Considering indoor environments without obstructions, the assumption of constant speed of light is considered robust. However, the issue lies in the timestamps which in order to provide precise ranging requires that the transmitter- and receiver clocks are synchronized. The local time of the clock can be modelled as a function of the true time t, where ideally $C(t) = t$, however, this is seldom the case. Instead, an estimate of the true time is obtained as $\hat{t} = C(t)$ which accounts for clock offset μ and clock drift δ. The model is expressed in Equation 2.7

$$C(t) = (1 + \delta)t + \mu. \tag{2.7}$$

Hence, the true duration of passed time $t_2 - t_1 = \tau$ can be expressed as in Equation 2.8

$$\hat{\tau} = C(t_2) - C(t_1) = \tau(1 + \delta). \tag{2.8}$$

Equation 2.8 indicates that the clock drift δ is an important measure of a clock's ability to track the true time (this concept is further explained in Section 2.5.1) [14].

Without a central clock timing the anchors, it is difficult to synchronize the anchors unless highly precise clocks are used. High precision timekeeping is both costly and bulky and therefore not an option in these applications, thus a method reducing the error induced by the lack of synchronization is required.

2.2.1.1 Two-Way Ranging

In Equation 2.7, the timekeeping ability of only one clock was considered. If instead considering the anchor and tag setup, both utilizing transceivers to transmit and receive signals, a two-way exchange of timestamps is enabled. This is illustrated in Figure 2.4, where the tag transmits a timestamp to the anchor which receives after the ToF. The anchor then processes this message and switches to transmitting mode, this process has a duration of $\tau_{reply1} >> ToF$. The anchor then transmits its timestamp back to the tag, thus finishing the roundtrip which has a duration τ_{round1} and can be expressed as seen in Equation 2.9

$$\tau_{round1} = 2\tau_f + \tau_{reply1}. \tag{2.9}$$

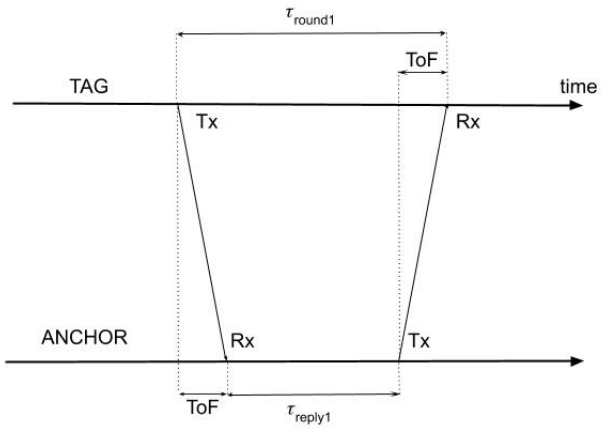

Figure 2.4: Basic operation of two-way ranging.

Using the expression in Equation 2.7, the roundtrip- and reply time can be estimated as in Equation 2.10

$$\begin{cases} \hat{\tau}_{round1} = \tau_{round1}(1 + \delta_A) \\ \hat{\tau}_{reply1} = \tau_{reply1}(1 + \delta_B). \end{cases} \tag{2.10}$$

Rewriting Equation 2.9 to acquire the ToF τ_f and inserting the estimations from Equation 2.10, the estimated ToF is obtained in Equation 2.11

$$\hat{\tau}_f = \frac{1}{2}(\hat{\tau}_{round1} - \hat{\tau}_{reply1}). \tag{2.11}$$

The error between the estimation and the true ToF can then be expressed as in Equation 2.12

$$\hat{\tau}_f - \tau_f = \tau_{round1}\delta_A - \tau_{reply1}\delta_B = \tau_f\delta_A + \frac{\tau_{reply1}}{2}(\delta_A - \delta_B) \tag{2.12}$$

where Equation 2.9 was used to acquire the final expression. To provide some sense of scale, the clock drifts $\delta_{A,B}$ can be on the order of ± 20 ppm, indoor environments usually mean that the ToF is in the range of *tenths of nanoseconds* and the replytime in the vicinity of *1* milliseconds which would yield an error on a meter level. However, this poor precision can be avoided by adding another timestamp exchange as will be made clear in the next section [15].

2.2.1.2 Asymmetrical Double-Sided Two-Way Ranging

In order to obtain a ranging system with decimeter level precision, without clock synchronization, an *asymmetrical double-sided two-way ranging* algorithm (ADS-TWR) must be implemented. The operation is illustrated in Figure 2.5 and the *double-sided* feature stems from the double exchange between tag and anchor. The *asymmetry* comes from not assuming that the replytimes τ_{reply1} and τ_{reply2} are equal, as this is usually not the case since the transmit- and receive path in the device are significantly different.

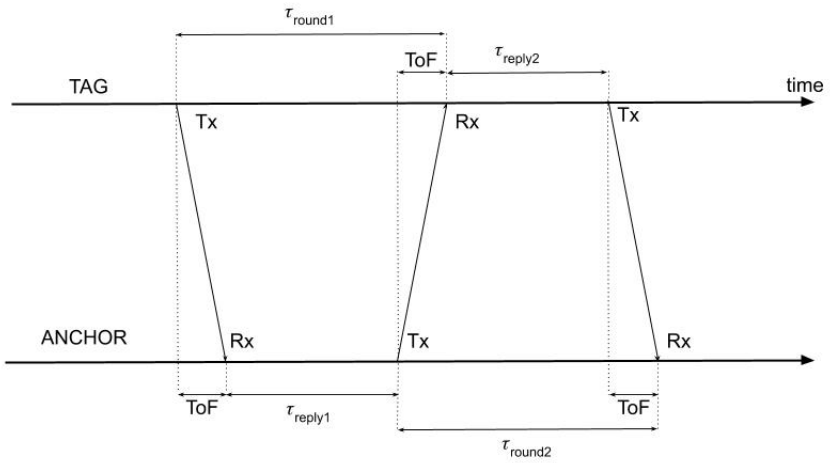

Figure 2.5: Basic operation of asymmetrical double-sided two-way ranging.

From Figure 2.5 it is clear that the two roundtrip times can be written as in Equation 2.13

$$\begin{cases} \tau_{round1} = 2\tau_f + \tau_{reply1} \\ \tau_{round2} = 2\tau_f + \tau_{reply2} \end{cases} \tag{2.13}$$

which implies that $\tau_{round1} + \tau_{reply2} = \tau_{round2} + \tau_{reply1}$. Multiplying the roundtrip times with each other leads to Equation 2.14

$$\begin{aligned} \tau_{round1}\tau_{round2} &= (2\tau_f + \tau_{reply1})(2\tau_f + \tau_{reply2}) \\ \implies \tau_{round1}\tau_{round2} - \tau_{reply1}\tau_{reply2} &= 2\tau_f(2\tau_f + \tau_{reply1} + \tau_{reply2}). \end{aligned} \tag{2.14}$$

Rewriting Equation 2.14 using Equation 2.13, the expressions in Equation 2.15 are acquired

$$\begin{cases} \tau_{round1}\tau_{round2} - \tau_{reply1}\tau_{reply2} = 2\tau_f(\tau_{round1} + \tau_{reply2}) \\ \tau_{round1}\tau_{round2} - \tau_{reply1}\tau_{reply2} = 2\tau_f(\tau_{round2} + \tau_{reply1}). \end{cases} \tag{2.15}$$

Combining the expressions in Equation 2.15, an expression for the ToF is presented in Equation 2.16

$$\tau_f = \frac{\tau_{round1}\tau_{round2} - \tau_{reply1}\tau_{reply2}}{2(\tau_{round1} + \tau_{reply2})} = \frac{\tau_{round1}\tau_{round2} - \tau_{reply1}\tau_{reply2}}{2(\tau_{round2} + \tau_{reply1})}. \tag{2.16}$$

To present an expression for the measured, or estimated, ToF, the clock drifts need to be accounted for. Assigning the delay/advancement created by the clock drifts in an easier-to-read manner as in Equation 2.17

$$\begin{cases} \hat{\tau}_{round1} = k_A\tau_{round1} \\ \hat{\tau}_{round2} = k_B\tau_{round2} \\ \hat{\tau}_{reply1} = k_B\tau_{reply1} \\ \hat{\tau}_{reply2} = k_A\tau_{reply2}. \end{cases} \tag{2.17}$$

Assuming that the drifts are the main contributor to error in timekeeping, the estimated ToF is expressed in Equation 2.18

$$\begin{aligned} \hat{\tau}_f = \frac{k_Ak_B}{k_A}\frac{\tau_{round1}\tau_{round2} - \tau_{reply1}\tau_{reply2}}{2(\tau_{round1} + \tau_{reply2})} &= k_B\tau_f \\ \frac{k_Ak_B}{k_B}\frac{\tau_{round1}\tau_{round2} - \tau_{reply1}\tau_{reply2}}{2(\tau_{round2} + \tau_{reply1})} &= k_A\tau_f \end{aligned} \tag{2.18}$$

The error of the estimation is, using ADS-TWR, reduced to the expressions in Equation 2.19

$$\begin{cases} \hat{\tau}_f - \tau_f = k_A\tau_f - \tau_f = \delta_A\tau_f \\ \hat{\tau}_f - \tau_f = k_B\tau_f - \tau_f = \delta_B\tau_f. \end{cases} \tag{2.19}$$

This result indicates that the error between estimate and true time is only dependent on the clock drift in either of the clocks. This significantly reduces the error as the potential risk of the clocks drifting in opposite directions disappears [15].

2.2.2 Trilateration and Positioning

The position of the tag acquired through the process of trilateration. It is intuitively described as obtaining the intersection point(s) of three spheres, centred at the anchors location, with a radius corresponding to the range between anchor and tag. As the anchors are all located at the same height this method will result in an ambiguous result in the height component when using three anchors, adding a fourth will solve this issue. This method is illustrated in Figure 2.6 where the uncertainty of the range measurements have been accentuated indicating that the intersecting area is the precision of the position.

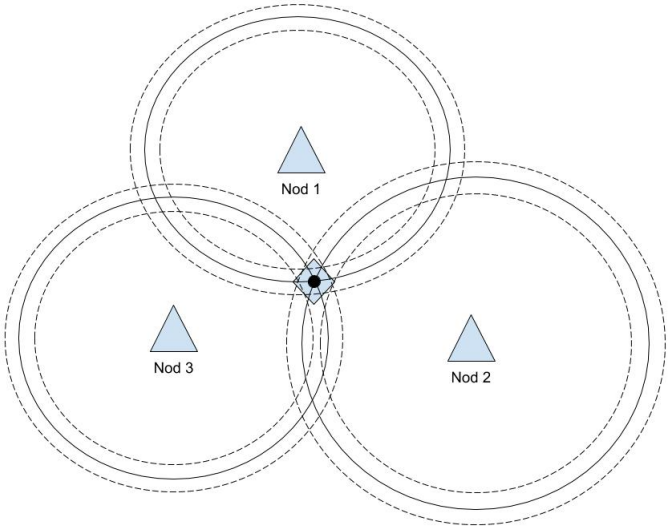

Figure 2.6: Intersection point provides the position estimate. Dashed lines indicate uncertainty in range measurements.

The software provided by Decawave requires the anchor's relative 3D positions as input in order to solve the position of the tag. A more mathematically helpful illustration is found in Figure 2.7,

where **C0**, **C1** and **C2** are the center of the spheres, **r0**, **r1** and **r2** are the ranges and **P** is the intersection point or area. The three spheres surrounding the anchors can be described by Equation 2.20a, 2.20b and 2.20c

$$r_0^2 = x^2 + y^2 + z^2, \tag{2.20a}$$
$$r_1^2 = x^2 + (y-a)^2 + z^2, \tag{2.20b}$$
$$r_2^2 = (x-b)^2 + (y-c)^2 + z^2. \tag{2.20c}$$

Solving these equations simultaneously will yield the position **P** of the tag. The first step is subtracting Equation 2.20b from 2.20a resulting in the y-position of the intersection as seen in Equation 2.21

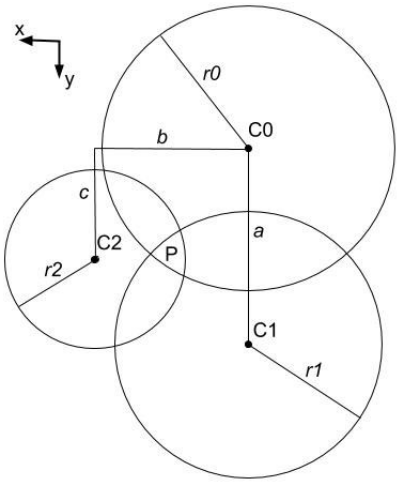

Figure 2.7: Trilateration, **C0** located at (0,0), **C1** at (0,a) and **C2** at (b,c).

$$\begin{aligned} r_0^2 - r_1^2 &= y^2 - (y-a)^2 \\ y &= \frac{r_0^2 - r_1^2 + a^2}{2a}. \end{aligned} \tag{2.21}$$

The second step is subtracting Equation 2.20a from 2.20c resulting in the x-position of the intersection as seen in Equation 2.22

$$\begin{aligned} r_2^2 - r_0^2 &= b^2 + c^2 - 2bx - 2cy \\ x &= \frac{r_0^2 - r_2^2 - 2yc + b^2 + c^2}{2b}. \end{aligned} \tag{2.22}$$

As previously mentioned, the anchors are all located at the same height producing a geometry unable to detect if the tag is above or below the plane of the anchors. Thus, the z-position is acquired with ambiguity from Equation 2.20a resulting the Equation 2.23

$$z = \pm\sqrt{r_0^2 - x^2 - y^2} \tag{2.23}$$

where the $\pm$ indicates that the solution is found at a distance z perpendicular to the xy-plane seen in Figure 2.7. This is an extreme case of what is referred to as *dilution of precision* (DOP), a term commonly used in satellite navigation to relate positioning error to the geometry of the nodes within the system [7]. Increased separation of the anchor locations will generate a more beneficial geometry, thus increasing precision. Expanding the system to include more anchors in carefully chosen locations would not only solve the problem of ambiguity, it is likely it would also lead to improved positioning precision.

2.3 Signal Environment

The transmitted pulse is heavily dependent on the environment it propagates within and considering the applications of UWB positioning, the surroundings can contain many objects necessitating complex propagation paths to reach the receiver. The quality of the signal reaching the receiver is dependent on the wave's ability to penetrate obstacles and refract off of objects. This section provides insight into the subjects of *absorption losses* and *multipath* as these concepts will assist the reader in understanding the difficulties typically faced in indoor environments.

2.3.1 Absorption Losses

Upon interaction with material, an EM-wave is scattered, absorbed and reflected. These three phenomena are linked to each other and all contribute to a loss of energy in the direction the wave was propagating in. When discussing signals within the frequency range of the UWB spectrum, the main concern is to what extent the wave is *absorbed* by the material [3]. Materials absorb energy and convert it to heat to various extents which can be partly described by the material's *refractive index* n as seen in Equation 2.24

$$n = n' - jn''. \tag{2.24}$$

The complex part of n describes the *absorption loss* in the case of a positive valued n''. Thus sharing a close relationship to the absorption coefficient γ_a which represents the intensity of absorption per unit length, according to Equation 2.25

$$\gamma_a = \frac{2\omega n''}{c}. \tag{2.25}$$

Thus, the loss of energy in the path of propagation over distance z can be described by an exponential decrease in flux density as seen in Equation 2.26

$$I(z) = I_0 e^{-\gamma_a z} = I_0 e^{-\frac{2\omega n''}{c} z} \tag{2.26}$$

which is known as the *Beer-Lambert law* where $I(z)$ is the distance dependent flux density $[W/m^2]$ and I_0 is the incident flux density $[W/m^2]$.

It is therefore clear that increased frequency or complex refractive index attenuates the signal more. To quantify a material's opacity to a certain frequency the term *penetration depth*, also known as *absorption length* ℓ_a, is commonly used. It is the distance the wave travels within in the medium corresponding to an attenuation of $1/e$ [3]. This distance is derived from Equation 2.26 and coincides with the reciprocal of the absorption coefficient γ_a according to Equation 2.27

$$\ell_a = \frac{1}{\gamma_a} = \frac{c}{2\omega n''}. \tag{2.27}$$

While indoor environments often consists of a plethora of different materials, the large surfaces are commonly made of poorly conducting materials such as wood, concrete, plaster or glass. These materials often exhibit a penetration depth on the order of centimeters to decimeters within the UWB frequency range. However, as the conductive properties of a material increases so does the complex refractive index leading to a very short penetration depth. Metals are generally very good conductors and as such have a penetration depth on the level of micrometers, often referred to as *skin depth*. In an applied scenario this means the signal will definitely not penetrate metals, yet the signal might penetrate most walls and windows albeit weakened. This results in two issues:

- The already weak signal is now weaker making it harder to detect in relation to the noise floor.
- The velocity of propagation is dependent on the refractive index of the material as in Equation 2.28

$$\nu = \frac{c}{n} \tag{2.28}$$

  and as $n > 1$ for the above mentioned materials the velocity will decrease during the period the signals propagates within the obstruction. Recalling that the distance calculation is based on Equation 2.6, even small deviations from the speed of light will result in errors in the distance measurements.

2.3.2 Multipath

As mentioned in Section 2.3.1, the signal is scattered, absorbed or reflected when interacting with a material, this section will focus on reflections. Simply put, when the wave propagates from one medium to another part of the energy will be reflected in a new direction that is dependent on the wave's angle of incidence. Figure 2.8 depicts a possible scenario where the direct path is obstructed leading to the issues explained in Section 2.3.1. However, there are other objects present in the vicinity of the two nodes.

The signal is reflected off the surfaces of these objects leading to node 2 receiving signals that have propagated several different paths - a phenomena called *multipath*. To acquire the correct distance measurement the signal received from the direct path needs to be detected and processed according to the methodology in Section 2.2.1.2. Yet, the direct path is likely weakened from absorption losses in the obstruction. The reflected paths could possibly possess a higher amplitude than the direct path, depending on the refractive index n of the objects. The ratio of power reflected and transmitted r from a non-magnetic medium is given by Equation 2.29

$$r = \left| \frac{n_1 - n_2}{n_1 + n_2} \right|^2 \tag{2.29}$$

where the 1 and 2 subscripts indicate the transition from one medium to another, in this case air to object. In the case that the second medium is a metal, meaning that the signal is unable to penetrate the object, most of the signal is instead reflected.

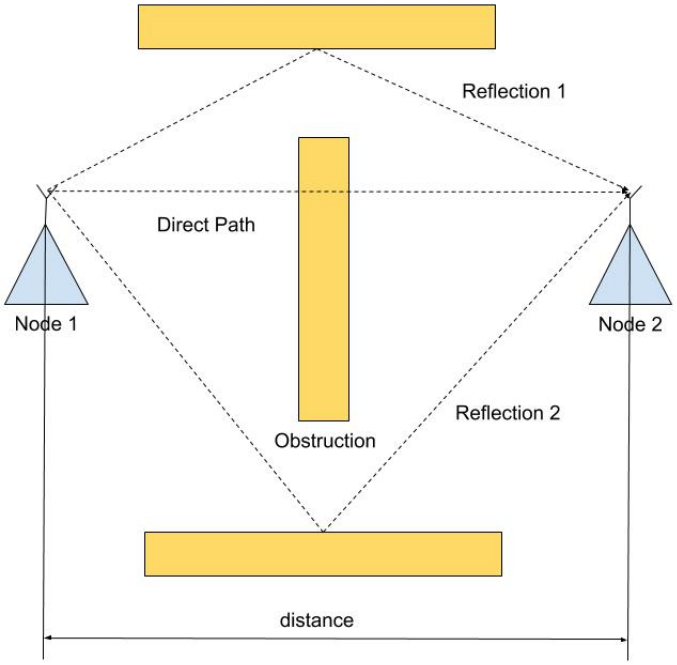

Figure 2.8: Non-line-of-sight scenario with reflecting surfaces. Node 1 acting as transmitter and Node 2 as receiver.

This leads to a reflected path exhibiting a higher amplitude than the direct path making the reflected path easier to detect. Thus registering a distance greater than the direct path. Figure 2.9 illustrates this situation, where a form of threshold detection is used as in the Decawave DW1000.

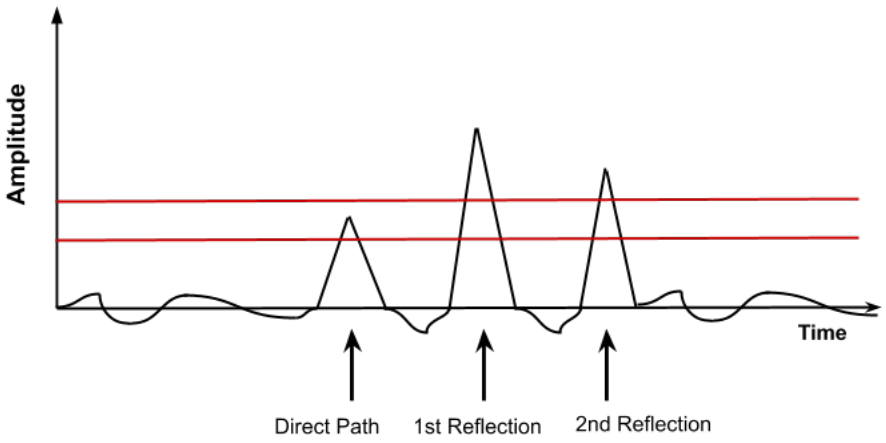

Figure 2.9: Simplified illustration of threshold detection with the two red lines indicating two possible levels for detection.

The higher threshold level does not detect the desired direct path and will instead timestamp the 1st reflection. In this scenario both reflections have a higher amplitude

than the direct path which is a common case in complex indoor environments.

As seen in Equation 2.24, the refractive index is a complex value suggesting that the reflected signal will have its phase shifted in relation to the incident signal. With signals being received in node 2 from several directions with different path lengths, *wave interference* is commonly the result. Waves will interfere with each other depending on their relative phase, either constructively or destructively, producing new waves with higher or lower amplitude as illustrated in Figure 2.10 [4].

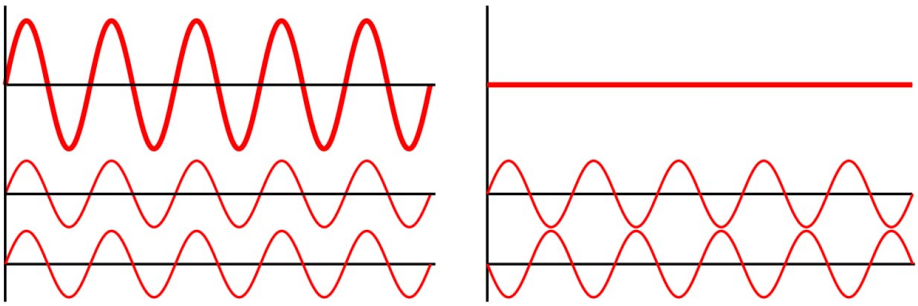

Figure 2.10: Interference of two waves with resulting wave above. *Left*: Constructive interference. *Right*: Destructive interference. [5]

As discussed in Section 2.1, the UWB pulses are very short when compared to more narrowband pulses. This is beneficial in multipath environments as the pulses received from different paths are less likely to interfere, stemming from the low probability of two or more pulses being received within the period of the other. Although robustness against multipath is one of the advantages of applying UWB in positioning systems, it can be still lessen the precision of the system. This is especially apparent when the direct path signal is heavily attenuated from obstructions.

2.4 Noise

Noise can be seen as random, undesirable, signals that may interfere with the wanted signal and reduce the precision and accuracy of the measurement of it. Even though anything that is interfering with the signal can be seen as noise the main contributor is the thermal noise, also known as *Johnson noise*.

Thermal noise is the motion of electrons that generates an undesired voltage and relates to the temperature as seen in Equation 2.30

$$P = kTB \tag{2.30}$$

where P is the noise power, k is the Boltzmann constant, T is the temperature and B is the bandwidth. Over a specific bandwidth the noise can be seen as *White Gaussian Noise* (WGN), meaning that it has the same noise power for each Hz of frequency [16].

Electrical current is the flow of discrete electrical charges. Due to the fact that the number of these discrete particles is going to vary will lead to a fluctuation in the

current. For independently acting particles the current noise density can be described as in Equation 2.31

$$i_n = \sqrt{2qI_{dc}}. \tag{2.31}$$

Where, q is the electron charge ($1.60x10^{-19}$ coulomb). This noise is known as *Shot noise* and, as for the Johnson noise, this noise is seen as WGN and the amplitude over a specific bandwidth can be calculated via Equation 2.32

$$i_{noise}(rms) = \sqrt{2qI_{dc}B}. \tag{2.32}$$

Both Johnson noise and shot noise will always be present due to physical fundamentals. Actual devices will also have other sources of noise, which for example depends on the manufacture and material properties of the device. A resistor will have variations in resistance which will lead to generation of additional noise voltage. This sort of noise is called *flicker noise* and appears as a 1/f power spectrum. Figure 2.11 shows the characteristics of flicker noise where f_c is known as the *corner frequency*, which is the point where the flicker noise is the same as the white noise component [16].

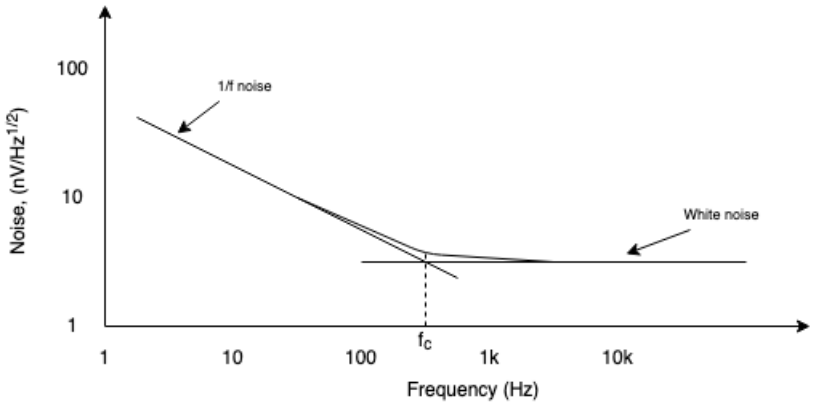

Figure 2.11: illustration of flicker noise on log axes as noise voltage versus frequency. Frequency marked as f_c is the corner frequency.

Another kind of noise is that known as *Burst Noise*, also called as popcorn noise or *Random Telegraph Signal Noise* (RTS noise). This type of noise is seen in devices like transistors, *Integrated Circuits* (ICs), film resistors and more. It appears due to contamination of metallic atoms amid processing or crystallographic damaging regions close to junctions. This noise appears as burst in the collector current at a random rate, and is proportional to $1/f^2$ which makes it most present at lower frequencies [6].

As mentioned in the beginning of this section noise is undesirable when it comes to the detection of a desirable signal. It is therefore appropriate to talk about the *Signal-to-Noise Ratio* (SNR) which is the ratio between the signal power and the noise power, and most often expressed in dB. It is desirable to have a relative large SNR to easily distinguished desired signal from the noise, but a higher SNR often means that the complexity in the system increases.

2.5 Theory of Evaluated Components and Relation to Positioning Precision

In the following sections theory regarding the components which will be tested for their impact on the precision in a positioning system will be presented. Focus will be on oscillators and antennas, explaining key features such as oscillator stability, antenna directivity and gain but also what effect an antenna which blocks certain part of the designated frequency spectrum might have. This report where also supposed to investigate what the implementation of a *Low Noise Amplifier* (LNA) would have however, due to unforeseen events, it had to be excluded from this report. But for the interested reader the theory regarding the LNA will still presented in this section.

2.5.1 Clocking - Crystals and Oscillators

In any process where precision measurement is desired some sort of time reference needs to be available. In electronic circuits this is mostly done by implementing a clock in the form of an oscillator. In order to work as a clock the oscillator needs to generate accurate periodic, equal spaced, pulses. The precision and accuracy of the measurements will depend highly on how precise the frequency of the clock is, meaning that the oscillator will need to have high stability and tolerance in order to minimize the frequency drift, which will be described later in this section. One of the most stable and well used sources for oscillation is the quartz crystal.

Quartz is a glass like looking mineral made of silicon and oxygen (SiO_2) and found all around the globe. In 1880 it was discovered that quartz had direct piezoelectric properties. This effect is defined as when a mechanical strain is applied to a crystal, an electrical polarization proportional and in the same direction as the strain is produced. Later it was also discovered that when a voltage is applied to a crystal it will be strained, known as the converse piezoelectric effect. Quartz is also known as anisotropic, meaning that it is directional sensitive depending on how the crystal is cut. An example is that electric conductivity can be thousand times greater in one direction than in the other [21]. So by applying an electric field acoustic waves is induced in the crystal which will generate a voltage at the crystal surface and by applying contacts on this surface you will have a circuit element [16]. This can be modelled by a RCL circuit illustrated in Figure 2.12.

Capacitance C_0 in the figure is a physical element which is present if the crystal is oscillating, which arises from the leads, electrodes and holders. The other three circuit elements C_1, L_1 and R_1 are not physical components, they are rather representations of various effects in the crystal and known as the motional arm of the resonator. C_1 is due to the stiffness of the crystal which is transformed into piezoelectric effect. L_1 is the effective mass of the crystal converted electrical conditions, and R_1 serve as frictional loss. The impedance of the two circuit elements C_1 and L_1 can be extremely high. The inductance can be as large as one Henry and the capacitance can be as low as 0.1 fento-Farad, the resistance R_1 can range from a few Ohm to tens of thousands ohms. From figure 2.12 one can see that the equivalent circuit

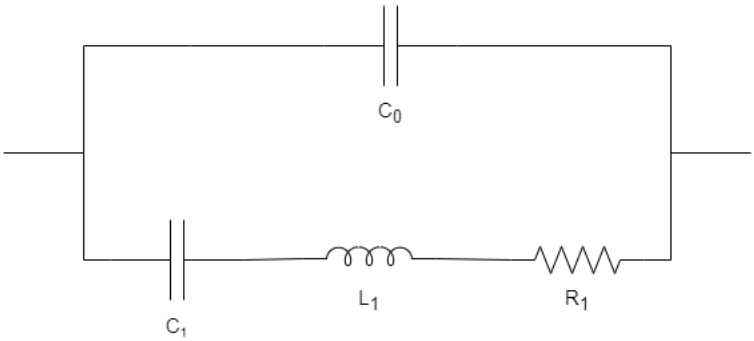

Figure 2.12: Equivalent electrical circuit for a quartz crystal resonator.

takes the form of a resonant circuit, and due to the values stated above the *Quality factor* Q, presented in Equation 2.33, can be very high which is physically impossible with real components. This property makes the quartz crystal highly suitable as an oscillator. The Q factor in a resonant circuit relates to the loss of the circuit, where lower loss gives a higher Q value. It is the high Q of the quartz crystal that makes it widely used as an effective oscillator [18], [21].

$$Q = \frac{1}{R_1}\sqrt{\frac{L_1}{C_1}}. \tag{2.33}$$

The Q value excluding the external loading effects is known as the unloaded Q, or Q_0. When the resonator is connected to external circuitry it will impact on the overall Q value, this is known as the loaded Q, or Q_L [18]. The loaded Q will have an important role for designing a crystal oscillator. By defining a transfer function $H(j\omega)$, where ω is the frequency in radians, one can find the phase of the function via Equation 2.34

$$\phi(j\omega) = tan^{-1}\left[\frac{Im(H(j\omega))}{Re(H(j\omega))}\right]. \tag{2.34}$$

By then take the derivative of the phase, which is the phase slope, with respect to ω one will get the loaded Q as in Equation 2.35

$$Q_L = \frac{\omega_0}{2}\left[\frac{d\phi(j\omega)}{d\omega}\right],\ when\, \omega = \omega_0. \tag{2.35}$$

Here, ω_0 is the resonant frequency. What can be seen from the above equation is that for a higher Q_L there will be a steeper phase response in the vicinity of ω_0, which can be seen in a phase response curve [21].

A crystal oscillator has two different resonant frequencies, known as *series resonant frequency* f_s and *parallel resonant frequency* f_a. The resonant frequency for f_s is calculated by 2.36 and for f_a by 2.37.

$$f_s = \frac{1}{2\pi\sqrt{L_1 C_1}} \tag{2.36}$$

$$f_a = \frac{1}{2\pi\sqrt{\frac{C_0 C_1}{C_0 + C_1}}}. \tag{2.37}$$

The series resonant frequency is stated for when the capacitance and inductance reactance in the motional arm of figure 2.12, i.e. C_1 and L_1, cancels. At this point, the crystal impedance will be at a minimum and the current through the resonator will be at maximum. C_0 will in this point be parallel with R_1 and the reactance will be much lower then the resistance, this will then lead to the crystal appearing resistive with a resistance very close to R_1. The parallel resonant frequency links the two parallel capacitance's C_0 and C_1. Operating at this frequency, the crystal will have a maximum impedance and a minimum current flow. f_s will be lower then f_a and the region between these two frequencies is known as the *parallel resonance region* where most oscillators operates at [22].

The series- and parallel-resonant oscillators will use series- and parallel-resonant crystals. The definition of a series-resonant crystal is that it is calibrated so that its nominal frequency is at the series resonant point f_s. The same principle is used for the parallel-resonant crystal, but instead of operating at a specific frequency point it is calibrated to operate within the parallel resonance region [21].

Due to the fact that the parallel-resonant oscillator is calibrated for a frequency region and not a single point makes it necessary to implement a form of adjustment to the circuit in order to limit the resonant frequency. This tuning is done by implementing whats known as *load capacitance* C_L on the input and output of the oscillator, this will limit the region into a specific point, which can be seen in Equation 2.38

$$f_L = f_s \left(1 + \frac{C_1}{2(C_0 + C_L)}\right). \tag{2.38}$$

where f_L is the frequency of the crystal with C_L.

Ideal crystal oscillators resonates at a specific frequency without any deviations or uncertainties, this is known as the *nominal frequency*. However, this is not the case for a real physical oscillator. Besides basic parameters such as frequency and amplitude there is also *stability*. In an oscillator circuit there will be presence of noise. This noise will have an impact on the phase and amplitude of the generated output of the crystal oscillator and might critically effect the oscillators performance. If the oscillator should follow the Barkhausen criteria, which states the oscillation condition, a disturbance to the phase will lead to a frequency change, and thus phase noise. In order to cope with these effects it is desirable to have as high loaded Q as possible, as can be seen from equation 2.35 [21].

Phase noise of an oscillator is seen as the random variation in the phase, or frequency, and depict the stability of an oscillator. The phase noise can be random or induced, known as stochastic or deterministic [2]. The phase noise is due to thermal and

other noise sources, described in section 2.4. For an ideal oscillator the signal would appear as a delta function in the frequency domain, but when phase noise is added the spectrum will appear as a broadening of the signal, illustrated in figure 2.13.

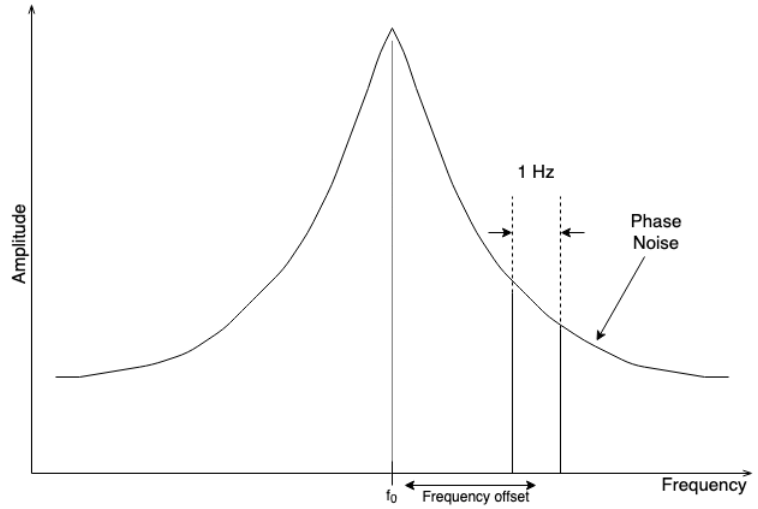

Figure 2.13: Illustration of phase noise around frequency f_0.

The stability of an oscillator can also be described in time domain with the jitter method, which collects all the noise sources. When measuring the pulse from the oscillator one can see a small fluctuation in the waveform, seen in figure 2.14. These small variations is caused by phase fluctuations [2].

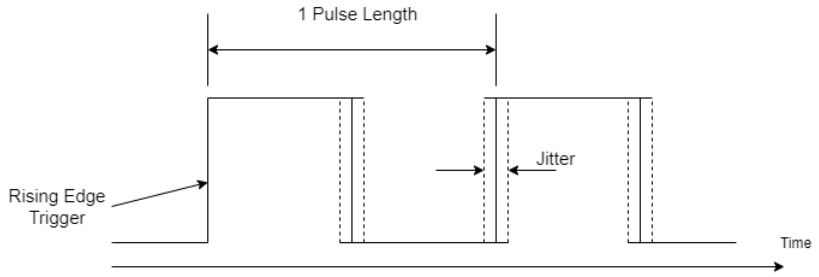

Figure 2.14: Illustration of jitter on an ideal square wave pulse.

Oscillators may also be affected by the temperature. Most oscillators are designed for room temperature i.e. 25 $°C$. As the temperature of the oscillator starts to deviate from the optimal temperature it might lead to a shifting frequency. The temperature to frequency relationship is determined by the quartz crystal cut, which is beyond the scope of this report and will therefore not get any deeper explanation in this report. The reader is, for a deeper understanding of the different quartz crystal cuts, referred to [21].

In order to achieve a better stability over a specified temperature interval one can chose *Temperature Controlled Crystal Oscillator* (TCXO) which adjusts the crystal by altering the load capacitance regarding to temperature. Figure 2.15 illustrates the temperature compensated crystal to a non temperature compensated crystal.

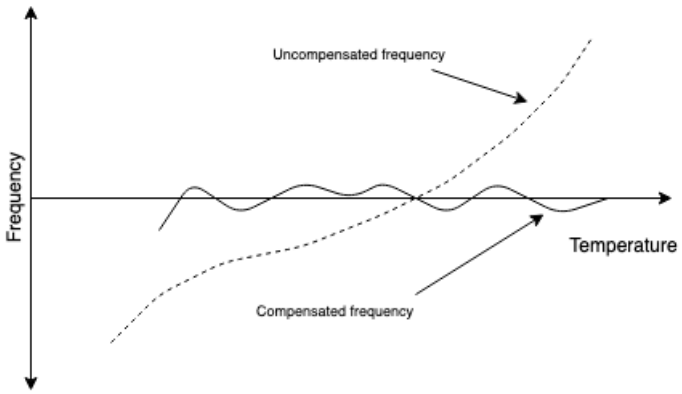

Figure 2.15: Illustration of frequency correction with a TCXO compared to uncompensated crystal.

2.5.2 Low-Noise Amplification

In almost all systems where a weak signal is supposed to be distinguished the eventual limit of detection is the noise, presented in Section 2.4. To minimize the impact of noise on the signal that is meant to be detected it is desirable to amplify the relative small signal while suppressing the noise. This can be done by implementing a LNA in the circuit. The LNA is not an ideal component, meaning that it will generate its own noise. This can be represented as in figure 2.16 which shows the internal voltage noise (u_n) and current noise (i_n) of a *Bipolar Junction Transistor* (BJT).

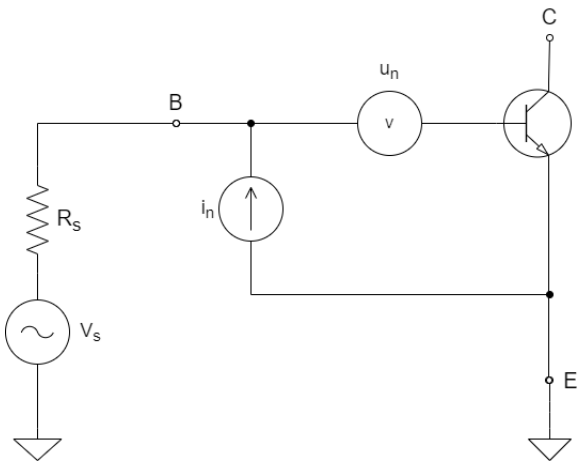

Figure 2.16: Noise model of a BJT transistor.

Here, V_s is the source voltage, R_s the source impedance, u_n is the noise voltage and i_n is the noise current. One can then calculate the total noise voltage from the amplifier (u_{an}) via Equation 2.39

$$u_{an} = \sqrt{u_n^2 + (R_s i_n)^2} \tag{2.39}$$

As can be seen from the formula, if there is a high source impedance, the current noise will be dominant part of the amplifier noise and vice versa, if the source

impedance is low, the noise voltage will be the main contributor. The voltage noise u_n is derived from the collector current shot noise which generates a noise voltage over the intrinsic emitter resistance (r_e), which is a small signal impedance when looking into the emitter (this is no resistance though but rather the transistors inverse transconductance $1/g_m$), defined as $r_e = V_T/I_C = kT/qI_C$ [16]. Here, k is the Boltzmann constant, T the temperature, q is the electron charge and I_C is the collector current. It also consist of the thermal noise and shot noise through the base resistance $r_{bb'}$. The noise density u_n^2 at the input can then be calculated by Equation 2.40

$$u_n^2 = 4kT(\frac{r_e}{2} + r_{bb'}) \tag{2.40}$$

The noise density can here be seen as thermal noise from two separate resistors. Seen from the definition of r_e, the noise voltage will decrease with an increase in collector current. From this one can conclude that to lower the noise voltage it is favourably to run at a higher collector current. The drawback from this is increased heating of the transistor and higher base current.

For the input noise current i_n, a noise voltage will appear over the input source impedance. The leading contributor will be shot-noise, which can be seen in Equation 2.41

$$i_n = \sqrt{\frac{2qI_C}{h_{FE}}} \tag{2.41}$$

Here, h_{FE} is the DC (*Direct Current*) gain for the BJT [19]. At low frequencies flicker noise will appear, presented in Section 2.4, which will contribute to the i_n^2. The base current noise density will follow the characteristics of flicker noise until a certain frequency, where it will go over to base-current shot noise $\sqrt{I_B}$, this point is called the corner frequency f_c, where the flicker noise is equal to the underlying white noise. What should be noted is that for low frequencies the base-current shot noise is unrelated to the collector current shot noise. This is not true though for high frequencies. At higher frequencies h_{FE} goes to unity, known as the gain bandwidth product f_T [20]. This lead to collector current's shot noise appearing in the base. These effects combined can be seen in Equation 2.42

$$i_n^2 = 2q\frac{I_C}{h_{FE}}\left(1 + \frac{f_c}{f}\right) + 2qI_C\left(\frac{f}{f_T}\right) \tag{2.42}$$

As the noise voltage density is generated when the noise current is going through the signal source impedance, it will have a magnitude of $v_n = i_n Z_{in}$. The total input-referred squared noise voltage is calculated by Equation 2.43

$$v_n^2 = e_n^2 + 4kTR_s + (i_n R_s)^2 \tag{2.43}$$

What should be noted in the above equation is, if the impedance is of reactance type, the last term in the equation, i.e. the current noise contribution, will be frequency dependant [16].

One can now see from Equations 2.40 and 2.41 that the voltage noise will decrease while the current noise will increase with a higher I_C current. The goal for creating a low noise BJT is then to find a I_C current that gives the lowest total noise voltage u_{an} with a specific R_S.

Now that the internal noise of a BJT has been described the next step is to examine the possibility of amplification of it. As mentioned in the beginning of this section, to distinguish a relative small signal is to suppress the noise while amplifying the desired signal. As the BJT is an active device, to work as an amplifier it will have to take the bias power and transform it into signal power. Consider figure 2.17 where the base is forward biased and the collector is reversed biased.

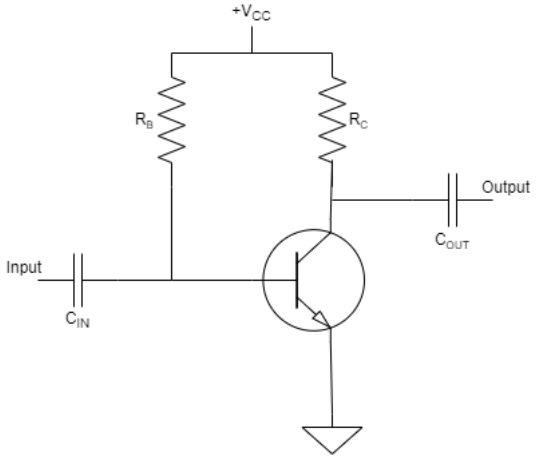

Figure 2.17: Circuit diagram of a BJT amplifier.

The current flowing through the base is $I_B = V_{CC}/R_B$. It is then possible to calculate the current gain (β) of the transistor by $\beta = I_C/I_B$ if I_C is known, alternatively the collector current can be determined if the transistor gain is known.

To get the transistor to work as a signal amplifier a input signal needs to be applied on the base of the transistor. The capacitance will work as a high-pass filter and only let the desired alternating current signal to propagate through, blocking the direct current from the bias network leaking back [17]. The output voltage can then be computed bu Equation 2.44

$$V_C = -i_C R_C = \frac{\beta}{i_B} R_C \tag{2.44}$$

A final observation that can be made is that both the amplification and noise contribution for a BJT amplifier relates to the I_C current. One has to find a suitable value of I_C for the amplifiers desired task in order to get as low noise contribution as possible while still getting enough amplification.

2.5.3 Antennas

Initially, a brief review of general antenna theory is presented, introducing necessary concepts and terminology. This is then used to explain and detail important factors indicating the performance of an antenna. After some general comments on antenna theory, the discussion is mainly limited to microstrip antennas applied within IR-UWB.

The radiation from the antenna behaves differently depending on where the field is observed in relation to the phase reference point. Roughly described, the radiation zones can be divided in to two regions; the *near-field-* and the *far-field* regions. This project is exclusively concerned with far-field radiation and it is thus the basis for all the forthcoming theory. The distance to the far-field region $\boldsymbol{r}$ can be approximated by the expression in Equation 2.45

$$r \leq \frac{2D^2}{\lambda} \tag{2.45}$$

where D is the diameter of the aperture which can be approximated in the case of a microstrip antenna as the diameter of the smallest sphere enclosing the whole mechanical construction and λ is the carrier wavelength. Within this project, the far-field region can be found around ~ 0.1 m, thus ruling out all near-field communication.

The intuitive definition of the far-field region is the region where the angular distribution of the radiation field is independent of the distance to the antenna, resulting in spherical waves which extends to infinity if uninterrupted. The electric field in this region can generally be expressed as in Equation 2.46

$$\boldsymbol{E}(\boldsymbol{r}) = \frac{1}{r}\boldsymbol{F}(\hat{\boldsymbol{r}})e^{-jkr} \tag{2.46}$$

and the magnetic field is similarly expressed perpendicular to the E-field and by considering the free space impedance. $\boldsymbol{r}$ and $\hat{\boldsymbol{r}}$ is the vector and the unit vector to the far field, hence $\hat{\boldsymbol{r}} = \boldsymbol{r}/r$ and $k = 2\pi/\lambda$. The term $\boldsymbol{F}(\hat{\boldsymbol{r}})$ is the complex far-field function representing the shape of the radiation in the far-field and e^{-jkr} is the phase term. For more details on the relation between the transmitted- and the far-field and the Fourier Transform, plane wave approximation and Bessel functions the reader is directed to [8] and [9].

2.5.3.1 Polarization

The transmitted wave is characterized by its polarization, which explains how the electric- and magnetic field varies in $\hat{x}$ and $\hat{y}$ over time. The fields can either oscillate linearly or rotate elliptically. In communication systems the polarizations can be defined as the co- and cross-polarizations, $\hat{\boldsymbol{co}}$ and $\hat{\boldsymbol{xp}}$ respectively which in turn can be translated to the wanted- and unwanted polarizations. The co-polarization is defined by the transmitting antenna specifications, hence this is the polarization

where ideally all power is concentrated. However, due to imperfections in the antenna design and possible perturbations in the propagation path some power could possibly spill over to the unwanted polarization causing significant losses in signal strength.

Equation 2.47 expresses the electric field in the far-field as a function of the co- and cross-polarizations, E_{co} and E_{xp}

$$\boldsymbol{E}(\boldsymbol{r}) = (E_{co}\hat{\boldsymbol{co}} + E_{xp}\hat{\boldsymbol{xp}})e^{-jkr}. \tag{2.47}$$

A good measure of the polarization alignment is the *polarization efficiency* shown in Equation 2.48. It produces a ratio of the power density of the co-polarization and the power density of the whole wave

$$[e_{pol}]_{dB} = 10log\left(\frac{|E_{co}|^2}{|E_{co}|^2 + |E_{xp}|^2}\right), \tag{2.48}$$

ideally the polarization efficiency is $0dB$.

2.5.3.2 Radiation- and Antenna Efficiency

Due to numerous reasons, the antenna will not radiate all power that is received at the ports of the antenna, leading to the term *radiation efficiency*. If an antenna receives power P_{in} at its ports and radiates with a power of P_{rad} then the radiation efficiency is defined by Equation 2.49

$$e_{rad} = \frac{P_{rad}}{P_{in}}. \tag{2.49}$$

The origins of the losses associated with radiation efficiency are absorption losses (ohmic), which in turn stems from conduction and dielectric losses in the antenna structure [9]. Radiation efficiency is an important quality measure of an antenna and can be used to compare against other antennas. However, as the antenna will be deployed in a system the idea of efficiency must be stretched further to include the antennas interaction with the rest of the system. The reflection- or mismatch efficiency accounts for the power reflected at the input port of the antenna. The schematic in Figure 2.18 illustrates the *Thevenin equivalent circuit*, representing the generator as a voltage source with terminals *a*-*b* serving as the antenna port [8].

The input impedance of the antenna Z_A can thus be written as in Equation 2.50

$$Z_A = R_L + R_r + jX_A \tag{2.50}$$

where R_L is the loss resistance, R_r the radiation resistance and X_A is the reactance. The generator is represented by the impedance Z_G as seen in Equation 2.51

$$Z_G = R_G + jX_G \tag{2.51}$$

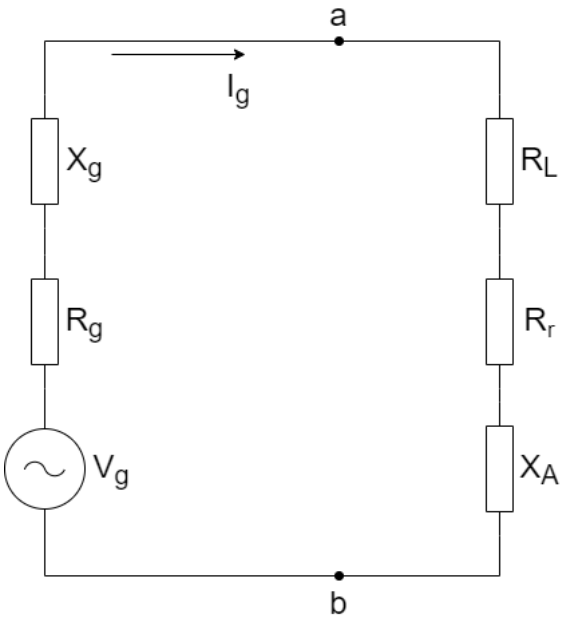

Figure 2.18: Thevenin equivalent circuit for a transmitting antenna.

A mismatch between the impedances Z_G and Z_A will cause reflection at the port resulting in losses. The *reflection coefficient* is defined by Equation 2.52

$$\Gamma = \frac{Z_A - Z_G}{Z_A + Z_G}. \tag{2.52}$$

Limiting reflections is therefore important for efficient energy transfer, hence the matching efficiency e_r is introduced and is written as in 2.53

$$e_r = 1 - |\Gamma| \tag{2.53}$$

The model in Figure 2.18 sometimes fail to convey a realistic scenario as the signal generator is commonly connected to the antenna via a transmission line (TL). This further requires that care is taken to reduce interfaces with different impedances as the impedance of the TL is included on the generator side in Equation 2.52. It can be shown that performing conjugate matching maximizes the power delivered to the load [18], in this case the antenna.

Combining Equations 2.48, 2.49 and 2.53, the antenna efficiency can be determined by simply accumulating these efficiencies. As most calculations related to antenna engineering and microwaves in general are performed in decibels it is convenient to include efficiency calculations in the same manner, seen in Equation 2.54

$$[e_{ant}]_{dB} = [e_r]_{dB} + [e_{rad}]_{dB} + [e_{pol}]_{dB} \tag{2.54}$$

2.5.3.3 Radiation Pattern, Directivity and Gain

Size, shape, feeding mechanism, material, etc. will affect how the radiation is spread in the space surrounding the antenna. The subject of radiation pattern is of great interest as it has a very direct relation to the physical positioning of the antenna and the desired application. Considering the project application, the movable *tag's* position in relation to the *anchors* is non-predictive. This implies that the optimal direction that the tag's antenna should radiate in is unknown. In addition to that, the tag is required to communicate with all anchors at the same time, this calls for an *isotropic* radiation pattern, meaning that it radiates with the same strength in all directions. The isotropic feature is a theoretical concept due to the requirement for a source of radiation, instead the term *omnidirectional* is commonly used indicating that radiation is spread in an almost isotropic manner. Focusing instead on the anchors, their geometrical relation to the tag might be more predictive, thus directing more power in a certain direction could prove beneficial.

To quantify the radiation pattern, the antenna's ability to direct power in a certain direction is referred to as *directivity*. This term has a close relation to what is commonly called gain as to describes how the antenna receives an amount of power and redistributes it in a specific direction. The unit used to measure this is *dBi* or "decibels vs. isotropic", serving as a measure of the antenna's deviation from isotropic behaviour.

Commonly the term directivity is used when discussing the direction of the maximum radiation, this direction is called the boresight illustrated by the axis with the highest radiation intensity. Instead, directive gain is used for explaining the radiation directed in a certain direction θ, ϕ, using spherical coordinates. It is defined as in Equation 2.55

$$[D(\theta,\phi)]_{dBi} = 10log\left(\frac{|F(\theta,\phi)|^2}{|F_{ISO}|^2}\right) \tag{2.55}$$

where F_{ISO} is the complex far-field function of an isotropic radiator. Exchanging the term $F(\theta,\phi)$ for F_0, indicating boresight, yields the maximum directivity D_0.

The *antenna gain* G is, as previously mentioned, closely related to the directivity and often applied in practice as will be seen in Chapter 3. While the directivity only describes direction, the gain also accounts for the antennas ability to radiate. Therefor the maximum antenna gain is expressed as in Equation 2.56

$$G_0 = e_{rad}D_0. \tag{2.56}$$

The more practical approach is however, to include the mismatch efficiency and generality is achieved by expressing the gain as function of angles θ and ϕ as seen in Equation 2.57

$$G_{re}(\theta,\phi) = e_r e_{rad} D(\theta,\phi) \tag{2.57}$$

which is referred to as the *realized antenna gain* [8].

2.5.3.4 Phase Center

As previously explained, the far-field is defined as the region where the radiation field consists of spherical waves, resulting in wave fronts with equal phase. Applying these ideal conditions means that the source of radiation can be traced to a specific point source - the phase center. In real world scenarios, no such perfect phase fronts exists making the phase center a highly theoretical point. In fact, the phase front exhibits small variations within a solid angle in the far-field, and thus the phase center is the point which minimizes this variation [9].

In ranging applications, the phase center has a significant impact on both precision and accuracy. As the phase center is regarded as the apparent source of radiation, this is the location in space that the ranging is referenced to. Attempting to determine the location of the phase center is a difficult task and can yield ambiguous results. Therefor, alternative methods to reliably resolve the *center of radiation* have been proposed, for example in [13].

Ideally, knowing the exact location of the phase center will alleviate some uncertainty in the ranging. However, arguing that the phase center location is perfectly determined and referencing all measurements to this location, might instead induce uncertainties due to the non-perfect phase front. This stems from the variation of the apparent source of radiation depending on the angle of the incident radiation. [12]

2.5.3.5 Fidelity Factor

The previously mentioned factors are all conveniently analyzed in the frequency domain. However, for IR-UWB antennas the most important performance metric, called the *Fidelity Factor* (FF), is measured in the time domain. It is a measure of the antenna's ability to retain the pulse shape between transmission and reception. The fidelity factor is based on a cross correlation of the transmitted and received pulse, maximum correlation yields $FF = 1$ and $FF < 0.5$ indicates significant distortion [10]. A brief mathematical description continues below.

Let $T_S(\omega)$ represent the transmitted pulse in frequency domain and $H(\omega)$ is the transfer function between transmitter and receiver, characterizing the medium. Then the received signal $R_S(\omega)$ is described by Equation 2.58

$$R_S(\omega) = \mathcal{F}\{T_S(\omega)\}H(\omega) \tag{2.58}$$

where the term $\mathcal{F}\{T_S(\omega)\}$ is the Fourier transform of the transmitted signal, thus representing the far-field approximation. The time domain expression for the received signal is obtained by performing an inverse Fourier transform on the frequency domain expression as in Equation 2.59

$$R_s(t) = \mathcal{F}^{-1}\{R_S(\omega)\} \tag{2.59}$$

and similarly, the time domain transmitted signal $T_s(t)$ is the inverse Fourier transform of $T_S(\omega)$. Since it is the shape of the pulse that is of interest, the time domain expressions can be normalized as in Equation 2.60

$$\hat{T}_s(t) = \frac{T_s(t)}{\left[\int_{-\infty}^{\infty} |T_s(t)|^2 dt\right]^{1/2}} \tag{2.60a}$$

$$\hat{R}_s(t) = \frac{R_s(t)}{\left[\int_{-\infty}^{\infty} |R_s(t)|^2 dt\right]^{1/2}}. \tag{2.60b}$$

Finally, the fidelity factor FF is described by the maximum value of the convolution between the transmitted- and received signal according to Equation 2.61

$$FF = max \int_{-\infty}^{\infty} \hat{T}_s(t)\hat{R}_s(t+\tau)dt \tag{2.61}$$

where τ is the time shift between $T_s(t)$ and $R_s(t)$ [10], [11].

2.5.3.6 Group Delay

Complementing the fidelity factor as another time domain measurement, *group delay* is a measure of the delay a certain frequency components is subject to when travelling through a device. If the signal is a continuous perfect sine wave, only containing one frequency component, the whole signal would experience the same delay through the device. However, as ultra wideband pulses contain numerous frequency components, it would require a completely linear phase response to avoid being delayed differently at different frequencies. This is seldom the case in real-world scenarios and certain parts within the bandwidth will "move slower" through the device, thus distorting the shape of the pulse. While this characteristic of the pulse might already have been concluded by determining *FF*, the group delay can be seen as complementary and provides insight to the actual phase response of the pulse, whereas FF is a purely mathematical concept. Hence the group delay being another important measure of quality of high frequency components in an UWB system.

More specifically, the group delay is defined as the derivative of the phase response ϕ with respect to frequency ω, as expressed in Equation 2.62

$$\tau_{group} = -\frac{d\phi}{d\omega} \tag{2.62}$$

where it can be seen that if the phase response is linear, the group delay is constant and this would be the ideal case.

3

Methods

The following chapter outlines the process from deciding system requirements to the design of the evaluation boards and antennas to the method of testing and evaluation.

3.1 System Design

Initially the system requirements are revisited with great detail to outline all necessary specifications and desired performance metrics. Secondly, the hardware choices are specified and motivated based on cost, availability and theoretical concepts derived in Chapter 2. The modular feature is explained as well as the associated issues arising from this feature. The process from design to manufacturing of the PCBs are then described. Lastly, the antenna design process is detailed from initial concepts to simulation to measuring and characterizing.

The main part of the UWB system is the Decawave DW1000 transceiver chip. This is a single six by six millimetre chip that is designed for UWB communication and positioning with a precision in accuracy of 10 centimetres, according to Decawave. The DW1000 has a transmit power of -14 or -10 dBm with a transmit power density of less then -41.3 dBm/MHz, and by an integrated switch it chose if either the transmitter or receiver will be connected to the RF trace. It has six frequency bands with centre frequencies from 3.5 GHz to 6.5 GHz and supports up to 6.8 Mbit/s data rate. The measured data from the DW1000 is acquired by interfacing the chip by a slave-only SPI (*Serial Peripheral Interface*) with a microcontroller, which can then send the data via USB to a main computer.

3.1.1 Choice of Components and Modularity

The components that have been selected for examination is the DW1000 oscillator and antennas. The oscillator is investigated due to the exact timing needed for precision measurement. As mentioned in section 2.5.1, the oscillators stability, which relates to the frequency drift, is believed to have a major impact on the precise timing. Three different oscillators with frequency stability of 2, 10 and 30 ppm will be examined. All oscillators will be of the type *surface-mount device* (SMD).

Two antennas are also designed and manufactured with specific features. One antenna, in this report called octagonal antenna, is a octagonal shaped antenna which has a band-reject function. The theory behind this function is that by minimising the

energy from certain frequencies it is possible to lower the noise level in the system, leading to better precision. A second antenna, called the Vivaldi antenna, is designed in order to get a higher directivity and by that minimising the multipath error.

In order to change and alternate between the components that are supposed to be tested a high order of modularity should be implemented. This is done by expanding the area where the components will be placed in order to easily add and remove, for example, the oscillator and the peripheral components, such as capacitors and resistors, but the modularity also contributes with some uncertainties in the system. By implementing a larger distance between components some of these might end up farther away then necessary and therefore introduce more noise to some parts of the system, which will be described. The way to change the components will also include some uncertainties due to the fact that most of these will placed by hand soldering them to the PCB. The lacking control of heat and solder applied might alter the function of the component.

3.1.2 PCB - Design, Layout and Manufacturing

A *Printed Circuit Board* (PCB) was designed in order to test and evaluate the various components that are intended to improve the precision in ranging. The PCB is made up of four layers of copper and three layers dielectric material, known as FR-4 TG130, which is a glass-reinforced epoxy laminate material. For this project the FR-4 will have a dielectric constant ϵ of typical 4.58 which, however, can vary due to impurities in the manufacturing process of the dielectric. The centre layer of the PCB is called the core, this is made up of fiber glass and resin hardened at high temperature with one copper layer on each side. The two other layers of dielectric material is called the prepreg, which stands for pre-impregnated, and is a glass wave which also is impregnated with resin but not yet hardened. The arrangement of the layer is known as the *stackup*, illustrated in figure 3.1. The four layer stackup, with separate ground plane and power plane, is used in order to minimize the loop current inductance. For a PCB using alternating current it will follow via the path of least impedance, and specifically of least inductance, this happens if the current follows the signal trace back to the source [23].

Even though ground and power planes have relative low impedance, low inductance and is generally adjacent to each other, which results in high capacitance, some problems may still occur. Figure 3.2 depicts a CMOS (*Complementary Metal Oxide Semiconductor*) logic gate. Capacitor C_L is representing all of the capacitance's in the circuit of transistor Q_1 and Q_2. As the capacitance's are not ideal they require some charging time for when the gate switches from one state to another. The capacitance has to charge, or discharge, in order for the gates to reach steady-state. When the states changes from a logical 0 to a logical 1, Q_1 turns on and Q_2 turns off and C_L begins to charge. For a short time in this transition both gates will be on, and therefore a lot of power will be consumed. During this period there will be a short circuit between VDD and VSS through the transistors and C_L. Due to the short circuit there will exist a high current for a short time and voltage at VDD tends to drop until the capacitor is fully charged. The same goes for the other situation

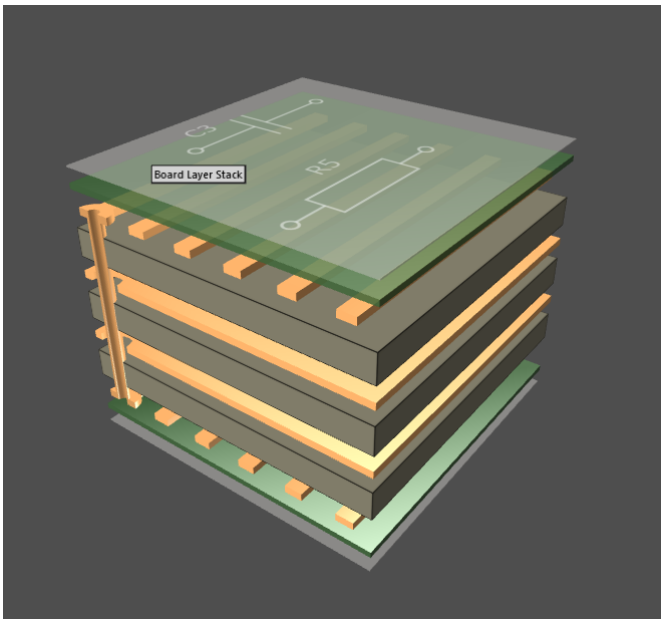

Figure 3.1: Visualization of the four layer stackup.

when changing from a logical 1 to a logical 0, but here C_L is instead discharging and the voltage at VSS tends to rise [23].

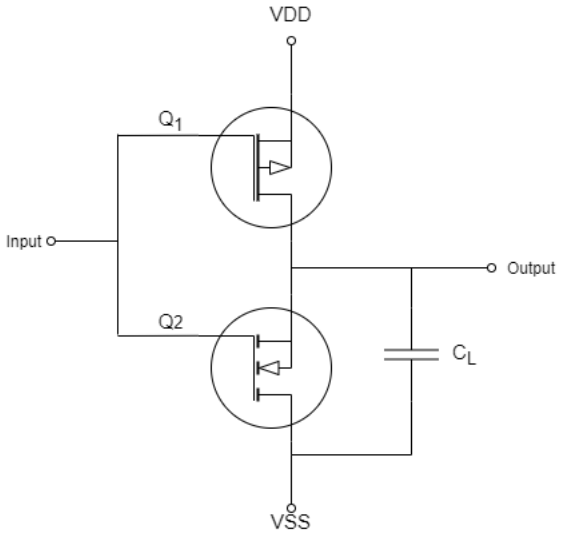

Figure 3.2: Schematic of a CMOS logic gate.

This voltage drop or voltage rise is known as *rail collapse* and *ground bounce*. To minimise these effects it is desirable to implement bypass capacitors. These capacitors are intended to act as current reserves and uphold the positive rail voltage and keep the return rail voltage down, except close to the gate that is switching. For digital circuitry the bypass capacitors keeps the power distribution stable. For analog circuits they act as low-pass filters shorting power transients, i.e. power supply noise, before the ICs [23].

Figure 3.3 shows the placement of all components and the size, in millimetre, of

the designed PCB. Some of the more important parts are marked with a coloured square. As can be seen in the lower right of the PCB, marked with the green square, is the microprocessor *STM32F105RCT6* from STMicroelectronics and the required components such as oscillators and decoupling capacitors. The microprocessors main job is to work as an interface between the Decawave transceiver and the user, delivering ranging data.

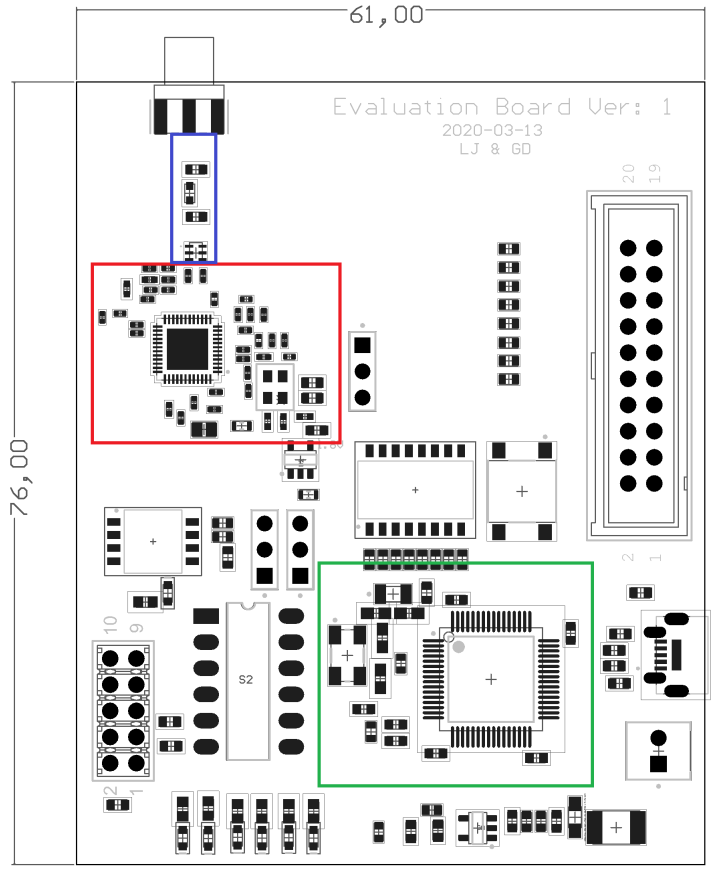

Figure 3.3: Assembly Drawing of the reference card designed by the authors.

Marked with a red square in the figure is the Decawave DW1000 chip together with its oscillator and peripheral components. The DW1000 chip handles the transmitting and receiving of the UWB signal and then process the data in order to evaluate the range.

The final blue square in the upper part of the PCB marks the RF transmission line, including the pi-network. The Transmission line is designed in such a way that it should have an impedance equal, or in the vicinity of, the *Subminiature Version A* (SMA) which is the connector that the antenna will be interfaced with. This is usually 50 Ohms in regards to the industry standard. The pi-network implemented in the RF transmission line is for impedance tuning, which will be described later in this section. To understand how matching between the transmission line and SMA it is suitable to start with how to calculate the impedance of the transmission line, as in Equation 3.1.

$$Z_0 = \begin{cases} \dfrac{60}{\sqrt{\epsilon_e}} ln\left(\dfrac{8d}{W} + \dfrac{W}{4d}\right) & \text{for W/d} \leq 1 \\ \dfrac{120\pi}{\sqrt{\epsilon_e}[W/d + 1.393 + 0.667\, ln\,(W/d + 1.444)]} & \text{for W/d} \geq 1. \end{cases} \tag{3.1}$$

Where W is the width of the microstrip transmission line and d is the thickness of the dielectric substrate and ϵ_e is the *effective dielectric constant*, which in the above equation is the dielectric constant for a homogeneous media. Due to the fact that the microstrip line is facing two different dielectrics, both the inner parts of the PCB as well as the air, leads to field lines in both of these mediums which is hard to analyze. It is therefore necessary to replace the air and the dielectric part of the PCB with a homogeneous dielectric, which is done approximately with Equation 3.2 [18].

$$\epsilon_e = \frac{\epsilon_r + 1}{2} + \frac{\epsilon_r - 1}{2} \frac{1}{\sqrt{1 + 12d/W}}. \tag{3.2}$$

From the above equation one can see that both the dielectric thickness and the width of the transmission line have a major impact on the effective dielectric constant and the impedance of the microstrip transmission line.

The pi-network, which was mentioned earlier, is implemented in order to fine tune the impedance of the transmission line and to realise a good match between the antenna and DW1000 chip to allow maximum power transfer. To understand how a pi-network works it might be helpful to briefly go through the slightly simpler L-section matching network.

Figure 3.4 and 3.5 shows the two ways which an L-section network can be implemented.

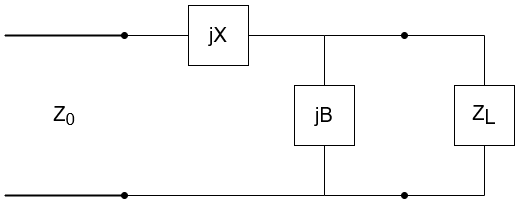

Figure 3.4: L-section network with normalized load impedance inside 1+jx circle.

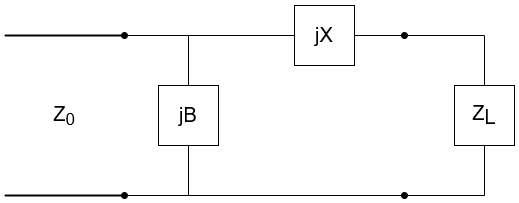

Figure 3.5: L-section network with normalized load impedance outside 1+jx circle.

In figure 3.4 the L-section network is used when the normalized load impedance z_L = Z_L/Z_0 is inside the 1+jx circle in a Smith chart, which is the resistance circle on the impedance Smith chart. Figure 3.5 is for when the normalized load impedance is outside of the 1+jx circle. The X in figure 3.4 and 3.4b represents an inductor if it is positive and a capacitor if X is negative. The same goes for B with the difference that if it is positive it implies a capacitor and for a negative B it implies an inductor. Starting with the circuit depicted in figure 3.4 used for when z_L is inside the 1+jx

circle on the Smith chart, which if $Z_L = R_L + jX_L$, implies that R_L is larger than Z_0. The impedance when looking into the matching circuit, together with the load, must be equal to Z_0 in order to have a impedance matching condition. This can be seen in Equation 3.3

$$Z_0 = jX + \frac{1}{jB + 1/(R_L + jX_L)}. \tag{3.3}$$

One can then divide and rearrange the real and imaginary parts which will then give two Equations as in 3.4a and 3.4b.

$$B(XR_L - X_L Z_0) = R_L - Z_0, \tag{3.4a}$$
$$X(1 - BX_L) = BZ_0 R_L - X_L. \tag{3.4b}$$

B can then be found by solving 3.4a for X and substituting into 3.4b, which will then give a quadratic formula for B as in Equation 3.5a, and X can then be found as in Equation 3.5b

$$B = \frac{X_L \pm \sqrt{R_L/Z_0}\sqrt{R_L^2 + X_L^2 - Z_0 R_L}}{R_L^2 + X_L^2}, \tag{3.5a}$$
$$X = \frac{1}{B} + \frac{X_L Z_0}{R_L} - \frac{Z_0}{BR_L}. \tag{3.5b}$$

Due to the quadratic nature of equation 3.5a it is possible to have both positive and negative values for both X and B, however, this is no problem due to the fact that a positive X suggests an inductor and a negative sign a capacitor. Same goes for the B except that a positive B suggests a capacitor and a negative B suggests a inductor.

The circuit in figure 3.5, which is used when z_L is outside the 1+jX circle in the Smith chart, implies that $R_L < Z_0$. Using the same principle as above but instead of observing an impedance looking in to the matching network with the following load one will see an admittance, which then must be equal to Z_0 in order to full fill an impedance-matched condition, seen in Equation 3.6

$$\frac{1}{Z_0} = jB + \frac{1}{R_L + j(X + X_L)}. \tag{3.6}$$

By dividing and rearranging the real and imaginary components in the above equation, one can find X and B as in Equation 3.7a and 3.7b

$$BZ_0(X + X_L) = Z_0 - R_L, \tag{3.7a}$$
$$(X + X_L) = BZ_0 R_L. \tag{3.7b}$$

One can then find X and B via Equation 3.8a and 3.8b

$$X = \pm\sqrt{R_L(Z_0 - R_L)} - X_L, \tag{3.8a}$$

$$B = \pm\frac{\sqrt{(Z_0 - R_L)/R_L}}{Z_0}. \tag{3.8b}$$

One should note that because of $R_L < Z_0$ the arguments of the square roots will always be positive, and there is also two solutions possible. In order to match an arbitrary load to the input impedance Z_0 of a transmission line the real part of the input impedance of the L-section matching network must be Z_0 while the imaginary part must be zero. This suggests that a matching network needs two degrees of freedom, which in the L-section network is the values of the two components [18], [29].

Problem with the L-section network is that when frequencies gets higher the wavelength will be near the same size as the components leading to undesired effects such as parasitic capacitance and inductance. Another disadvantage with this sort of matching network is that it only has two degrees of freedom. As the Q value is determined by the inverse of the fractional bandwidth, and with the component values X and B already chosen as well as a desired frequency, the Q value is automatically set, and may possibly be to low to function satisfactorily. In order to get a higher Q value a further degree of freedom must be implemented. This can be done by cascading two connected L-section networks, as in figure 3.6.

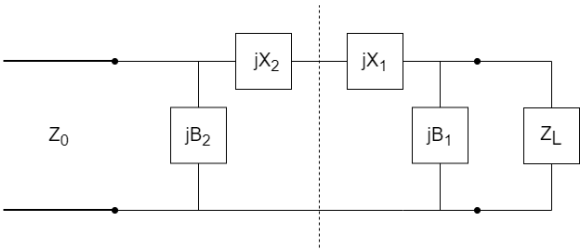

Figure 3.6: A equivalent pi network made up by two lumped L-section networks.

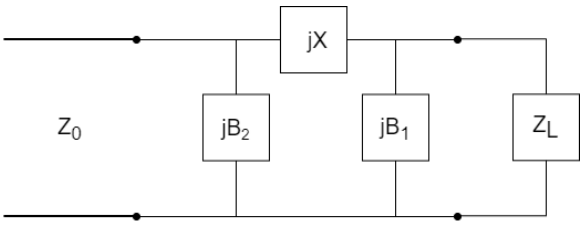

Figure 3.7: Lumped pi-matching network.

In figure 3.7 we can see the so called pi-network which is based on the two cascaded L-section networks, where jX in this case is $jX_1 + jX_2$. The pi-network takes the load and source impedance and match it to a virtual resistance R_V at the junction between the two L-sections, marked by the dotted line in figure 3.6. By using Equation 3.9 one can approximate the Q value by taking the highest resistance of the source or

load impedance. One can also use Equation 3.10 to find the virtual resistance by taking the loaded Q value of the pi-network from the highest Q relating to one of the L-networks [30], [31].

$$Q = \sqrt{\frac{max(R_S, R_L)}{R_V} - 1} \tag{3.9}$$

$$R_V = \frac{max(R_S, R_L)}{Q^2 + 1}. \tag{3.10}$$

The Q value in the above equation can be found by using Equation 3.11 if one knows the frequency for which the circuit should be operating at together with the half power bandwidth.

$$Q = \frac{f_0}{\Delta f} \tag{3.11}$$

Here, f_0 is the centre frequency and Δf is the half power bandwidth.

To determine the component values in the pi-network it is suitable to go back to figure 3.6. By using equation 3.11 and 3.10 the virtual resistance can be calculated. One can then calculate the Q value for the left L-section (Q_{left}) by using equation 3.9. It is then possible to determine B_2 and X_2 via Equation 3.12

$$Q_{left} = \frac{|X_2|}{R_V} = \frac{R_S}{|B_2|}. \tag{3.12}$$

For the right L-section $Q_{right} = Q$ and the component values are calculated as in Equation 3.13

$$Q_{right} = \frac{|X_1|}{R_V} = \frac{R_L}{B_1}. \tag{3.13}$$

Depending on the application of the pi-network, i.e if DC-block is needed, harmonic filtering or elimination of stray reactant's, makes four different versions of the circuit possible [31].

The final PCB layout and 3D model is presented in figure 3.8 and 3.9. Schematics for the PCB can be found in Appendix A

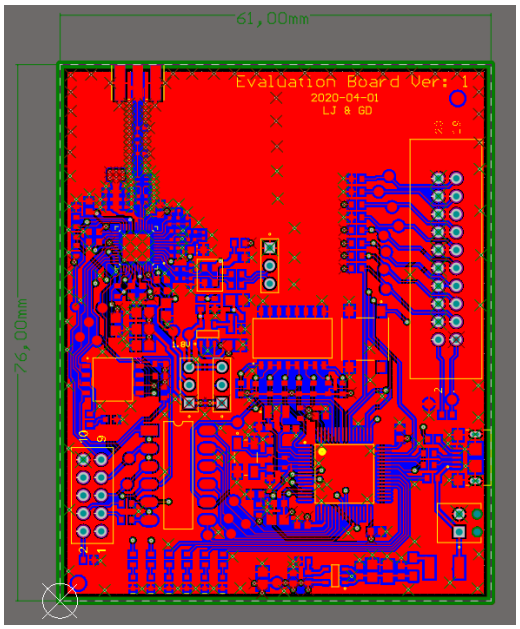

Figure 3.8: Layout of the final reference PCB designed by the authors.

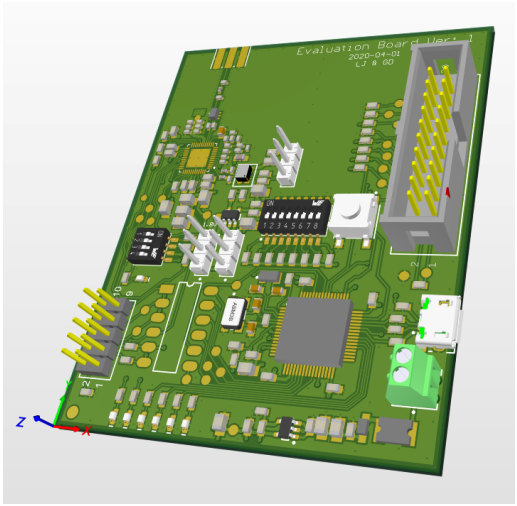

Figure 3.9: 3D model of the final reference PCB designed by the authors.

3.2 Antenna Designs

As two antennas were designed within the project to be compared to the reference omnidirectional antenna with design-files supplied by Decawave, extensive simulation, measuring and characterizations of these own designs was necessary. The two designs were the

1. Octagonal band-reject patch antenna using a complementary split ring resonator
2. Vivaldi patch antenna with tapered corrugations and gratings

which from now will be referred to as 1. *Octagonal* and 2. *Vivaldi*. Both were designed with a goal resonance frequency of ∼4 GHz (corresponding to DW1000 channel 2), yet with two different approaches. The *Octagonal* attempts to limit noise and unwanted signals by rejecting frequency bands not within the channel 2 bandwidth while the *Vivaldi* covers more of the UWB spectrum in combination with higher directivity. Both were designed and simulated in Ansys HFSS.

3.2.1 Octagonal Antenna

The octagonal antenna design is based off concepts from the article in [24], and illustration taken from the simulation process in HFSS can be seen in Figures 3.10 and 3.11.

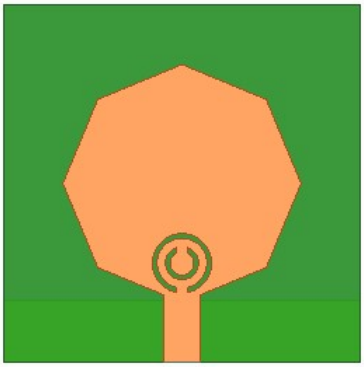

Figure 3.10: Top view of octagonal antenna with feed and CSRR visible.

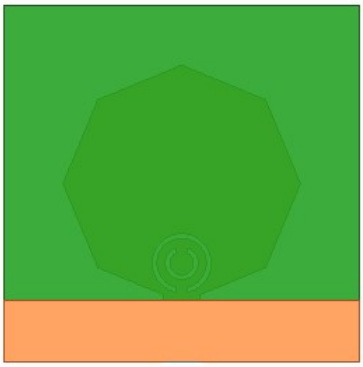

Figure 3.11: Bottom view of octagonal antenna with partially filled ground plane visible.

It is a microstrip fed octgonally shaped patch antenna utilizing a partial ground plane and a *Complementary Split Ring Resonator* (CSRR). Applied in a scenario where communication is desired in all directions, the octagonal shape is a suitable choice for omnidirectional performance [26]. Combined with the partial ground plane, a wider impedance bandwidth is accomplished. This feature limits the amount of the

reactive energy stored by reducing the capacitance between the ground plane and the patch [25], thus acquiring an antenna operating over most of the UWB spectrum. The dimensions have been optimized to achieve a resonance frequency in the vicinity of 4 GHz. The band-reject properties stems from the CSRR, an electronically small ring resonator. While a regular closed microstrip ring resonator would have to be $\lambda/2$ in length to provide these properties at λ, the CSRR can be made electronically small by making use of the mutual coupling between the inner- and outer ring [27].

Figure 3.12 depicts the radiation patterns of the antenna and clearly shows the omnidirectional behaviour. The patterns resembles the typical dipole antenna E- and H-plane radiation.

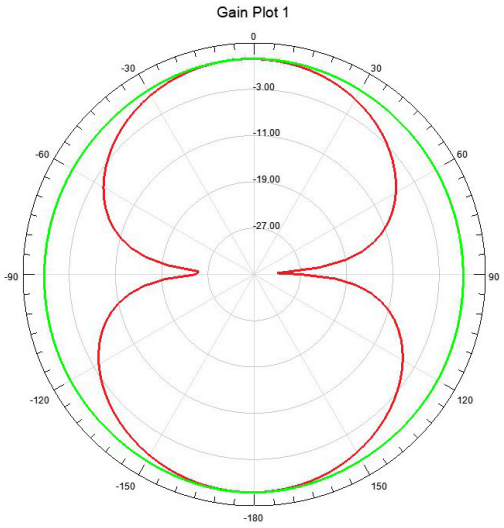

Figure 3.12: Simulated radiation patterns for the Octagonal antenna. E-plane in red and H-plane in green.

An analysis of the dimensions of the octagon, feed line, ground plane and CSRR was performed to acquire low input reflections (S_{11}) and a Ω input impedance within the desired bandwidth. Secondly, the optimization focused on rejecting frequencies between 2-3 GHz and >5 GHz. The resulting simulations of S_{11} and input impedance are seen in Figures 3.13 and 3.14 respectively.

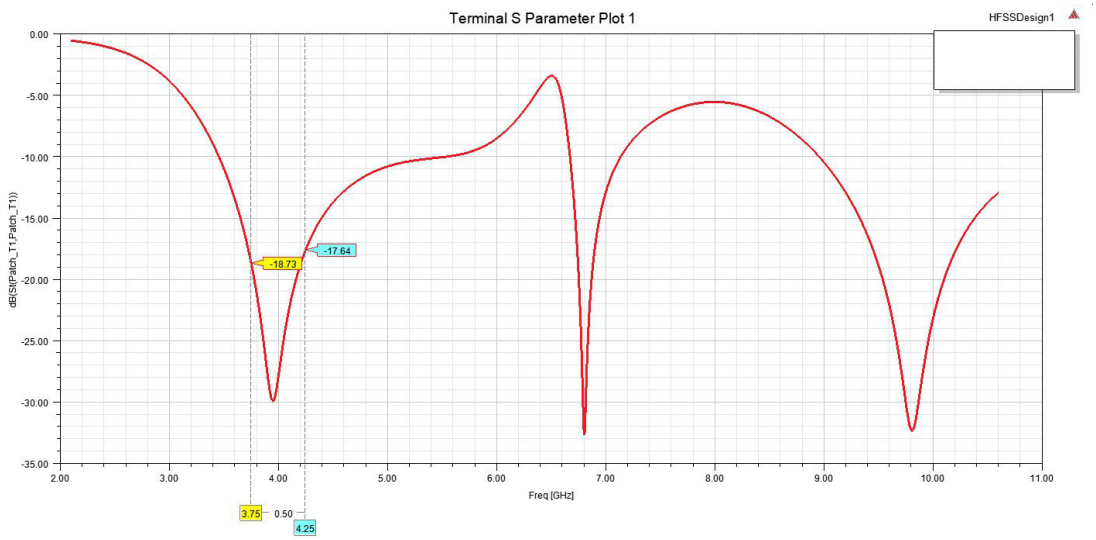

Figure 3.13: S_{11} of Octagonal antenna. Band-reject properties especially visible between 2-3 GHz.

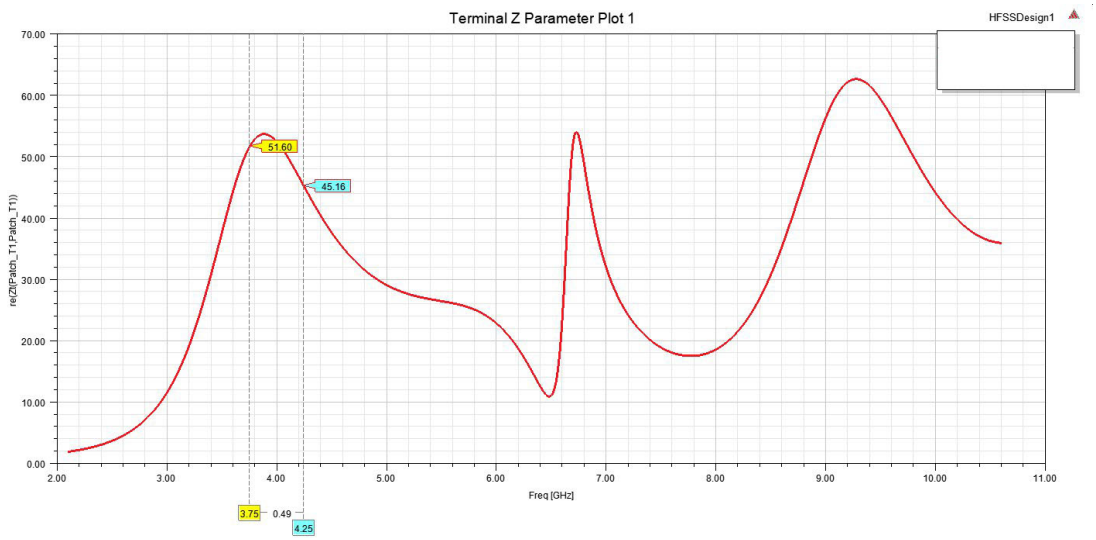

Figure 3.14: Input impedance of octagonal antenna. In the vicinity of the desired 50 ohm.

3.2.2 Vivaldi Antenna

The vivaldi antenna, also known by its more descriptive name as *travelling wave end-fire tapered slot antenna*, is seen in the HFSS simulation environment in Figures 3.15 (top) and 3.16 (bottom). The design is based on the proposal in the article found in [28]

The signal is fed to the antenna via a microstrip on the bottom, terminated in a short circuit. It is coupled to the tapered slot on the top through a 1.0 mm thick FR-4 substrate. In one end it is terminated by a circular cavity and opens up towards the other end (upwards in Figure 3.15. The radiation will propagate in the direction of the increasing exponential tapering as the maximum surface current is found along the inner edges of the tapering. However, surface current also spreads to the outer

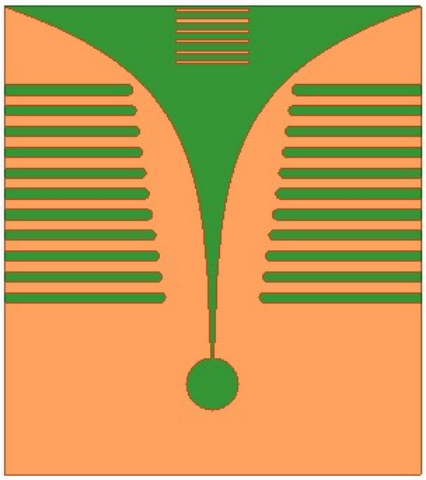

Figure 3.15: Top view of vivaldi antenna with exponential tapering, corrugations and gratings visible.

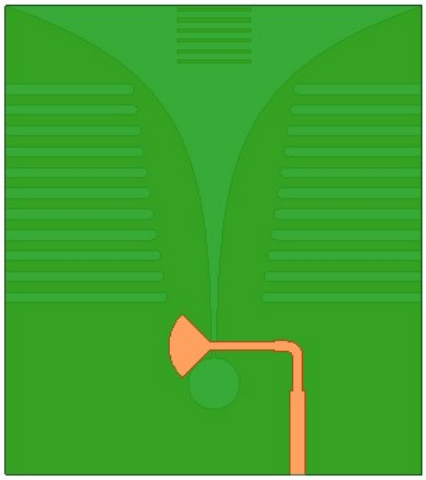

Figure 3.16: Bottom view of vivaldi antenna with feed visible.

edges which reduces the directivity of the antenna. Adding the corrugations seen in Figure 3.15 creates a high impedance region which concentrates the current toward the tapered edges. The grating elements at the open end of the antenna increases high frequency directivity allowing the antenna to exhibit high directivity over almost the whole UWB spectrum [28].

Figure 3.17 illustrates the radiation pattern of the antenna, exhibiting a more directive behaviour visible in the H-plane.

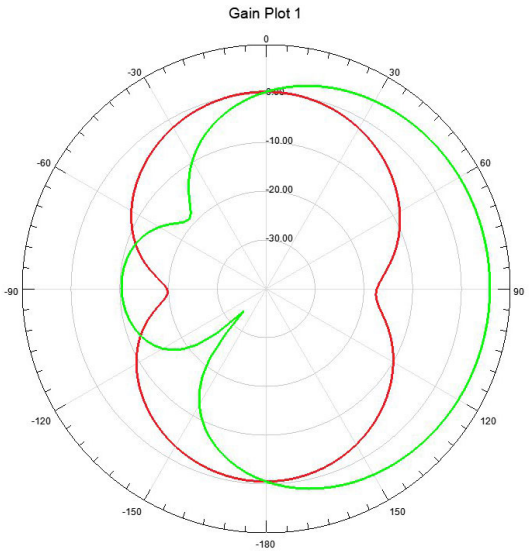

Figure 3.17: Simulated radiation patterns for the Vivaldi antenna. E-plane in red and H-plane in green.

The optimization of the dimensions were done to achieve a low S_{11} for most of the

UWB spectrum, sen in Figure 3.18. The goal of having the lowest input reflections around 4 GHz was not achieved. However, a S_{11} of <-15 dB has a very limited negative effect on the radiation properties. The input impedance seen in Figure 3.19 to be lower than the desired 50 Ω which will limit the performance when connected to a 50 Ω SMA connector.

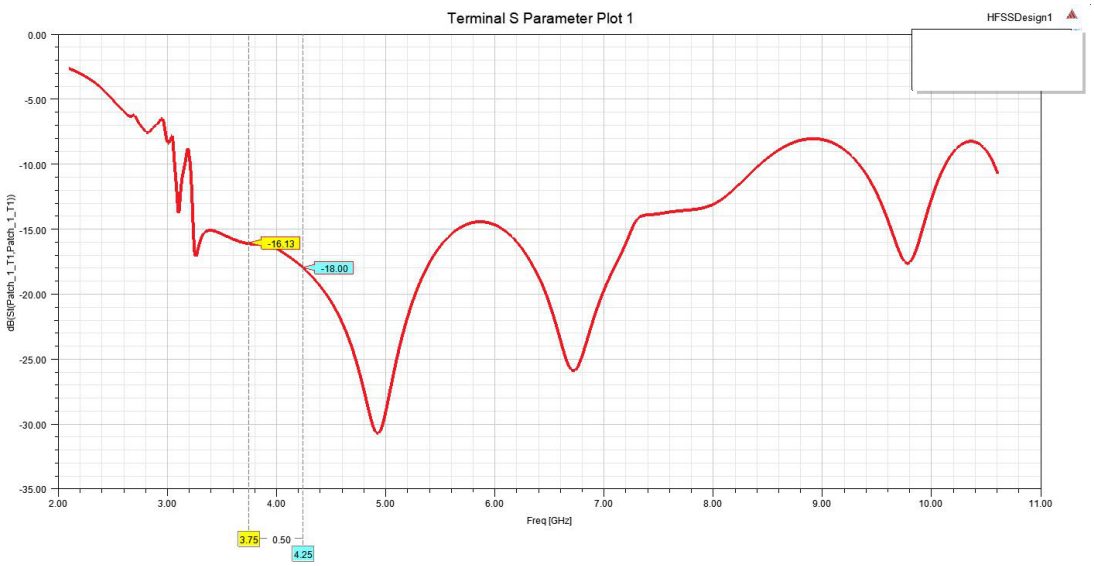

Figure 3.18: S_{11} of vivaldi antenna. Low for most of the available UWB channels.

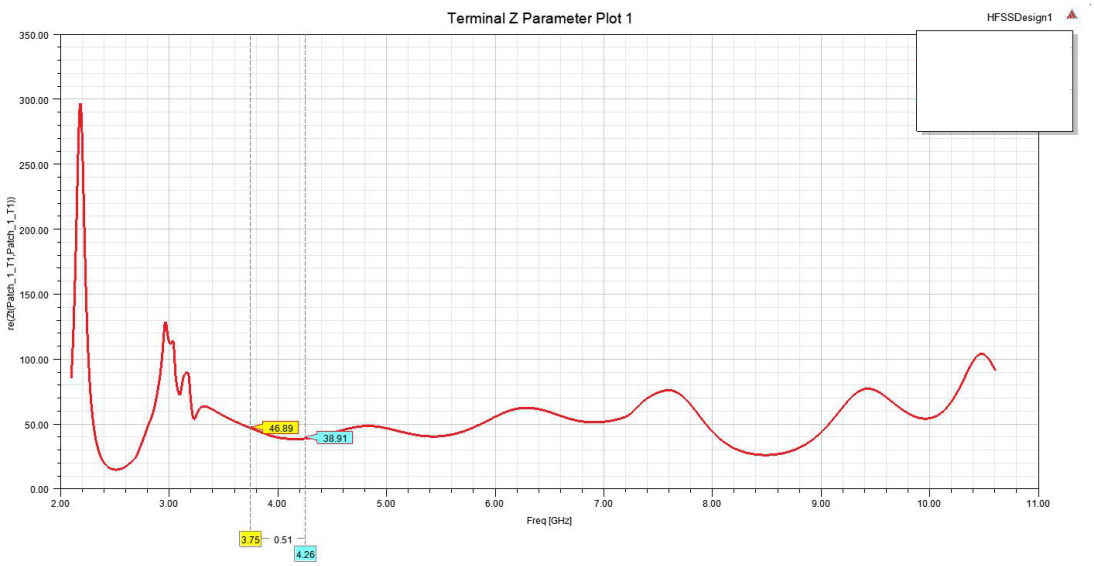

Figure 3.19: Input impedance of vivaldi antenna. Slightly lower than the desired 50 ohm.

3.2.3 Characterization

To derive a connection between the results and the impact of the different antennas, the antennas underwent a series of measurements to acquire their characteristics. This section outlines the measurement setups and displays the results along with comments on performance and similarities to simulated results. The measurements were performed in an anechoic chamber at RISE, department of metrology in Borås. An anechoic chamber is a room which limits reflections and interference within a certain frequency range, in this case RF. This is done by covering the inside walls, ceiling and possibly the floor with material with high absorbing properties. It is also sealed off from its surroundings by an outer metal layer (commonly a Faraday cage) to reduce interfering radiation from the outside. This allows measurements to be made which isolates the behaviour of the equipment under test [8]. Photographs from inside the chamber used in this project is shown in Figures 3.20 and 3.21.

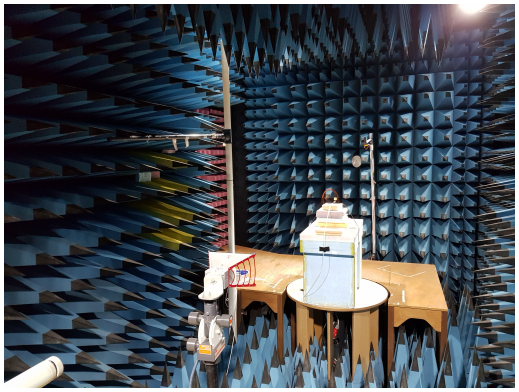

Figure 3.20: Anechoic chamber with standard horn antenna visible.

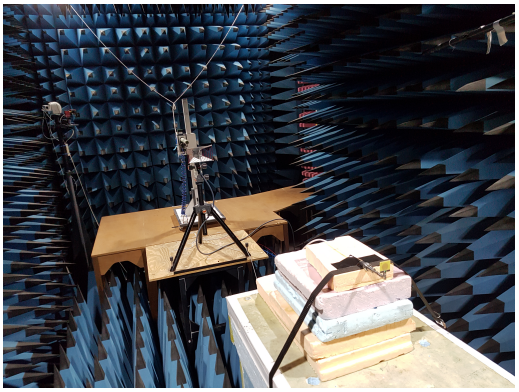

Figure 3.21: Anechoic chamber with the octagonal antenna visible during measurement.

As can be seen, the chamber is of the type *fully anechoic room* meaning that there are absorbers present on the floor. Other equipment present, such as stands are made of an absorbing plastic material. The plywood podium and the styrofoam table are also poor reflectors at these frequencies.

The measurements are based on the communication between the transmitting standard horn antenna and the receiving *antenna under test* (AUT). The horn antenna has a well known gain, polarization and radiation pattern and transmits a continuous wave from approximately 1- to 11 GHz with a stepsize of 50 MHz. This allows the characteristics of the AUT to be determined as there is minimal influence from the surroundings and the effects of the transmitting antenna can be eliminated as they are known. The measured data is acquired by connecting the AUT to a network analyzer which measures the S-parameters. All data is valid both in a transmitting- and a receiving situation due to the reciprocity of the AUT [9].

The reference antenna, Decawave's WB002 antenna, was manufactured along the vivaldi- and octagonal antennas. Figure 3.22 shows the manufactured reference antenna which underwent the same characterization procedure as the other antennas. This allows more accurate comparisons between antennas.

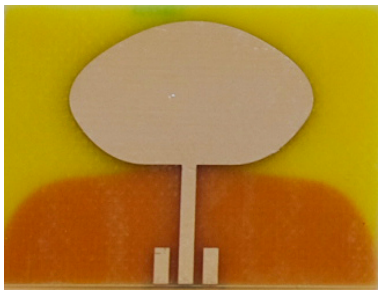

Figure 3.22: Decawave WB002 antenna manufactured, used as a reference in the test setup.

Initially, the radiation pattern was measured by rotating the podium supporting the AUT 360 degrees with a stepsize of 1 degree. Figures 3.23, 3.24 and 3.25 illustrates the results of the radiation pattern measurements for the reference-, octagonal- and vivaldi antenna respectively. Contrary to the simulation results in Figures 3.12 and 3.17 the red colour represents the H-plane in the measurement results and black the E-plane, please excuse this source of confusion.

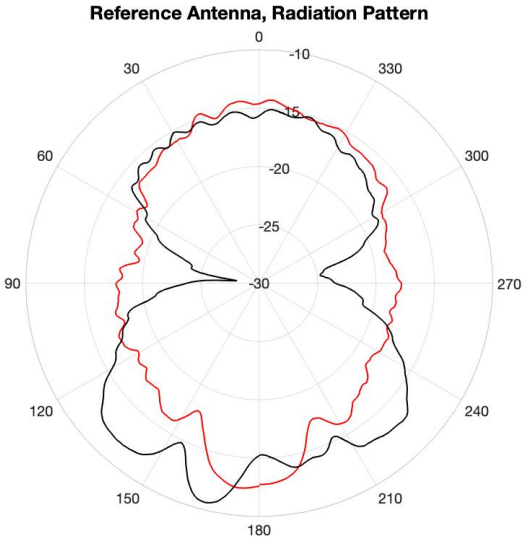

Figure 3.23: Measured radiation patterns for the reference antenna.

The reference antenna pattern in Figure 3.23 showcases the dipole behaviour with the ”eight shaped” E-plane and the rounder H-plane, assuring omnidirectional radiation. It bears some similarity to the octagonal antenna pattern in Figure 3.24, the main difference being that the octagonal antenna has more energy directed in the back lobes. This is an undesired feature as it becomes less susceptible to radiation in some directions. The vivaldi antenna pattern in Figure 3.25 depicts the directive behaviour expected from the vivaldi antenna. The H-plane bears a strong resemblance to the simulated H-plane in Figure 3.17.

The next measurements were performed to determine how well the antenna is matched to 50 Ω and also to obtain the boresight gain. The matching is measured by again transmitting a signal from the standard horn antenna and studying the reflection at

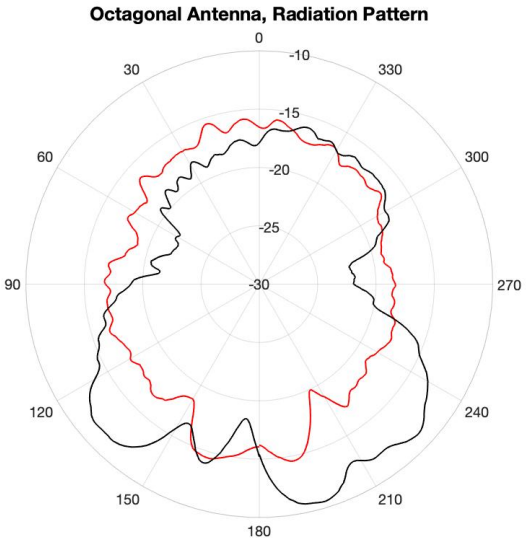

Figure 3.24: Measured radiation patterns for the octagonal antenna.

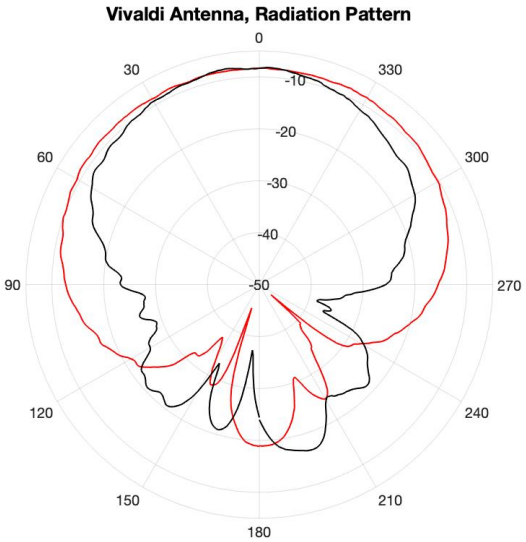

Figure 3.25: Measured radiation patterns for the vivaldi antenna.

port 2 of the AUT, meaning that the parameter measured is actually S_{22}. However, due to the reciprocity of antennas $S_{22} = S_{11}$. The boresight gain, also known as maximum- gain or directivity, is measured by aligning the standard horn with the AUT in the axis of maximum radiation. The transmission between these antennas are then compared to the transmission between two standard horn antennas at the same distance. This technique is called *gain-transfer* [8] and the steps to acquire the boresight gain is described below.

Using Friis' transmission equation, Equations 3.14 and 3.15 are obtained

$$G_t + G_T = 20log_{10}\left(\frac{4\pi R}{\lambda}\right) + 10log_{10}\left(\frac{P_T}{P_t}\right) \tag{3.14}$$

$$G_t + G_S = 20log_{10}\left(\frac{4\pi R}{\lambda}\right) + 10log_{10}\left(\frac{P_S}{P_t}\right) \tag{3.15}$$

where the AUT has gain G_T, receiving horn has gain G_S and transmitting horn has gain G_t. Subtracting Equation 3.15 from Equation 3.14 yields Equation 3.16

$$G_T - G_S = 10log_{10}\left(\frac{P_T}{P_t}\right) - 10log_{10}\left(\frac{P_S}{P_t}\right) \implies G_T = G_S + 10log_{10}\left(\frac{P_T}{P_S}\right) \tag{3.16}$$

resulting in the final expression for the gain of the antenna under test.

The matching of the reference antenna, illustrated in Figure 3.26, shows optimal performance around 6 GHz while at the operating frequency around 4 GHz the matching is poorer, hovering around -10 dB, which is an acceptable level. The boresight gain would ideally be 0 dBi for the desired operating frequency as this would indicate the omnidirectional property. However, as can be seen in Figure 3.27 the boresight gain is actually below 0 dBi at 4 GHz which could be due to the energy lost from the non-optimal matching. Boresight gain is also frequency dependent and the measurement in Figure 3.27 implies that the line of communication is the boresight at around 7 GHz.

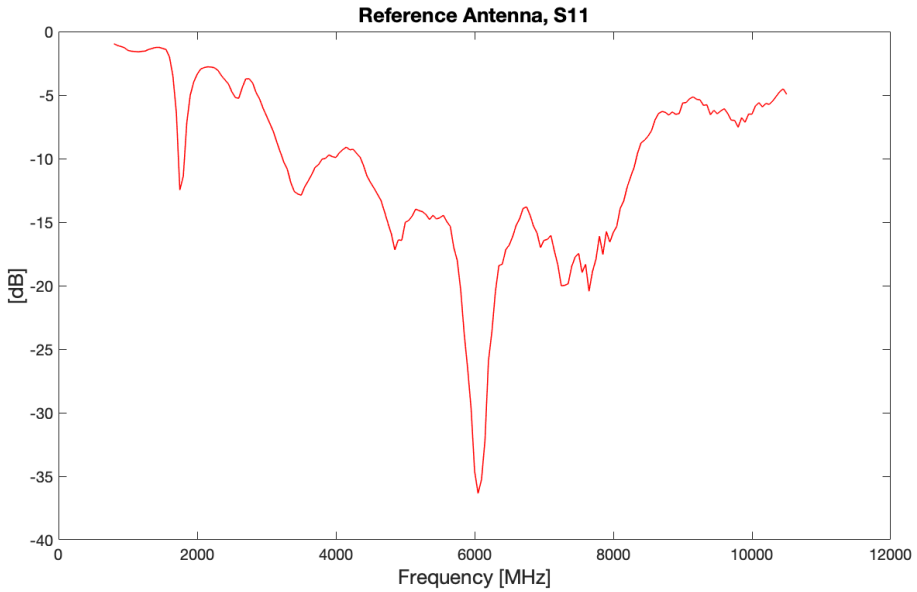

Figure 3.26: Measured S_{11} of reference antenna.

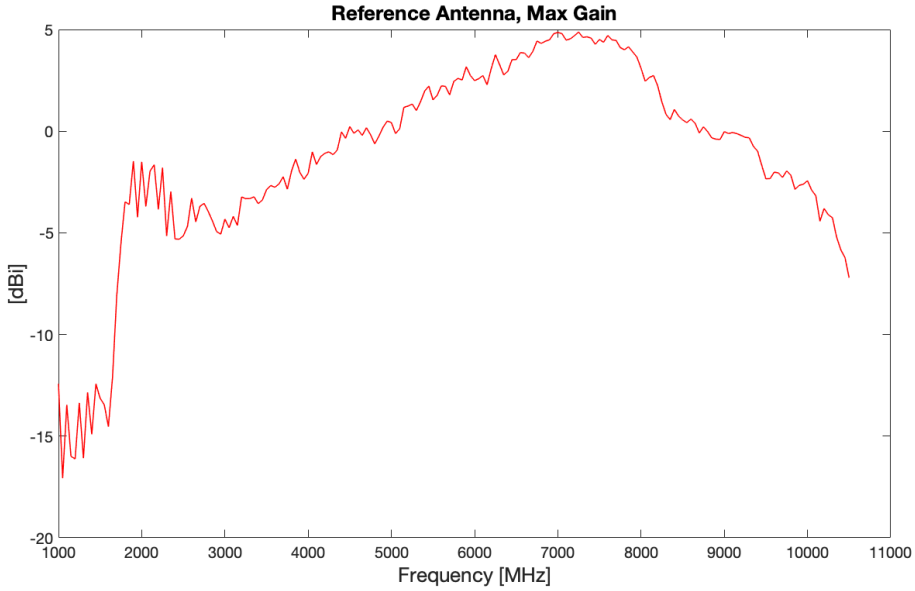

Figure 3.27: Measured boresight gain of reference antenna.

The band-reject properties are clearly visible in the measured S_{11} of the octagonal antenna in Figure 3.28, illustrating excellent matching around 4 GHz and rejecting frequencies, especially at the lower end of the spectrum. The measured S_{11} bears many similarities to the simulated S_{11} in Figure 3.13, although the dip below 10 GHz is missing in the measurement which could be a result of the limited frequency resolution. Similarly to the reference antenna, a boresight gain of 0 dBi is desired. However, Figure 3.29 shows a lower gain level throughout the spectrum with a distinct dip between 6- and 7 GHz. It is possible that a resonance occurs at this frequency causing a null in the particular direction that is measured.

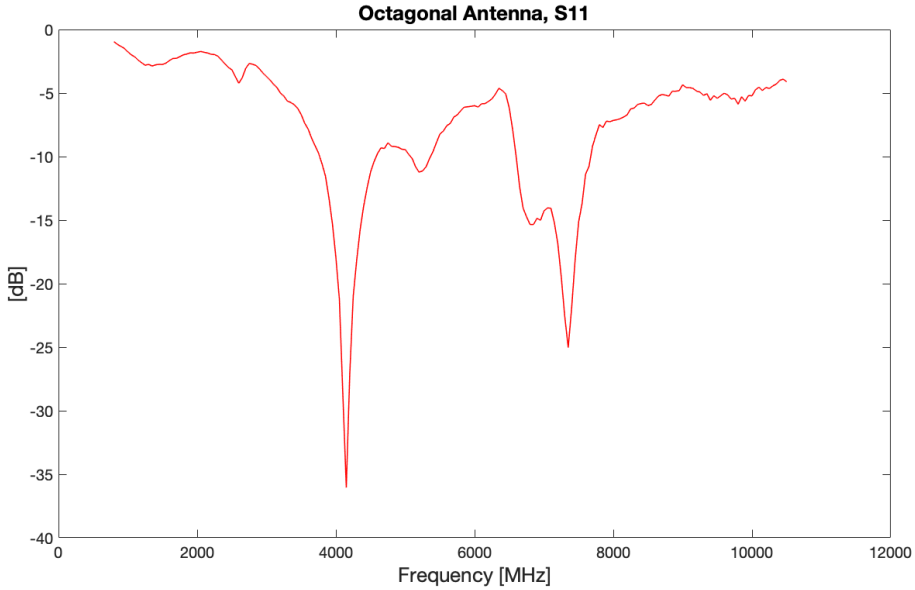

Figure 3.28: Measured S_{11} of octagonal antenna.

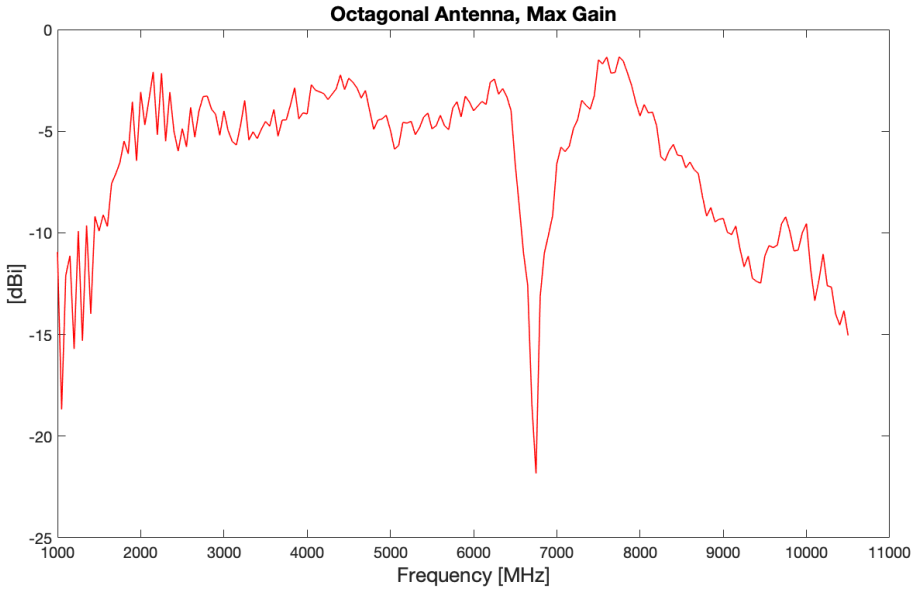

Figure 3.29: Measured boresight gain of octagonal antenna.

The vivaldi antenna exhibits a very good matching from 3- to 7 GHz, as seen in Figure 3.31. It also possesses plenty of similarities to the simulated S_{11} in Figure 3.18, most importantly the aforementioned range where it mostly stays below -15 dB, this can be seen in figure 3.30. Figure 3.31 showcases the high directivity of the vivaldi antenna, measuring approximately 5 dBi at 4 GHz in boresight.

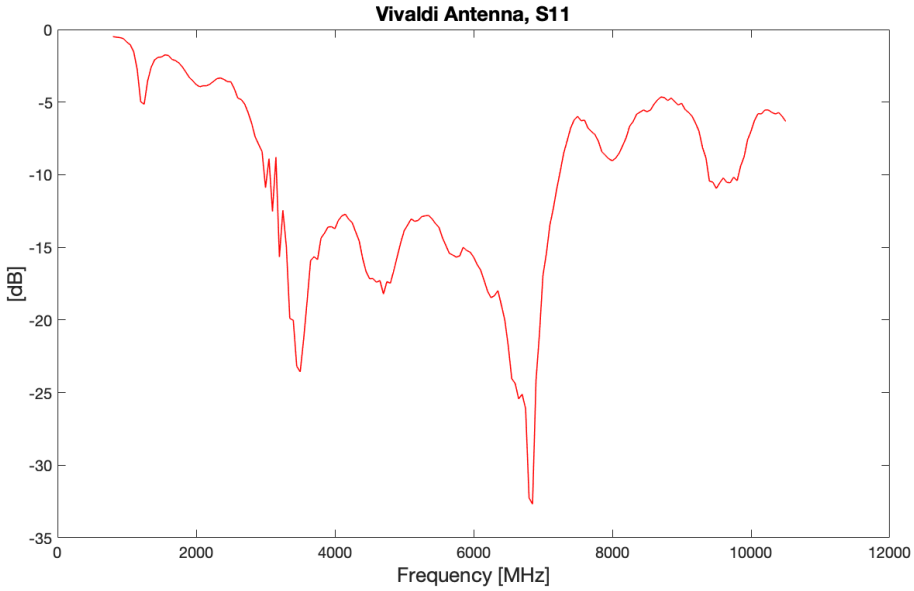

Figure 3.30: Measured S_{11} of vivaldi antenna.

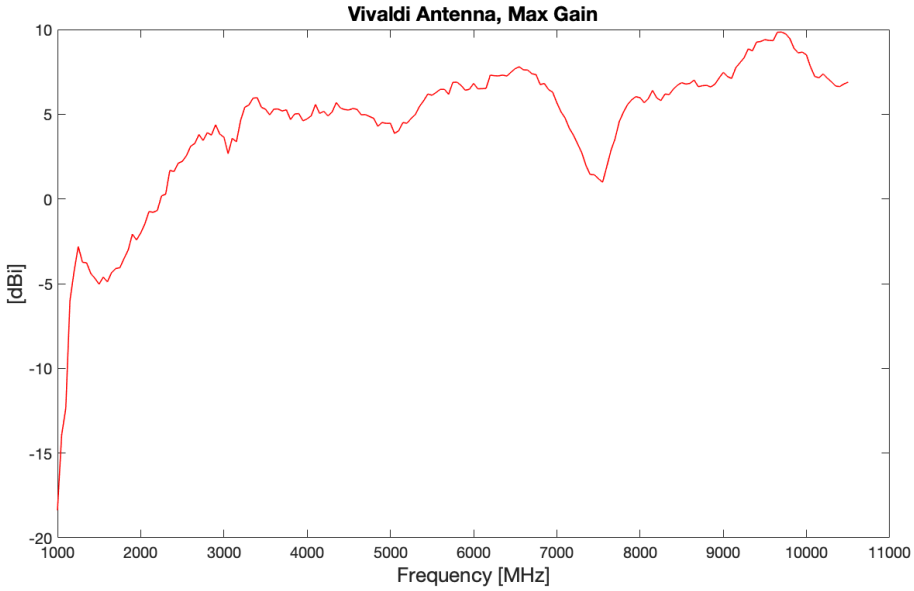

Figure 3.31: Measured boresight gain of vivaldi antenna.

3.3 Implementation and Realization

The evaluation PCB and the patch antennas were manufactured by *Seeed Studios* in Shenzhen, China [32]. The finished products can be seen in figure 3.32 and 3.33 where a battery of the type AA has been added in order to illustrate the size of them.

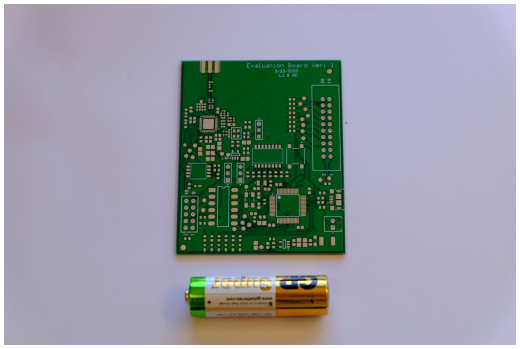

Figure 3.32: Evaluation board PCB before mounting of components. AA battery for size reference.

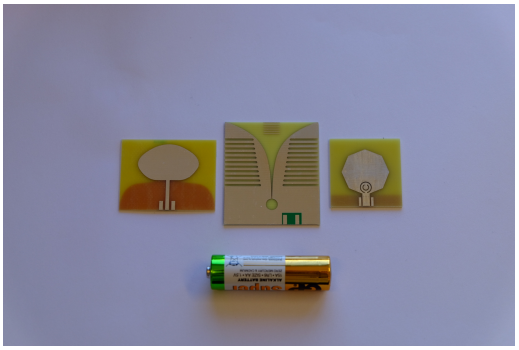

Figure 3.33: Printed Reference-, Octagonal- and Vivaldi antenna in that order. AA battery for size reference.

Figure 3.34 shows the RF trace in a zoomed in perspective. What should be noted here is the lack of components on the pads, which are the small squares with a silver shade. The next part in the building process is to apply soldering paste on all pads and then place each component on its intended location, this is done with the use of a microscope and tweezers due to the small size of the components, they can be as small as 1.0 by 0.5 mm.

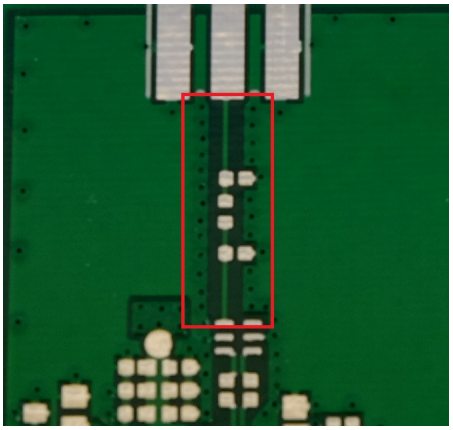

Figure 3.34: RF-trace without components highlighted.

After all components have been placed, the PCB will be put in an infrared oven. Here it will be exposed to a heating cycle which melts the solder and causes the components to be attached. However, some components contained plastic that can not withstand the heat from the oven, they had to soldered by hand afterwards. This

also applies for the other oscillators that are intended to be tested.

When all the components finally were in place, the card was connected to a power supply. A low voltage was then applied and the current was limited to investigate so that there were no short circuits. Troubleshooting had to be done if it was detected that the wrong current or voltage was measured.

If the card passed the tests described above, one could then proceed with the programming of the microprocessor. This was done with a device known as J-Link from the company SEGGER along with the program STM32CubeMX and STM32Cube IDE from STMicroelectronics. After successfully programming the PCBs they were connected to a PC together with the DecaRanging RTLS software in order to see if ranging was established between two PCBs.

3.4 Test and Evaluation

Careful thought must be put in to the design of the test system to ensure minimum errors. The following sections will describe how the measurement models are built and how the testing will be conducted. First the *Line-of-Sight* (LOS) and *Non-Line-of-Sight* (NLOS) setup will be described, followed by the implementation of these two in a real environment. The methods for evaluating the measurement data will then be described along with the limitations of the experiments.

3.4.1 Precision Test Setup

The basis of the precision test are several pre-determined measurement points (locations) forming tracks which the tag will be moved along. All locations as well as anchor- 1 and 2 are referenced to the location of anchor 0 which is found at location (0,0,z) in the local coordinate system. All range data are also transmitted to anchor 0 which in turn is connected to a laptop via an USB cable. The position is estimated in the DecaRange RTLS PC application and shown graphically on the GUI also provided by Decawave. The anchors are mounted on top of tripods resulting in the antenna being at an approximate height of 1.57 meters above the ground.

The precision test is divided in to several parts, the initial test is the reference test using what was determined as the reference component setup. Afterwards, the components are switched one at a time and the precision test is performed again. All tests includes evaluation of precision in a LOS- and a NLOS environment, these environments are described in Sections 3.4.1.1 and 3.4.1.2.

3.4.1.1 LOS Environment

The LOS environment setup is illustrated in figure 3.35. The test is done in an office environment and therefore there are objects that could possibly interfere with the measurements at some locations such as a desk, which is depicted in the top left corner of the figure. The anchors are placed relative to a 3x3 meter square, and a Cartesian coordinate system is implemented in order to position the anchors and locations relative Anchor 0, which is the origin. Anchor 1 will then have a position of (3,1.5,1.57) meters and Anchor 2 (3,-1.5,1.57) meters. For when the anchors are equipped with directional antennas they will be placed so that the main lobe is approximately pointing to the centre of the square. There are total of 70 locations where the device working as a tag will be placed, each with a distance of 30 centimetres to each other and a minimum of 90 centimetres to each anchor. The tag will also be placed on a movable device with a height of 37 centimetres from the ground. As the tag changes position it is allowed a settling time in order to minimize the randomness in the measurements. The tag will then stay in that position and the position estimates will be logged for ten seconds in order to acquire an appropriate amount of data for statistical evaluation.

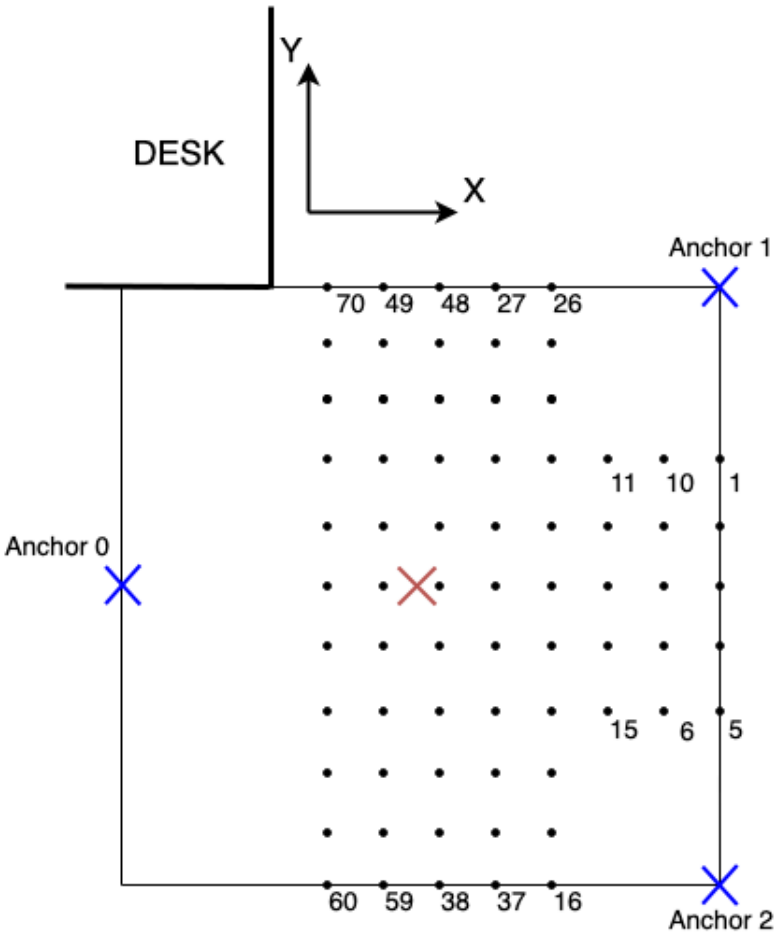

Figure 3.35: Layout showing the LOS measurement. Locations for measurements are marked with small black dots and numbered. Anchor placements are marked with blue crosses and the red cross marks the centre of the measuring area.

3.4.1.2 NLOS Environment

Figure 3.36 shows the placement of anchors and measurements points for the NLOS test. As in the LOS test there is a Cartesian coordinate system where anchor 0 is set as the origin. Anchor 1 is placed at (-1.20,6.5,1.57) meters and Anchor 2 is placed at (3.80,4.50,1.57) meters. The tag will use the same movable device as in the LOS test. There are 21 locations where six of these are placed under a office desk in order to simulate NLOS circumstances. The desk are covered with traditional office equipment such as computer screens, keyboards and other accessories. The height of the desk is set to 77 centimetres from the floor to the top side of the desk, and under the desk are metal structures and cables. The measurement points located on the right side in the figure is placed with a distance of 30 centimetre from each other in the Y direction and one meter from the measurement positions in the X direction. There is also a two meter distance from Anchor 2 to the closest measurement point. The other measurement points are placed so that there is a distance of one meter to each other in each direction. As for the LOS case the tag will be allowed a settling time and then the position estimation will be logged for ten seconds to get an satisfying amount of data.

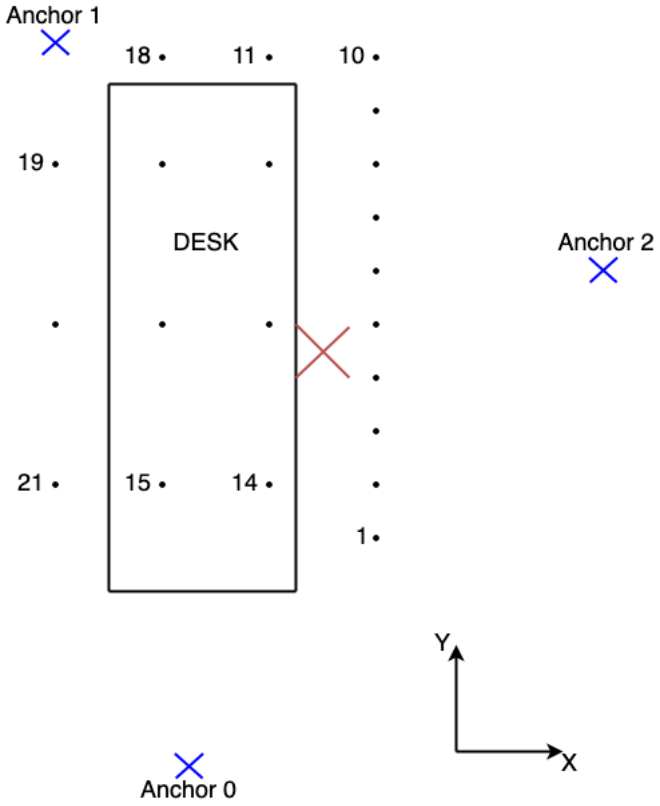

Figure 3.36: Layout showing the NLOS measurement. Locations for measurements are marked with small black dots and numbered. Anchor placement are marked as blue crosses and the red cross marks the centre of the measurement area.

3.4.1.3 Realization of the Test Environment

The LOS test setup in the office environment, described in section 3.4.1.1, can be seen in figure 3.37. Here one can identify the placement of anchors and tag, marked with a red circle. One can also distinguish the locations, seen as white spots, on the floor. The office environment where this test is conducted contains a variety of objects and material, which can be observed in the figure. This complex environment will affect the result due to the concepts discussed in Section 2.3, such as reflections absorption losses.

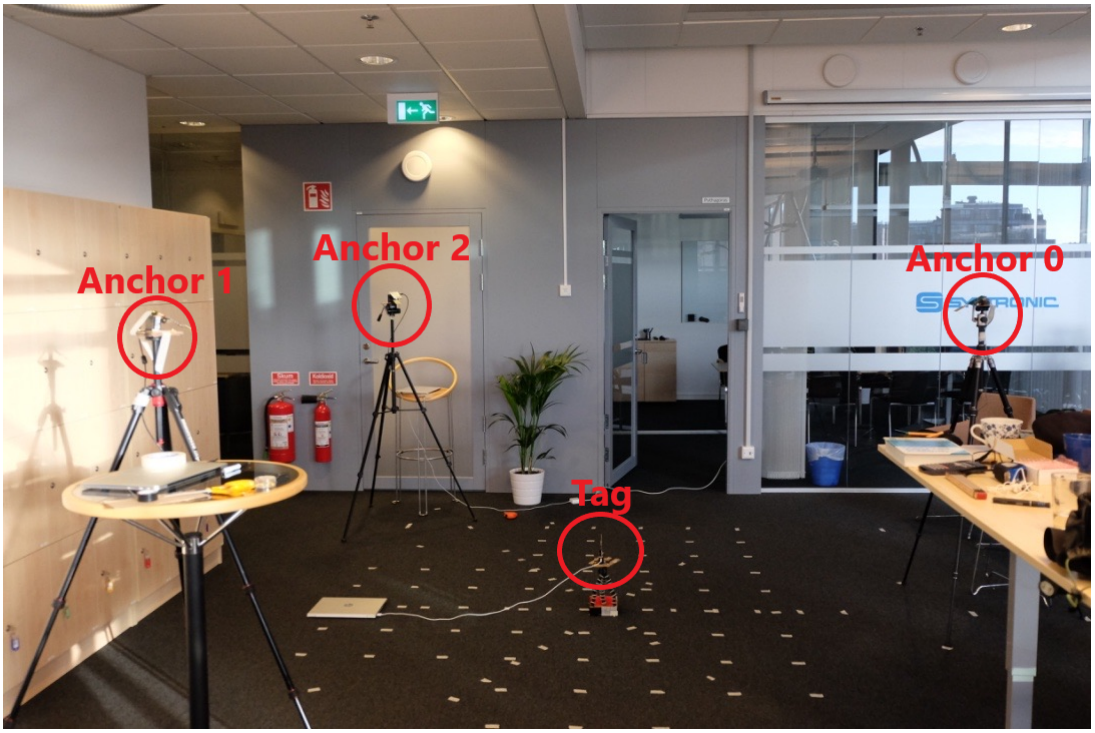

Figure 3.37: Placement of anchors in the LOS setup. White dots on the floor are the chosen locations where the tag will be placed to acquire position estimates. For a more detailed overlook of the positions see figure 3.35 in previous section.

As mentioned in the previous section, to achieve high repeatability in the positioning of the tag at the different locations the tag was placed on a movable device. To accurately place the tag at the same location for every test a crosshair was implemented on the movable device and the distance to each point intended for measure was carefully marked, illustrated in figure 3.38. The tag is placed above the crosshair centre and is not moved during the whole test.

The setup for the NLOS test is shown in figure 3.39, explained in section 3.4.1.2. The NLOS test is also performed in an office environment, as in the LOS test, but the difference here is that office equipment is used as blocking objects. Figure 3.40 depicts the difficult environment that the desk area represent with metal structures, cables and wood blocking the signal path between anchors and tag at certain locations.

Another view of the NLOS test setup can be seen in figure 3.41 which is taken behind anchor 2.

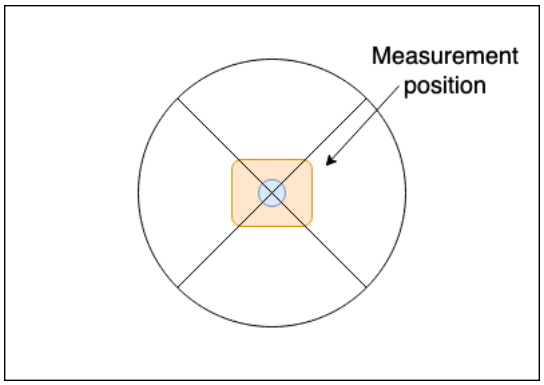

Figure 3.38: The crosshair of the movable device placed accurately over the marked measurement position on the floor. The tag is located right above the crosshair centre.

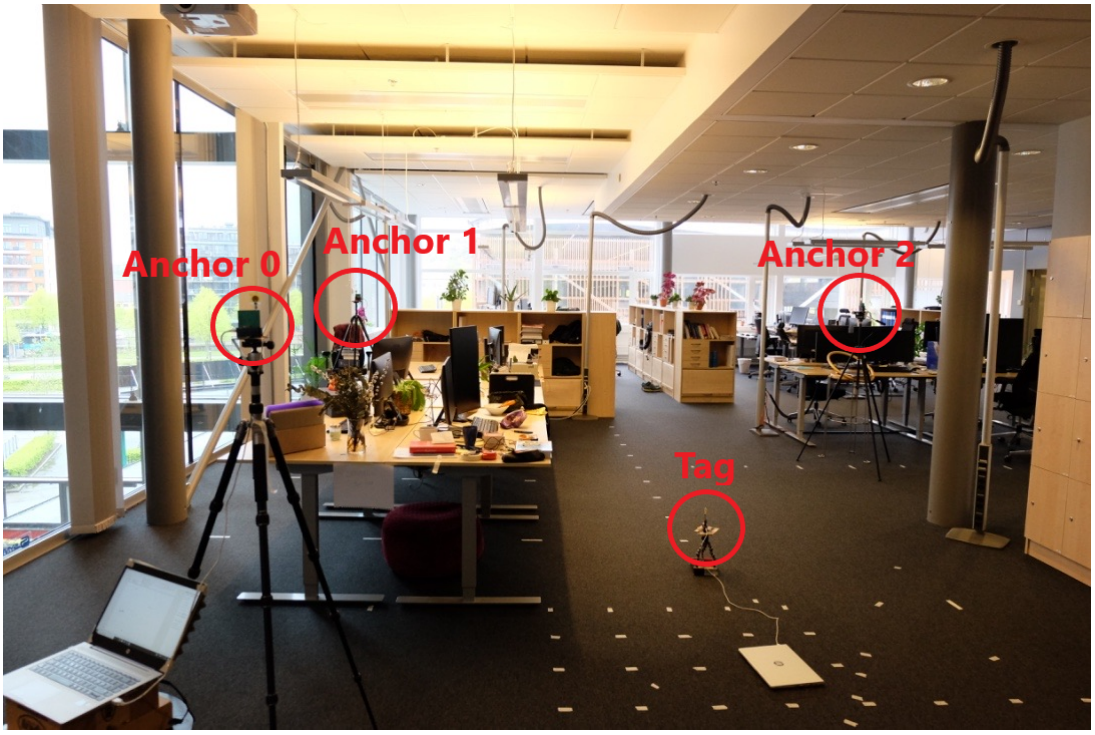

Figure 3.39: Overview of the NLOS setup where anchors and tag are marked. The tag locations are the white marks on the floor, as seen in figure 3.36

When the test uses the Vivaldi antenna, with a more directional main lobe, then the anchors needs to be repositioned in order to point the main beam of the antenna towards the centre of the measuring area. The way this is done is illustrated in figure 3.42 which shows an anchor placed on a tripod. The angle with which the anchor is placed is not calculated but placed approximately aimed towards the centre point seen as red crosses in figure 3.35 and 3.36.

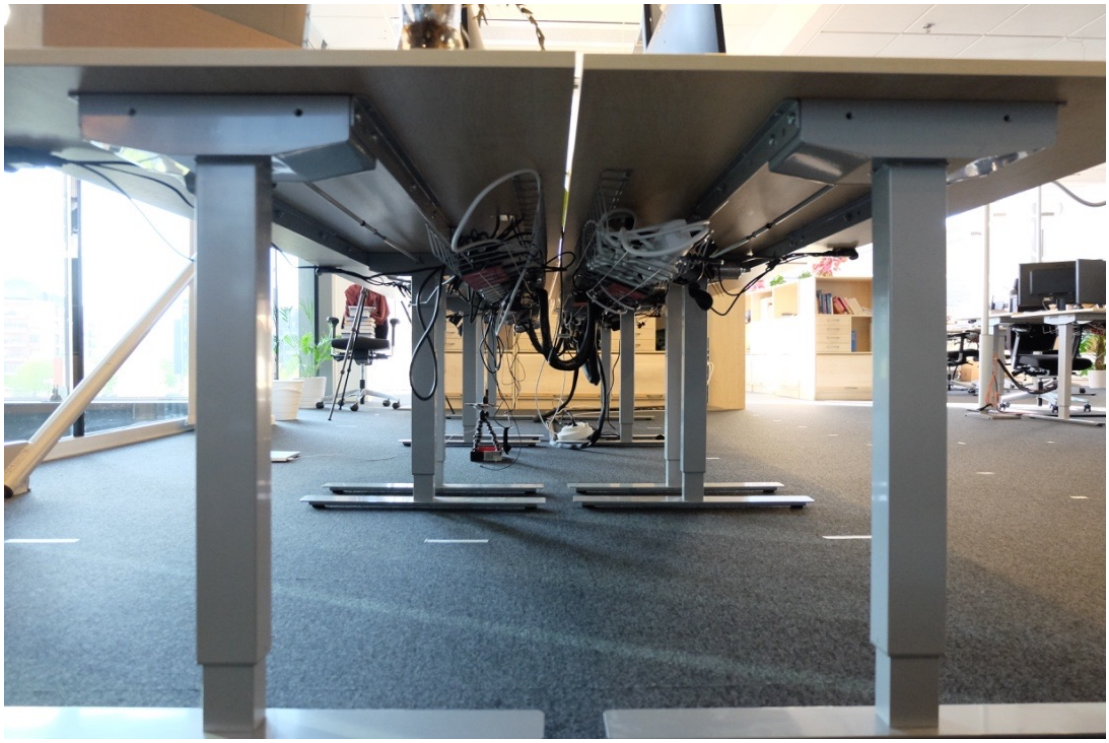

Figure 3.40: This figure shows the difficult environment under the desk which is used for the NLOS test.

Figure 3.41: NLOS setup seen from anchor 2 position.

Figure 3.42: Vivaldi antenna directed towards the centre of the measuring area.

3.4.2 Methods for Evaluation

The data acquired from the precision tests are contained in log-files which include all range results, position estimates and error messages. These log-files were processed to include the location number as described in Figures 3.35 and 3.36, the number of position estimates and the position estimate in x,y,z-coordinates. The number of position estimates vary depending on the difficulty of receiving the timestamps transmitted between tag and anchors, some locations resulted in upwards 40 position estimates while others had none or just a few. The exact number of locations are presented Appendix B.

As stressed previously in this report, the desired quality of measurement is high repeatability. Therefore, the measure referred to as *error* in following sections is a measure of the closeness of the position estimates for a specific location. As described in Section 3.3, the fourth anchor was not included in the test setup and thus the height component z is subject to ambiguity. The evaluation will therefore focus on the measurements in the x,y-plane. Following is a description of the methods used to evaluate the quality of the measurements along with critique directed toward these same methods.

For a specific location, the arithmetic mean of all x- and y estimates were calculated according to Equation 3.17

$$\mu = \frac{1}{N}\sum_{i=1}^{N} A_i \tag{3.17}$$

where N is the number of position estimates and A_i represents either the x- or y component. This produces a new coordinate (μ_x, μ_y) acting as a center of mass for the cluster of the position estimates. The euclidean distances from each position estimate to the mean is then calculated using Equation 3.18

$$d_i = \sqrt{(\mu_x - x_i)^2 + (\mu_y - y_i)^2} \tag{3.18}$$

where x_i and y_i are the coordinates of a specific position estimate. The mean distance μ_d represents how the position estimates deviates from the center of the cluster. Since high precision correspond to a compact cluster, the mean distance is a measure of the positioning error. This technique is more formally referred to as *mean absolute deviation* (MAD). To measure how dispersed the distances are, the standard deviation of the distances are calculated as in Equation 3.19

$$S = \sqrt{\frac{1}{N-1}\sum_{i=1}^{N} |d_i - \mu_d|^2}. \tag{3.19}$$

Figure 3.43 exemplifies a uniformly distributed random cluster of position estimates, while Figure 3.44 illustrates the distribution of distances from position estimates to the mean.

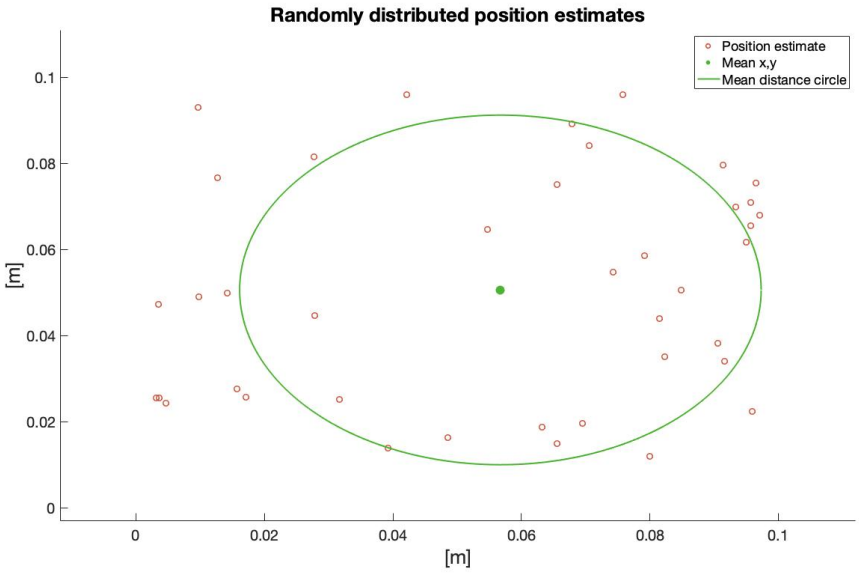

Figure 3.43: Cluster of position estimates with their mean as the green dot. The green circle has a radius equal to the mean distance μ_d. This is an example displaying all estimates within a 1 dm square.

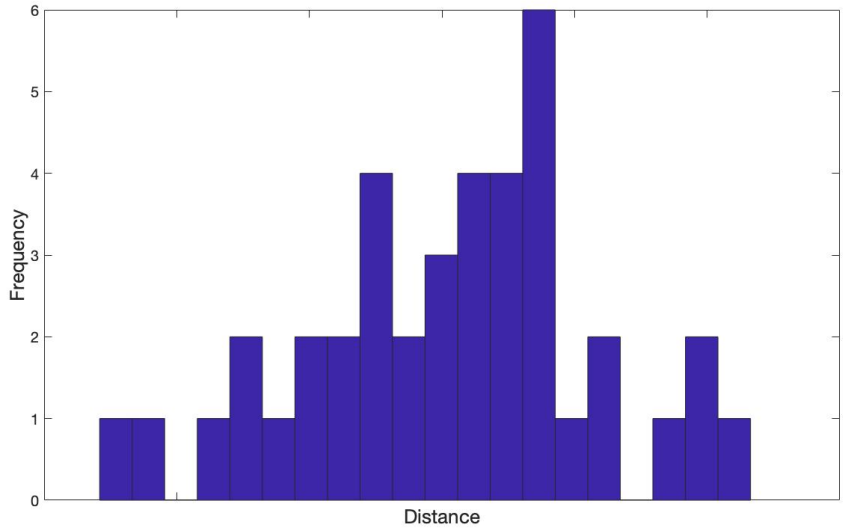

Figure 3.44: Distribution of distances from position estimate to the mean position.

As seen in Figure 3.43, the circle around the mean provides a decent approximation of the size of the cluster. It could be further improved by enforcing a requirement that it should encapsulate 90 % of the position estimates. However, in a real scenario it is far from certain that the cluster will be uniformly distributed, and clusters at different locations could exhibit different distributions. This could lead to issues with the requirement to encapsulate a certain amount of estimates as it would have to include analysis of the distribution as well. Figure 3.44 demonstrates that all distances are not equally probable for this particular example, the standard deviation

of the distance provides a measure of their variation - how cohesive they are, yet provides no indication of how small the cluster is.

These two measures, the MAD (error) and the distance deviation, are both sensitive to outliers. The MAD could significantly increase due to a few outliers, using the median would be more robust in this case. The distance deviation could be used to indicate a more spread out cluster if some position estimates are very close to the mean while some far. However, both measures are best applied in conjunction with the number of position estimates - more estimates will likely reduce effect of outliers and chance effects.

The results in Chapter 4 uses all these measurements together with visual inspection of test results to draw conclusions regarding precision.

4

Results

The chapter presents the results from each measurement performed, divided in to sections describing the hardware setup for the particular measurement. The results consists of the position estimates received after completion of the tests described in Sections 3.4.1.1 and 3.4.1.2. These position estimates are presented graphically without any processing. Appendix B should be read in conjunction with this chapter as it contains tables depicting the *mean x,y coordinates*, *distance error*, *distance deviation* and *number of position estimates* for each *location*. It is recommended that the reader reviews Section 3.4.2 to follow the discussion surrounding the results. The tables in Appendix B are also commented on in this chapter and interesting features are emphasized and displayed here as well. In general, interesting deviations and features are commented on, while more extensive discussion is left to Chapter 5.

4.1 Reference Test Setup

The reference test utilizes the same components for all boards as follows:

- **Oscillator:** TXC Corporation 8Z-38.400MAAJ-T
- **Antenna:** Decawave WB002

Figure 4.1 displays the measurements performed in the LOS environment.

The range bias is evident in Figure 4.1 as the clusters of position estimates tend to be tighter spaced towards the middle and looser at the borders. However, the clusters are generally small indicating that the anchors estimates approximately the same position every time. The **mean error** is **0.034 m** and the **mean number of position estimates** is **37.55**. Table 4.1 illustrates a departure from the otherwise low error at location 12, also clearly visible in Figure 4.1.

Location 32, the location closest to the geometrical centre of the test setup, has a very low error along with excellent accuracy - matching its location (1.8,0.0) with millimeter accuracy. The statistics for this location are presented in Table 4.2.

Figure 4.2 displays the measurements performed in the NLOS environment.

The measurements in the NLOS environment are notable for their lack of position estimates, never reaching above 20 estimates with a **mean number of position estimates** of **7.76**. Figure 4.2 depicts fairly small clusters leading to a relatively low

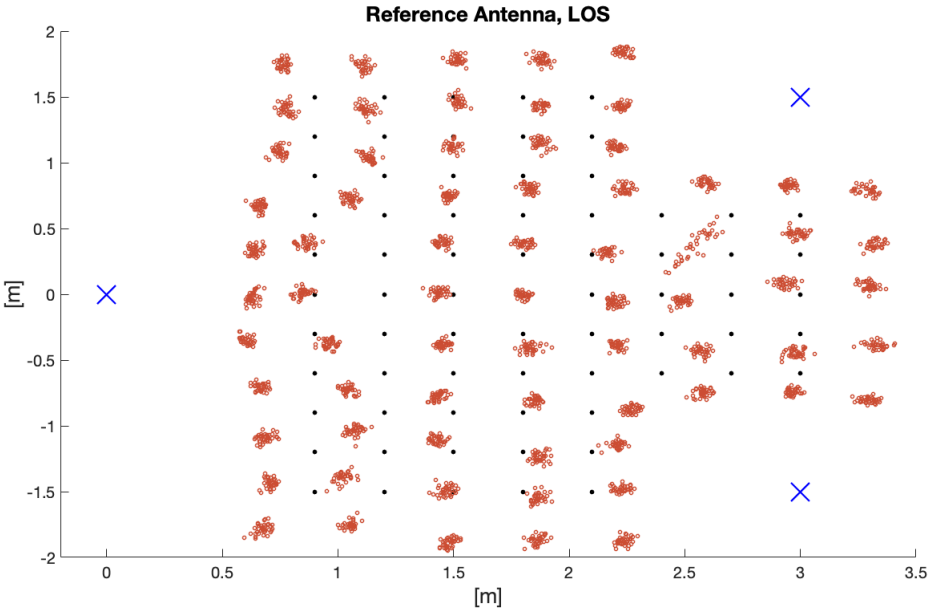

Figure 4.1: Line of sight test regarding the reference setup. Blue crosses are positions for the three anchors, black dots are the predicted values and red dots are the measured values. Figure 3.37 and 3.35 shows the setup of the test.

Table 4.1: Selected values around location 12 in the LOS measurement for the reference antenna. Note that all values, except location and number of measurements, are in meters.

Location	Mean X	Mean Y	Error	Deviation	# of measurements
10	2.95	0.83	0.026	0.013	39
11	2.59	0.84	0.033	0.015	38
12	2.55	0.37	0.11	0.060	38
13	2.49	-0.053	0.029	0.017	38
14	2.57	-0.43	0.032	0.019	38

Table 4.2: Selected values around line 32 in the LOS measurements for the reference antenna. Note that all values, except location and number of measurements, are in meters.

Location	Mean X	Mean Y	Error	Deviation	# of measurements
30	1.83	0.80	0.034	0.016	37
31	1.81	0.38	0.030	0.014	37
32	1.80	-0.0072	0.025	0.012	38
33	1.83	-0.41	0.037	0.020	38
34	1.85	-0.81	0.029	0.014	37

mean error of **0.046 m**. However, this value comes with plenty of uncertainty due

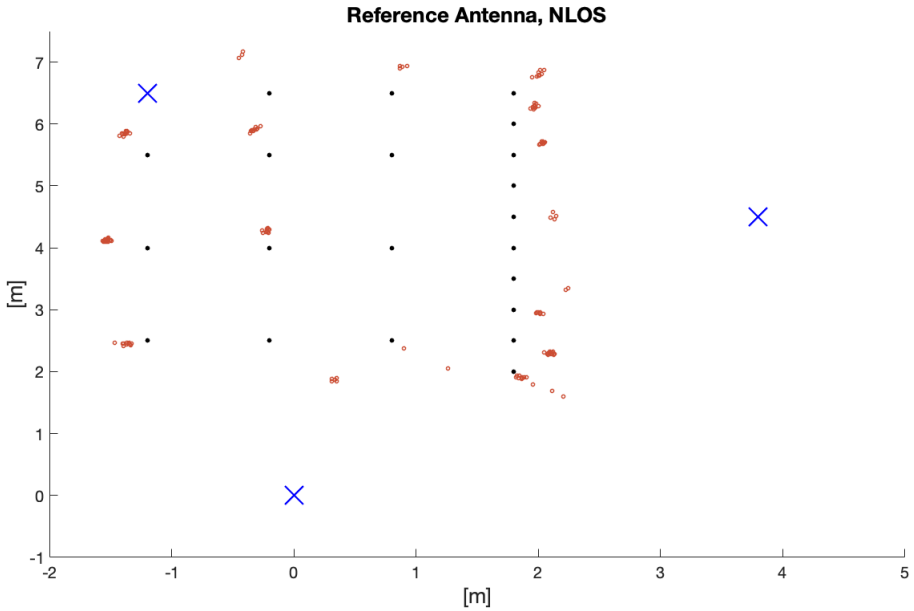

Figure 4.2: Non line of sight test regarding the reference setup. Blue crosses are positions of the anchors, black dots are the predicted values and red dots are measured values. For detailed visualization of the setup and environment see figure 3.36 and 3.39.

to the low number of position estimates. For locations 1-10 (rightmost locations), the position estimates imply an angle leaning outwards from anchor 2 (rightmost anchor) dependent on their y-position. Locations 11-14, which are under the desk area, prove to be very difficult yielding almost no position estimates.

4.2 Octagonal Antenna Test Setup

The octagonal antenna test utilizes the same components for all anchors as follows:

- **Oscillator:** TXC Corporation 8Z-38.400MAAJ-T
- **Antenna:** Octagonal band-reject

The tag uses the Decawave WB002 antenna.

Figure 4.3 displays the measurements performed in the LOS environment.

The range bias is again visible in the measurements with the octagonal antenna, yet not showcasing as clear patterns as for the reference antenna. The clusters are generally small as suggested by a **mean error** of **0.036 m**. Acquiring position estimates proved to be no issue as indicated by a **mean number of position estimates** of **37.64**. As for the reference antenna, location 32 demonstrates below average error and millimeter accuracy. Table 4.3 displays the statistics for location 38 (bottom, third column) and its surroundings. The cluster, or clusters seen around location 38 hints that the position was difficult to estimate - ”hopping around” before

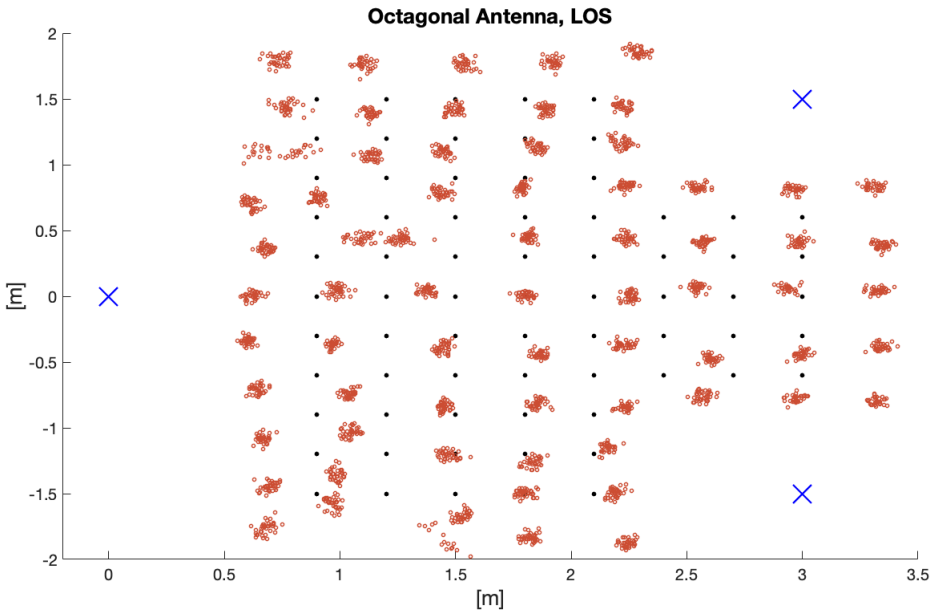

Figure 4.3: Line of sight test with the Octagonal antenna. Blue crosses are positions for the three anchors, black dots are the predicted values and red dots are the measured values. Figure 3.37 and 3.35 shows the setup of the test.

settling on a narrower estimation. This creates a large distance deviation meaning that the distance from position estimate to the mean has a significant variation.

Table 4.3: Selected measurements from location 36 to 40 for the Octagonal antenna in LOS test. Note that all values, except location and number of measurements, are in meters.

Location	Mean X	Mean Y	Error	Deviation	# of measurements
36	1.80	-1.50	0.032	0.016	39
37	1.82	-1.84	0.033	0.018	38
38	1.52	-1.97	0.12	0.066	37
39	1.53	-1.67	0.036	0.018	37
40	1.47	-1.21	0.038	0.019	38

Location 68, specified in Table 4.4, is another anomaly with a pattern stretched in the x-direction giving rise to both large error and deviation.

Table 4.4: Selected measurements from location 66 to 70 for the octagonal antenna in LOS test. Note that all values, except location and number of measurements, are in meters.

Location	Mean X	Mean Y	Error	Deviation	# of measurements
66	0.68	0.36	0.032	0.013	38
67	0.61	0.70	0.040	0.019	37
68	0.77	1.096	0.11	0.079	38
69	0.77	1.44	0.042	0.028	38
70	0.73	1.79	0.044	0.019	38

Figure 4.4 displays the measurements performed in the NLOS environment.

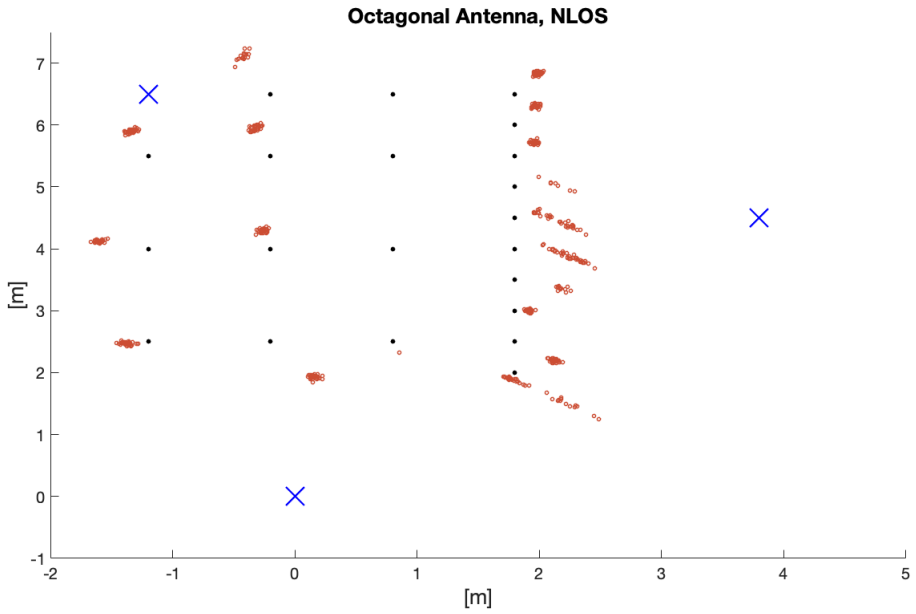

Figure 4.4: The Non-Line of Sight measurement with the Octagonal antenna. Blue crosses are positions of the anchors, black dots are the predicted values and red dots are measured values. For detailed visualization of the setup and environment see figure 3.36 and 3.39.

Comparing the octagonal- to the reference antenna in the NLOS environment, there is a significant difference in the ease of obtaining position estimates. The **mean number of position estimates** is **25.14** and the **mean error** is **0.073 m**. While the mean error is higher than for the reference antenna, the number of position estimates lowers the uncertainty making the error more reliable. The angled pattern for locations 1-7 are clearly visible in Figure 4.4, stretched out on a thin angled line. The first five locations are specified in Table 4.5 displaying the high precision achieved for location 2-4 while 1 and 5 prove more difficult.

Table 4.5: Selected measurements from location 1 to 5 for the NLOS test with the Octagonal antenna. Note that all values, except location and number of measurements, are in meters.

Location	Mean X	Mean Y	Error	Deviation	# of measurements
1	1.96	1.73	0.29	0.13	37
2	2.12	2.20	0.033	0.019	37
3	1.92	3.00	0.025	0.011	27
4	2.18	3.36	0.041	0.023	12
5	2.24	3.88	0.13	0.073	36

Table 4.6 begins by showing the lack of position estimates at location 14, this leaves a lot of room for chance yielding an error of 0 m which obviously does not imply perfect precision. When moving to the other side of the desk, at locations 15-18, the clusters are much smaller with plenty of estimations in each. Location 16 stands out with a very small and cohesive cluster, especially considering the difficult NLOS environment. While location 18 has a decent number of estimates, it is plagued by a few outliers causing a large distance deviation along with a large error as well.

Table 4.6: Selected measurements from location 14 to 18 for the NLOS test with Octagonal antenna. Note that all values, except location and number of measurements are in meters.

Location	Mean X	Mean Y	Error	Deviation	# of measurements
14	0.85	2.33	0	0	4
15	0.16	1.93	0.037	0.020	25
16	-0.26	4.29	0.034	0.018	37
17	-0.32	5.95	0.048	0.018	30
18	-0.37	7.25	0.26	0.30	21

4.3 Vivaldi Antenna Test Setup

The vivaldi antenna test utilizes the same components for all anchors as follows:

- **Oscillator:** TXC Corporation 8Z-38.400MAAJ-T
- **Antenna:** Vivaldi high gain

The tag uses the Decawave WB002 antenna.

Figure 4.5 displays the measurements performed in the LOS environment.

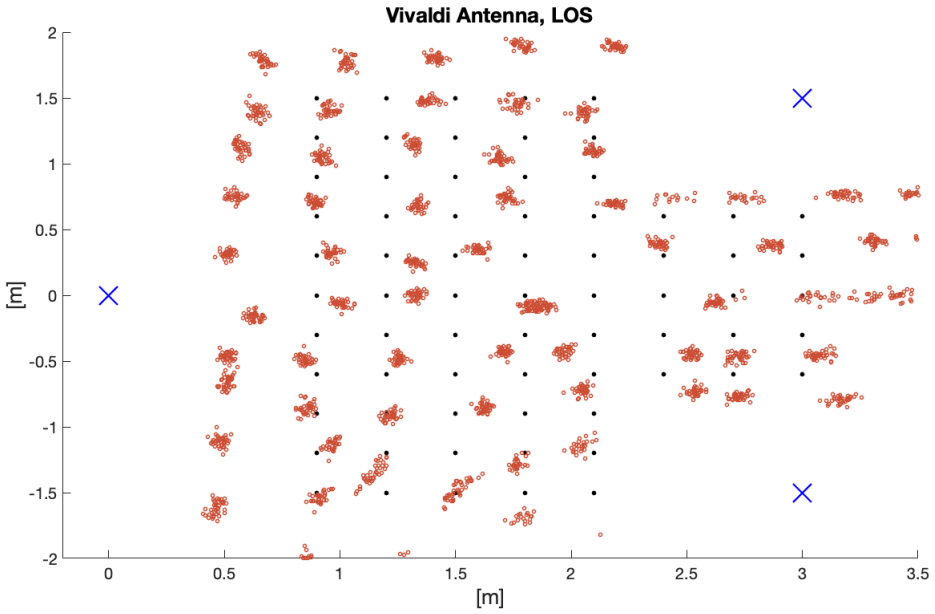

Figure 4.5: Line of sight measurement for the Vivaldi antenna. Blue crosses are positions for the three anchors, black dots are the predicted values and red dots are the measured values. Figure 3.37 and 3.35 shows the setup of the test.

The measurements performed with the vivaldi antenna are more disperse and have a less consistent range bias, when compared to the other antennas. There is an indication of pattern present on the negative side of the y-axis where several clusters are stretched at an angle. Obtaining estimates proved very difficult in some areas, notably around (2.2,0.0) and (1.3,-1.5). The **mean number of position estimates** is slightly lower than for the other antennas at **34.97** and the **mean error** is **0.040 m**, which is somewhat higher. With the level of dispersion for some locations it can be difficult to visually evaluate the precision in Figure 4.5. This is exemplified by location 11, seen in Table 4.7 which is heavily spread out in x-direction producing an error so large that position estimates spread in to neighbouring locations.

Table 4.7: Selected measurements around location 11 for the Vivaldi antenna in LOS setup. Note that all values, except location and number of measurements, are in meters.

Location	Mean X	Mean Y	Error	Deviation	# of measurements
9	3.31	0.41	0.031	0.015	38
10	3.18	0.76	0.037	0.019	37
11	2.63	0.74	0.16	0.076	38
12	2.87	0.38	0.035	0.015	37
13	2.62	-0.055	0.026	0.016	38

Table 4.8 illustrates the nonexistent position estimates at location 39 and only 4 registered at location 38 which imply that there a null present around these locations. A similar case is found around location 16 and 17 where almost no estimates were possible either, while surrounding locations produced well defined clusters with several estimates.

Table 4.8: Selected measurements from location 36 to 40 for the Vivaldi antenna in LOS setup. Note that all values, except location and number of measurements, are in meters.

Location	Mean X	Mean Y	Error	Deviation	# of measurements
36	1.77	-1.28	0.035	0.024	29
37	1.79	-1.69	0.039	0.021	20
38	1.28	-1.96	0.016	0.0051	4
39	NaN	NaN	NaN	NaN	0
40	1.15	-1.35	0.070	0.041	38

Figure 4.6 displays the measurements performed in the NLOS environment.

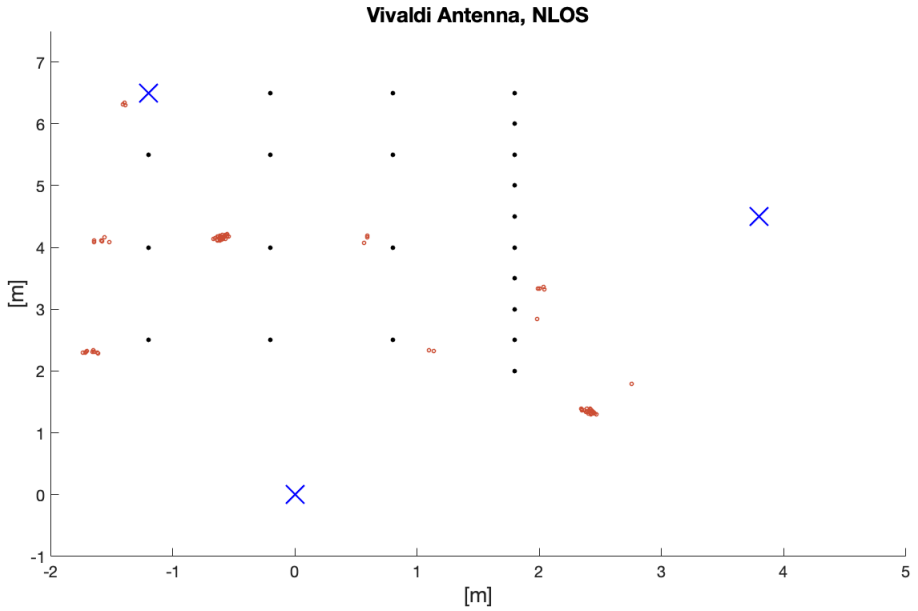

Figure 4.6: The Non Line of Sight measurement for the Vivaldi antenna. Blue crosses are positions of the anchors, black dots are the predicted values and red dots are measured values. For detailed visualization of the setup and environment see figure 3.36 and 3.39.

It is evident from Figure 4.6 that the setup with the vivaldi antenna struggled to a greater extent than the other antennas to obtain estimates in the NLOS environment. The **mean number of position estimates** is only **4.67** and the very uncertain **mean error**, influenced by the low number of estimates, is **0.028 m**. A low value which should not be relied upon.

4.4 10 ppm Oscillator Test Setup

The 10 ppm oscillator test utilizes the same components for all boards as follows:

- **Oscillator:** Kyocera International KC2520C38.4000C1YE00
- **Antenna:** Decawave WB002

Figure 4.7 displays the measurements performed in the LOS environment.

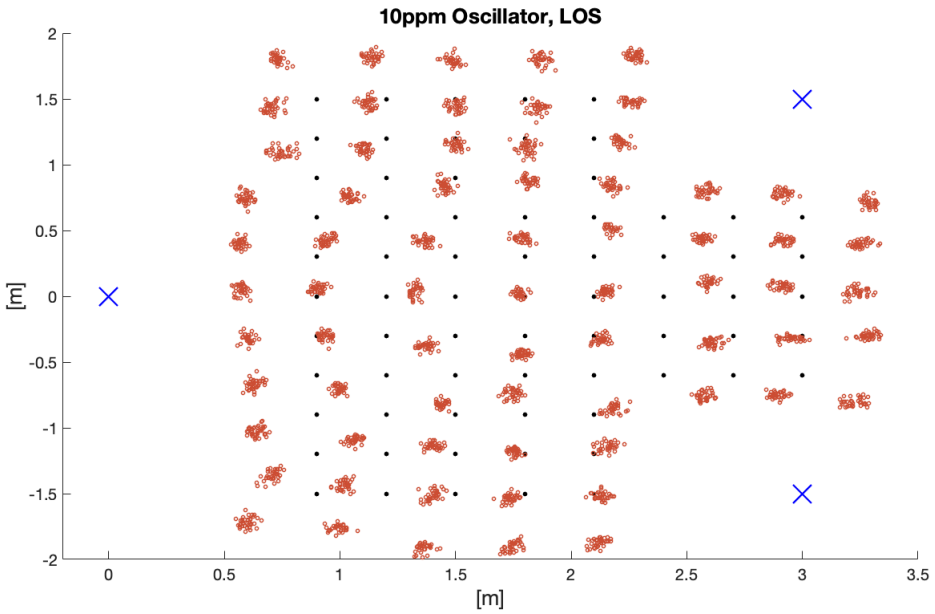

Figure 4.7: Line of sight test for the Kyocera 10 ppm oscillator together with the reference antenna. Blue crosses are positions for the three anchors, black dots are the predicted values and red dots are the measured values. Figure 3.37 and 3.35 shows the setup of the test.

The measurements with the 10 ppm setup in Figure 4.7 is strikingly similar to the reference test setup in Figure 4.1, indicating that the antenna dictates the performance. The **mean error** is **0.034 m** and the **mean number of position estimates** is **36.73**, also very similar to the reference test. The improved precision at location 12 and other smaller variations between the results of the two test setups are likely coincidental.

Figure 4.8 displays the measurements performed in the NLOS environment.

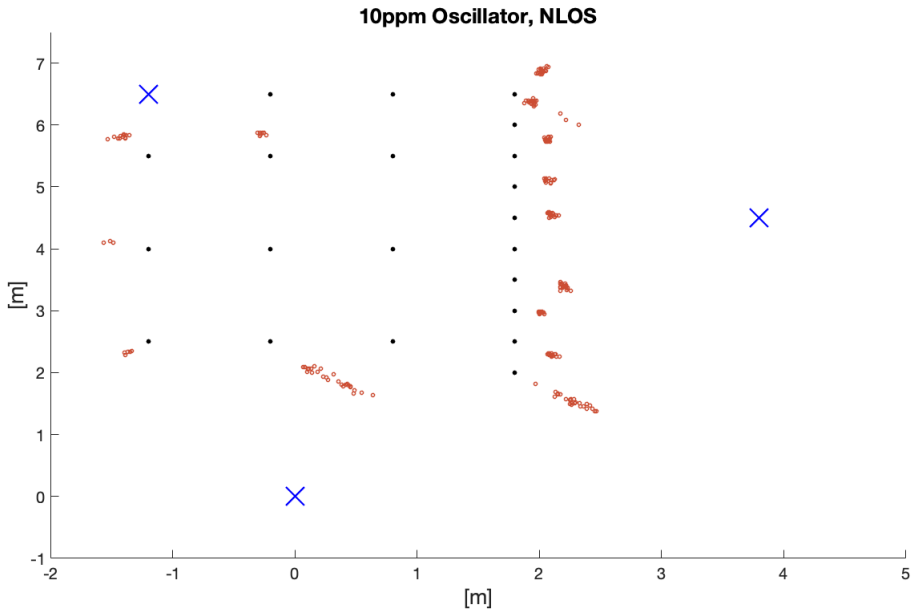

Figure 4.8: Non Line of sight measurement with the Kyocera 10 ppm oscillator and reference antenna. Blue crosses are positions of the anchors, black dots are the predicted values and red dots are measured values. For detailed visualization of the setup and environment see figure 3.36 and 3.39.

The NLOS measurements also bear some similarities to the reference test setup, the main difference being the improved **mean number of position estimates** at **11.19** with the most significant increase at location 15. This makes the **mean error** at **0.055 m** more reliable as well. The angled spread, as previously seen in both the reference- and the octagonal test setup is present here as well. Table 4.9 illustrates another similarity to the reference test setup in that location 5 remains difficult to estimate while its neighbouring locations are estimated with relatively precise clusters.

Table 4.9: Selected measurement data from location 3 to 7 for the Kyocera 10 ppm oscillator. Note that all values, except for location and number of measurements, are in meters.

Location	Mean X	Mean Y	Error	Deviation	# of measurements
3	2.011	2.97	0.015	0.0078	19
4	2.2	3.39	0.036	0.023	21
5	NaN	NaN	NaN	NaN	0
6	2.098	4.55	0.032	0.016	20
7	2.076	5.11	0.032	0.015	14

4.5 2 ppm Oscillator Test Setup

The 2 ppm oscillator test utilizes the same components for all boards as follows:

- **Oscillator:** Taitien Electronics TYKTCCSANF-38.400000
- **Antenna:** Decawave WB002

Figure 4.9 displays the measurements performed in the LOS environment.

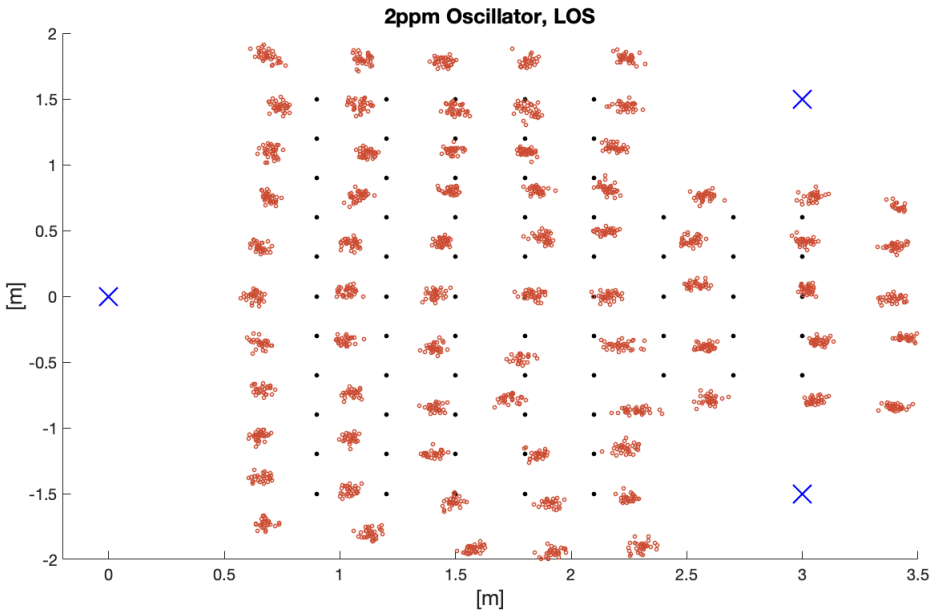

Figure 4.9: The Line of sight measurement with the Taitien 2 ppm oscillator and reference antenna. Blue crosses are positions for the three anchors, black dots are the predicted values and red dots are the measured values. Figure 3.37 and 3.35 shows the setup of the test.

The 2 ppm measurements displayed in Figure 4.9 show mainly small clusters with some slight angled pattern at the bottom of the visible y-axis. Its main difference from the reference- or 10 ppm test setup is the lack of a bulge in the three leftmost columns. The **mean number of position estimates** at **34.19**which is actually the lowest for a LOS measurement. The **mean error** at **0.035 m** is on par with the reference test setup.

Figure 4.10 displays the measurements performed in the NLOS environment.

Comparing the 2 ppm NLOS measurement to the 10 ppm NLOS measurement, they appear similar regarding the where position estimates are obtained. The **mean error** at **0.050** remains at a similar level. However, there is a significant increase in the **mean number of position estimates** at **17.86**. Exemplified by the now estimated location 5 which earlier had no estimations with the reference antenna. Table 4.10 specifies the now estimated location 5 and its neighbours, the precision is uncertain due to the low number of estimations.

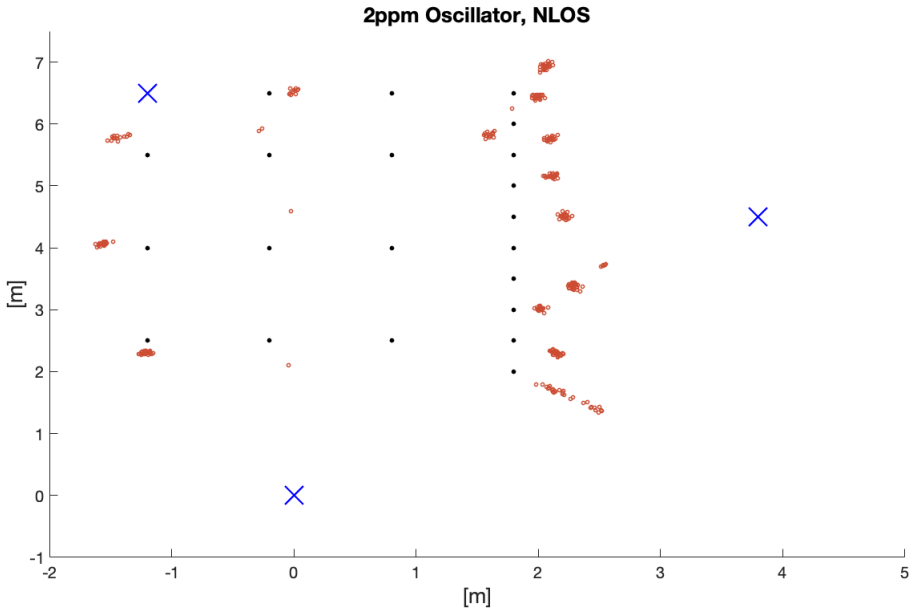

Figure 4.10: Non Line of Sight test for the Taitien 2 ppm oscillator together with the reference antenna. Blue crosses are positions of the anchors, black dots are the predicted values and red dots are measured values. For detailed visualization of the setup and environment see figure 3.36 and 3.39.

Table 4.10: Selected values for the Taitien 2 ppm oscillator in NLOS test. Note that all values, except location and number of measurements, are in meters.

Location	Mean X	Mean Y	Error	Deviation	# of measurement
3	2.015	3.013	0.028	0.018	27
4	2.29	3.38	0.042	0.019	29
5	2.53	3.72	0.016	0.012	6
6	2.21	4.51	0.033	0.023	28
7	2.11	5.16	0.033	0.019	27

4.6 2 ppm Oscillator and Octagonal Antenna Test Setup

The 2 ppm oscillator and octagonal antenna test utilizes the same components for all anchors as follows:

- **Oscillator:** Taitien Electronics TYKTCCSANF-38.400000
- **Antenna:** Octagonal band-reject

The tag uses the Decawave WB002 antenna.

This test was only performed in the NLOS environment. Figure 4.11 displays the measurements performed in the NLOS environment.

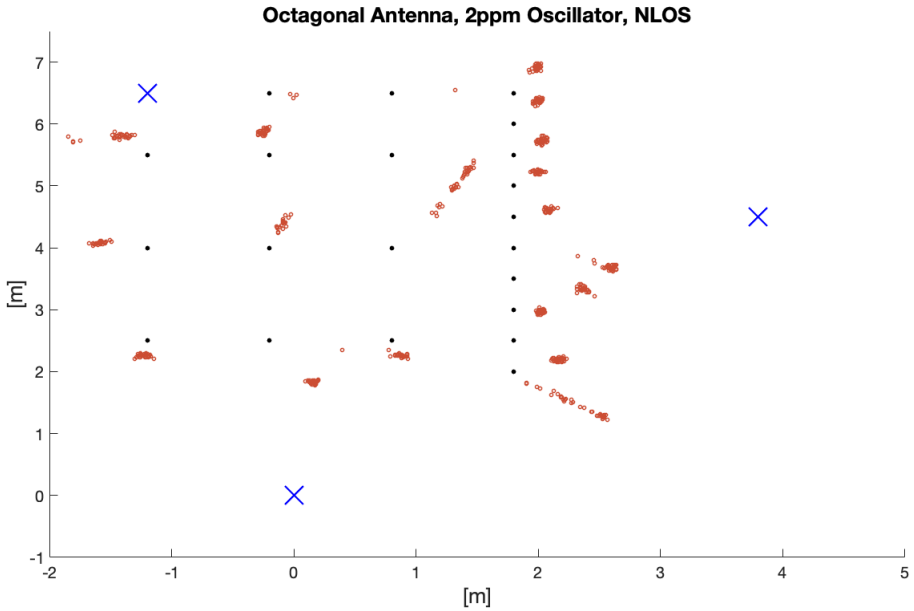

Figure 4.11: Non Line of Sight test with both Taitien 2 ppm oscillator and the Octagonal antenna. Blue crosses are positions of the anchors, black dots are the predicted values and red dots are measured values. For detailed visualization of the setup and environment see figure 3.36 and 3.39.

Combining the top performers in the NLOS environment, the 2 ppm oscillator and the octagonal antenna, yields the highest quality NLOS measurement as well. Due to the difficulty of obtaining position estimates in NLOS, the **mean number of position estimates** at **29.33** stands out as a good quality indicator. The **mean error** at **0.068 m** is higher than most other NLOS measurement, yet more reliable due to high number of position estimates. Table 4.11 illustrates the first proper estimation of location 13, although with a high error and stretched cluster. Together with the estimation of location 14 and 15-18, this is the best performance for the area under the desk.

Table 4.11: Selected measurement data for location 11 to 15 with Taitien 2 ppm oscillator and Octagonal antenna. Note that all values, except location and number of measurements, are in meters.

Location	Mean X	Mean Y	Error	Deviation	# of measurements
11	NaN	NaN	NaN	NaN	0
12	1.32	6.55	0.0012	0	4
13	1.34	5.050	0.22	0.15	37
14	0.87	2.26	0.039	0.027	26
15	0.16	1.84	0.048	0.087	37

5

Discussion & Conclusions

The goal of this project was to investigate the impact certain hardware component have on the precision of a UWB positioning system. Impact is a broad concept and to accurately specify the impact that the antennas and oscillators have on the precision was deemed not possible towards the end of this project. To establish that relation in a statistically reliable manner, four areas of improvement were identified:

- improved knowledge of the performance of evaluated components
- improved methods for switching components
- more extensive testing
- alternative testing methods.

This chapter will discuss these points along with insights gained throughout the project on improved design choices and test setups. Firstly though, a few interesting results will be discussed and how the evaluation procedure and precision measures possesses certain limitations.

5.1 Remarks on Evaluation and Precision

The evaluation process and therefore the precision measures of the system is heavily dependent on mean values as explained in Section 3.4.2. It is well known that the mean of a population is sensitive to outliers, at the same time neglecting outlying position estimates could yield misleading conclusion regarding precision. In Section 4.2 it was pointed out that sometimes the cluster is made of several smaller clusters, this is highlighted by the green rectangle in Figure 5.1. Removing outliers would in this case cause almost half of the estimates to be neglected.

Another interesting type of cluster can be seen in Figure 5.2 where several clusters have a rectangular shape and the two highlighted by the green rectangle both have a very distinct form. A probable reason for this is a consequence of the trilateration method. As indicated in Section 2.2.2 the precision will vary depending on the location due to the DOP, which can result in geometrical biases as the intersecting area stretches in a certain direction. In Section 3.4.2 the concept of using a circle to enclose a majority of the estimates as a precision measure was discussed. Several clusters seen in the results could be approximated by a circle, yet the ones in Figure 5.2 does not pertain to this type of distribution. Analyzing the the distributions

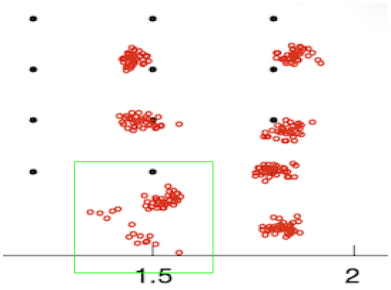

Figure 5.1: Selected position estimates from Figure 4.3, the octagonal test setup in LOS.

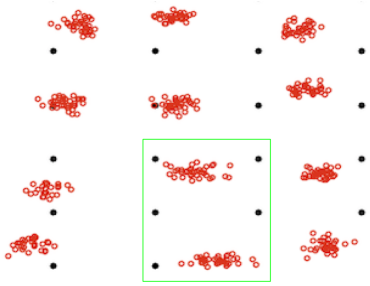

Figure 5.2: Selected position estimates from Figure 4.9, the 2 ppm oscillator test setup in LOS.

of the clusters could assist in acquiring better precision measures and also help understanding the impact of antennas and placement. Figure 5.3 illustrates a gradual shift in distribution within the clusters - from a circular shape to a more rectangular shape. Studying all the clusters gives the perception that there is a gradually steeper slant downwards if looking right to left. Considering that these measurements are performed with the more directive vivaldi antenna, the slant is likely caused by the tag being located on the edge of a lobe/null of at least one antenna. Causing the range in one direction to be over- or underestimated within this area.

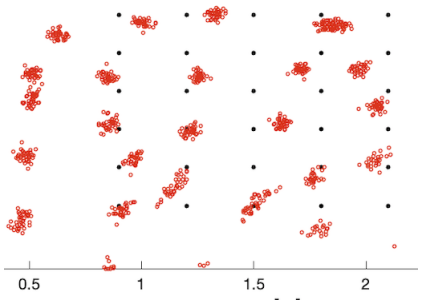

Figure 5.3: Selected position estimates from Figure 4.5, the vivaldi test setup in LOS.

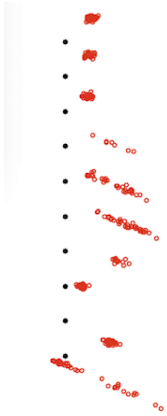

Figure 5.4: Selected position estimates from Figure 4.4, the octagonal test setup in NLOS.

Figure 5.4 presents another type of stretched clusters slanting upwards. These patterns were recurring for several measurements, although they were reduced with improved frequency stability of the oscillator - visible in Figures 4.10 and 4.11.

The level of precision can be difficult to assess, hence the need for more than one metric to evaluate the performance. Yet there is still reason to be sceptical towards the results, primarily due to the limited amount of testing performed. To further the analysis of the contrast between test setups, the distributions of the clusters ought to be examined as this would more clearly indicate the different behaviour of the evaluated components and their affect on overall system.

5.2 Excluded Measurements

Undertaking a broad scope project as this within a limited time frame means that some of the more time consuming tasks needs to be left out. The process of testing, measuring, evaluating, reworking and testing again is a very gradual process, influenced by delayed hardware deliveries and malfunctions. Several interesting investigation were therefore left out. This section will specify calibrations, measurements and tests that could have improved the conclusions with regards to the stated aim. A few intriguing leads that were discovered during the testing process will also be presented.

In Section 2.5.3, several performance metrics to determine the quality of an UWB antenna were presented. The metrics *fidelity factor* and *group delay* describe how the transmitted- or received pulse change as a result of the antenna. Unable to reliably measure these metrics accurately, it remains unknown how the shape of the transmitted pulse behaves. Knowing this could possibly answer the question of why it was so difficult to establish communication at some locations.

Due to unfortunate events during the mounting of the PCBs some of the units were broken. In retrospect it would be wise to order a larger buffer of components to ensure that enough devices could be built. This led to only four working devices in the end and therefore limited the measurement possibilities that could be performed. In order to have a reliable three-dimensional positioning system four anchors would be needed, but only three anchors and one tag could be realized. It was therefore only possible to perform 2-dimensional positioning, and thus the height component is ambiguous and has unknown precision.

Described in section 3.1.1, the PCBs were designed to be modular. However, mounting the oscillators by hand meant that they were destroyed once removed. It is also a time consuming process. This limitation only allowed one test series to be performed with each test setup which, as previously stated, limits the validity of the evaluation.

While there are advantages performing the precision tests in a environment more representing of an applied scenario, a more controlled test environment would allow a better understanding of the impact component changes has to the system. It would remove some of the unknown environmental effects, allowing more controlled testing of multipath and the penetrating ability of the signals. Results such as those discussed in Section 5.1 could be tested further to study how consistently they appear.

Some metrics, while interesting in many applications, were not within the scope of the project. However, they are briefly acknowledged here. Accuracy, described as to what extent a position estimate corresponds to the desired location, in this case the locations as seen in figure 3.35 and 3.36. High precision is a pre-requisite for high accuracy and provides more information regarding the systems reliability and consistency. The drawback of not having accuracy as a part of the measurement is the lack of visualization and intuitive feeling that it brings as one can clearly correlate it with the intended location. However, in order to measure the accuracy with a high certainty, the alternative method for creating the coordinate system

made up by the pre-determined locations has to be of a very high standard both in terms of precision and accuracy. The required steps for a accuracy test are the following:

- Calibrating the system as described in application notes from Decawave
  - Antenna Delay
  - Range Bias
- Construct a test setup specifically design for accuracy measurements using a highly precise alternative positioning method.

As the test was conducted in such a way that the tag was allowed a settling time after it was moved there has been no deeper analysis in how the precision is affected for a moving tag. If the test would reflect a real situation with a tag placed on a movable target, then a test environment would be needed where control of the tag speed and direction of movement could be controlled. A way to execute this sort of test is to place the tag on a slider, with a well defined length and speed control, and do a continuous positioning measurement for different length and speed.

5.3 PCB Improvements

As mentioned, due to the limited time available to complete this project, some revisions were needed. One of this was that the PCB only went through one iteration, which meant that some issues that were discovered during the project could not be corrected. The RF transmission line, which is one of the more crucial parts of the PCB, was unfortunately deformed during the manufacturing process and is one of the things that could not be fixed. The RF transmission line should initially look like the one presented in figure 5.5 but instead became like figure 5.6, also seen in figure 3.34.

The purpose of designing the RF transmission line as in figure 5.5 is to minimize reflections and losses for the highly sensitive RF signal. By making the RF transmission line as a wide solid trace from the SMA to the Balun one minimizes the problems which rises from sharp edges and the variation in impedance, as described in section 3.1.2. The transmission line seen in figure 5.6 will instead act as a *stepped-impedance filter*, which means that it will implement stop-band and pass-band characteristics [18]. Figure 5.7 shows the simulated scattering parameter S_{11} for the intended RF transmission line in figure 5.5, measured at the SMA. The markers *m1* and *m2* in this figure indicates the frequency band, with a centre frequency of 4 GHz, for which this positioning system is intended to be used. One can clearly see that, for the whole bandwidth, not a single point is higher than -32 dB, meaning that the reflections are quite low.

Figure 5.8 show the simulated frequency response for the RF transmission line which was instead manufactured. What is clearly seen in this figure is that the reflection, from the SMA, is significantly worse than in the ideal case above. The lowest S_{11} is around -27 dB at approximately 4 GHz, and -17.665 dB at the worst part of the

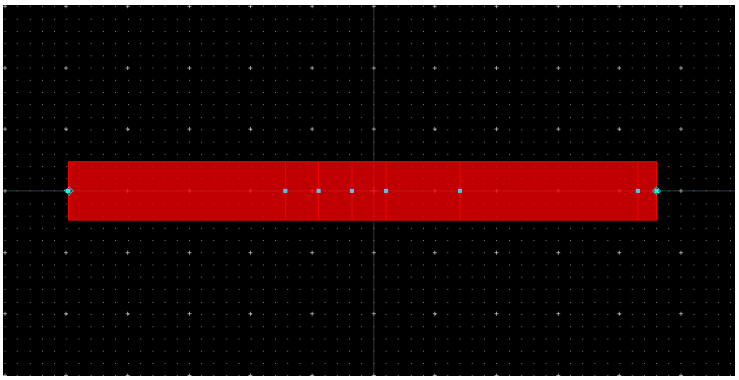

Figure 5.5: Intended design of the RF transmission line depicted in Keysights *Advance Design System*

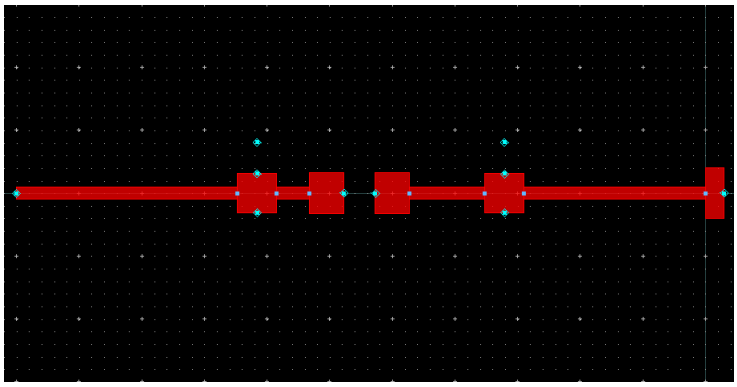

Figure 5.6: The realized transmission line depicted in Keysights *Advance Design System*

designated frequency band.

However, the impact of this mismatch on the system is unknown, but due to the sensitive nature of this positioning system, working with very low signal strength (-41.3 dBm), it is highly likely that this loss will degrade the precision of this positioning system. In order to ensure the actual impact, further tests would have to be made.

Additional contributing causes that may affect the signal integrity is the dielectric material, which was described in 3.1.2. The FR-4 TG130, used by the chosen manufacturer of the PCB, has a dielectric constant of 4.2 - 4.7 [32]. This variation leads to an uncertainty of the RF transmission line impedance and might therefore affect the signal in a negative way. A solution to this problem could instead be to use another substrate, such as Rogers RO4000 LoPro Series which is a high frequency circuit material [33]. This substrate has much less variation in the dielectric constant which would contribute to more reliable measurements.

The PCB was designed with the intention of being modular, which lead to the spread of most components. Oscillators and decoupling capacitors are designed to be as near to the IC to which it belongs to ensure that it works as intended, but some of these requirements had to be neglected. The impact that this might have on the system is difficult to say, probably quite small, but should still be taken into

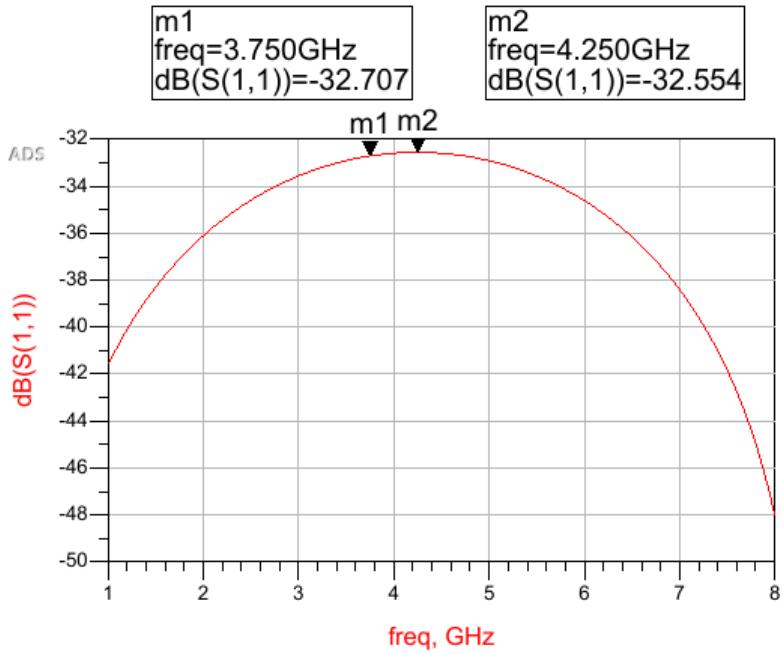

Figure 5.7: Simulated S_{11} parameter for the intended RF trace.

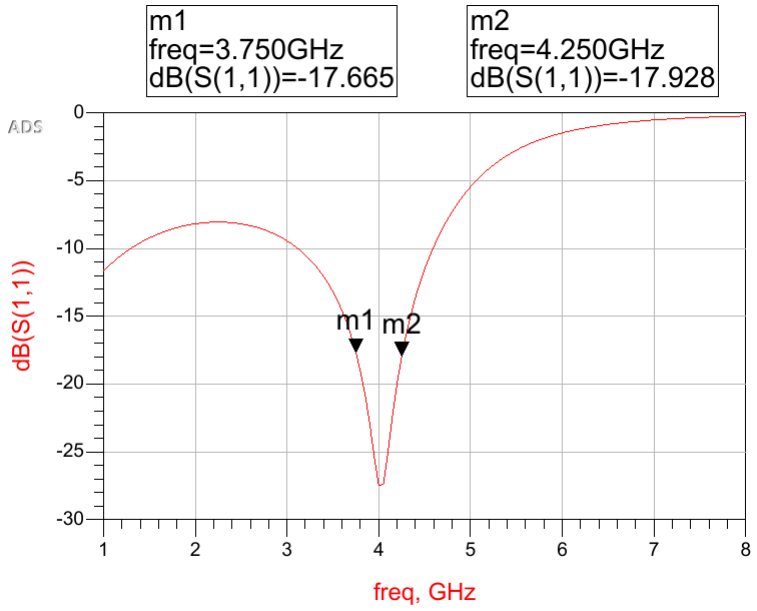

Figure 5.8: Simulated S_{11} for the stepped-impedance filter that was realized along with the intended components that were mounted in the pi-network.

consideration. A more likely negative impact on the precision is how the oscillators were mounted. As described in section 3.1.2 all oscillators is of the type SMD. The first oscillator was attached by solder paste and then heated in the oven. This gives a good control over the heat, which is important as oscillators are relative heat

sensitive. The other oscillators used were instead attached by means of a soldering iron, because peripheral components attached to the PCB would melt if the PCB was to undergo a second oven heating. This way of mounting gives little control over the heat supplied, and how this effect the heat-sensitive oscillators is difficult to determine. This could be solved by having several PCBs and sets of components in order to mount the different oscillators on separate PCBs and have a controlled heating cycle using the oven.

To summarize, this chapter can be read as a series of recommendations for anyone with an interest of improving precision of a UWB positioning system. During the course of the project this study has evolved in to a comprehensive review of several subjects closely related to UWB communication, wireless positioning and test- and measurement techniques. Hopefully this information will prove useful to future studies within these subjects.

Bibliography

[1] Decawave Limited, "DW1000 Radio IC,", URL: https://www.decawave.com/product/dw1000-radio-ic/

[2] G. Trudgen, "Phase noise / jitter in crystal oscillators," RAKON UK Ltd, 2009, URL: https://www.rakon.com/products/technical-resources/tech-docs/download/file?fid=54.313

[3] W.G. Rees, "Physical Principles of Remote Sensing," Third ed. UK, Cambridge University Press, 2012, ISBN: 978-0-521-18116-7

[4] D.K. Cheng, "Field and Wave Electromagnetics," Second ed. USA, Addison-Wesley Publ. Company Inc, 1989, ISBN: 0-201-52820-7

[5] Wikimedia Commons, "Interference of two waves.svg," URL: https://commons.wikimedia.org/wiki/File:Interference_of_two_waves.svg

[6] G. Vasilescu, "Electronic Noise and Interfering Signals : Principles and Applications," Berlin, Springer, 2005, ISBN: 9783540407416

[7] R. B. Langley, "Dilution of Precision," GPS World, 1999, URL: http://gauss.gge.unb.ca/papers.pdf/gpsworld.may99.pdf

[8] C. A. Balanis, "Antenna Theory: Analysis and Design," Fourth ed. NJ, USA, Wiley, 2016, ISBN: 978-1-118-64206-1

[9] P-S. Kildal, "Foundations of Antenna Engineering: An Unified Approach for Line-Of-Sight and Multipath," Gothenburg, Sweden, Kildal Antenn AB, 2015, ISBN: 978-91-637-8515-3

[10] G. Quintero, J.-F. Zürcher, A. K. Skrivervik, "System Fidelity Factor: A New Method for Comparing UWB Antennas", IEEE Trans. on Antennas and Propagation, Vol. 59, no. 7, pp. 2502-2512, 2011

[11] C. Roblin, S. Bories, A. Sibille, "Characterization Tools of Antennas in the Time Domain", in 2003 Int. Workshop: Ultra Wideband Systems (IWUWBS), June 2003.

[12] H. Liu, M. Sato, "Determination of the phase center position and delay of a Vivaldi antenna," IEICE Electronics Express, Vol.10, No.21, 1–7, Oct. 2013, DOI: 10.1587/elex.10.20130573

[13] J. Fridén, G. Kristensson, "Calculation of antenna radiation center using angular momentum," In 7th European Conference on Antennas and Propagation (EuCAP), 2013 (pp. 1531-1535). IEEE

[14] D. Dardari, A. Conti, U. Ferner, A. Giorgetti, M. Z. Win, “Ranging With Ultrawide Bandwidth Signals in Multipath Environments,” Proc. IEEE, vol. 97, no. 2, pp. 405-421, Feb. 2009, doi: 10.1109/JPROC.2008.2008846.

[15] D.Neirynck, E. Luk, M. McLaughlin, “An Alternative Double-Sided Two-Way Ranging Method,” 13th Workshop WPNC, Oct. 2016, doi: 10.1109/W-PNC.2016.7822844.

[16] P. Horowitz, W. Hill, “The Art of Electronics,” Third ed. New York, Country: USA, 2015, ISBN: 978-0-521-80926-9.

[17] Patrick Dale R, Fardo Stephen W, “Electricity and Electronics Fundamentals,” Second ed. Lilburn, Country: USA, 2008, ISBN: 0-88173-601-5.

[18] D. M. Pozar, "Microwave Engineering," Fourth ed. Wiley, Country: USA, Nov. 2011, ISBN: 978-0-470-63155-3

[19] Burkhard Vogel, “The Sound of Silence,” Second ed. 70180 Stuttgart, Country: Germany, 2011, ISBN: 9783642197741.

[20] Roy Hejhall, Application note: “Understanding Transistor Response Parameters,” ; Phoenix, Arizona, Country: USA, 1993, Available: https://www.nxp.com/docs/en/application-note/AN139A.pdf

[21] R M. Cerda, “Understaning Quartz Crystals and Oscillators,”. Boston, Country: USA, 2014, ISBN: 9781608071180.

[22] Poisel Richard A, "Electronic Warfare Receivers and Receiving Systems,". Artech House, Country: USA, Nov. 2018, ISBN: 13: 978-1-60807-841-7

[23] K. Mitzner, B. Doe, A. Akulin, A. Suponin, D. Müller, “Complete PCB Design Using OrCAD Capture and PCB Editor,” Second ed, London Country: United Kingdom, 2019, ISBN: 9780128176849. 9780128176856.

[24] N. Sharma, S. S. Bhatia, V. Sharma, J. S. Sivia, "An Octagonal Shaped Monopole Antenna for UWB Applications with Band Notch Characteristics," Wireless Personal Communications, Springer science, Nov. 2019, https://doi.org/10.1007/s11277-019-06968-w

[25] R. Cicchetti, E. Miozzi, O. Testa, "Wideband and UWB Antennas for Wireless Applications: A Comprehensive Review," Dep. of Information Eng., Electronics and Telecom., University of Rome “La Sapienza”, Feb. 2017, http://downloads.hindawi.com/journals/ijap/2017/2390808.pdf

[26] K. Kumar, Er. S. Kaur., "Investigation on Octagonal Microstrip Antenna for RADAR & Space-Craft applications," Int. Journal of Scientific & Engineering Research, Volume 2, Issue 11, November-2011 1, https://www.ijser.org/paper/Investigation-on-Octagonal-Microstrip-Antenna-for-RADAR-Space-Craft-applications.html

[27] M. Durán-Sindreu, J. Naqui, F. Paredes, J. Bonache, F. Martín, "Electrically Small Resonators for Planar Metamaterial, Microwave Circuit and Antenna Design: A Comparative Analysis," Dep. of Electronic Eng., Universitat Autònoma de Barcelona, April 2012, doi: 10.3390/app2020375

[28] G. K. Pandey, M. K. Meshram, "A Printed High Gain UWB Vivaldi Antenna Design Using Tapered Corrugation and Grating Elements," , Wiley Periodicals, Inc., Dep. of Electronics Engineering, Indian Institute of Technology, Feb. 2015,

[29] Das Sushrut, "Microwave Engineering". New Delhi 110001, Country: India, 2015, ISBN: 978-1-68015-877-9.

[30] Bowick Christopher, Blyler John, Ajluni Cheryl, "RF Circuit Design," Second ed, Country: USA, 2010, ISBN: 978-0-08-055342-9, 978-0-7506-8518-4.

[31] Steer Michael B, "Microwave and RF Design - A System Approach," Country: USA, 2011, ISBN: 9781891121883.

[32] Seeed Technology Co.,Ltd., URL: https://www.seeedstudio.com/

[33] RO4000 LoPro Series, Data Sheet, Rogers Corporation., Chandler, Arizona, USA, Publication #92-141, URL: https://rogerscorp.com/-/media/project/rogerscorp/documents/advanced-connectivity-solutions/english/data-sheets/ro4000-lopro-laminates.pdf

A

A.1 Schematics

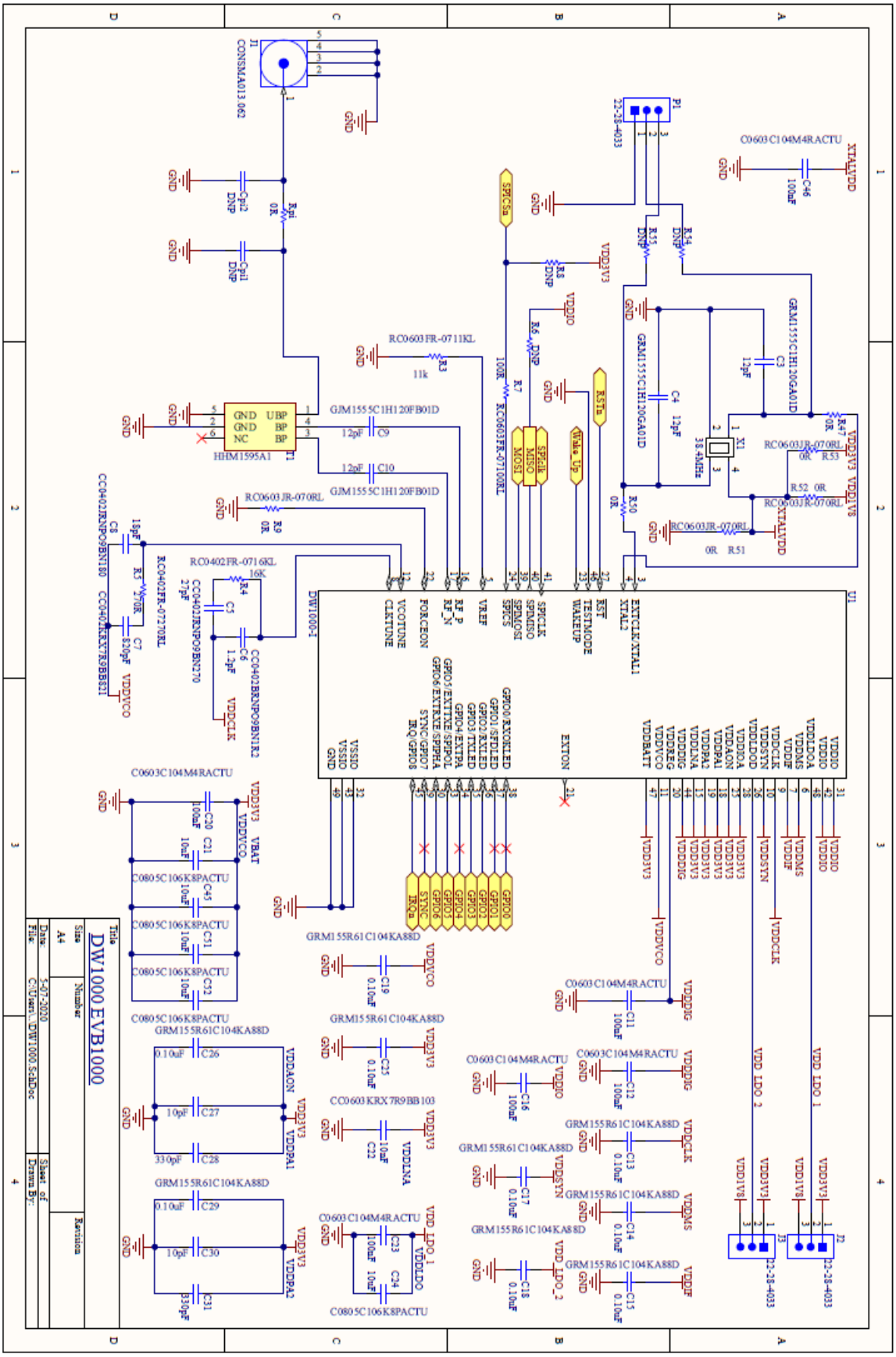

Figure A.1: Schematic regarding DW1000.

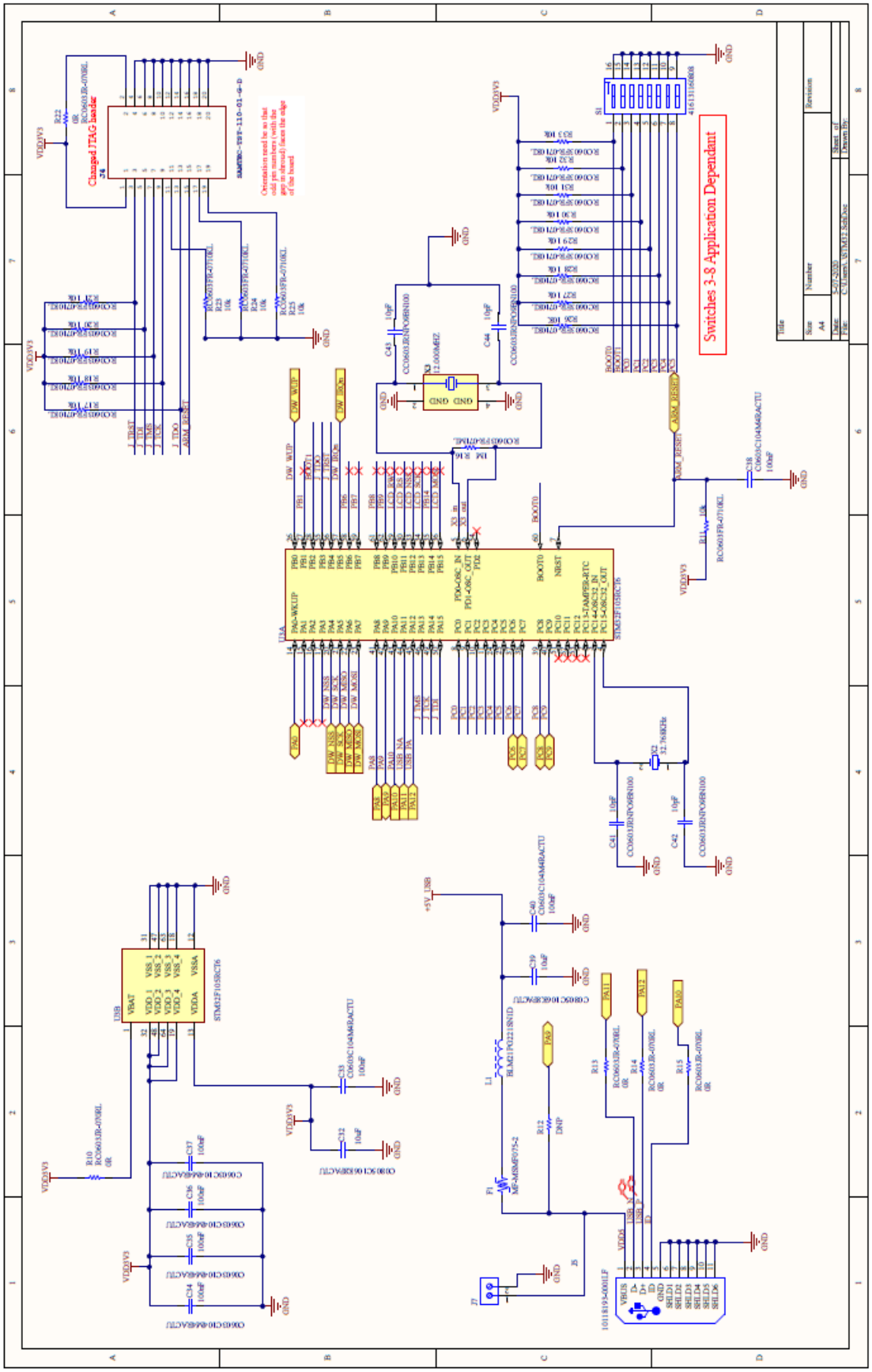

Figure A.2: Schematic regarding STM32.

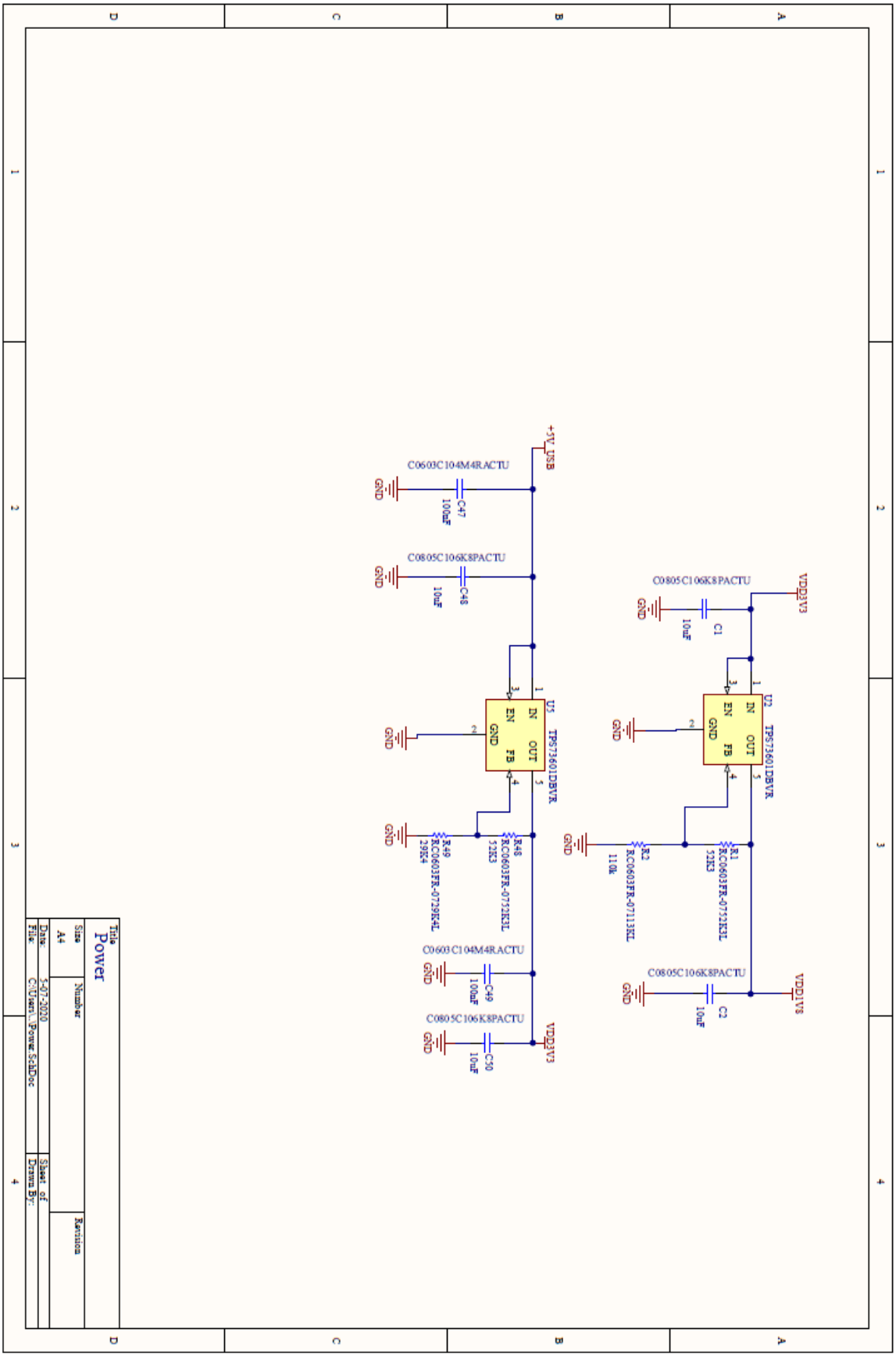

Figure A.3: Schematic regarding power.

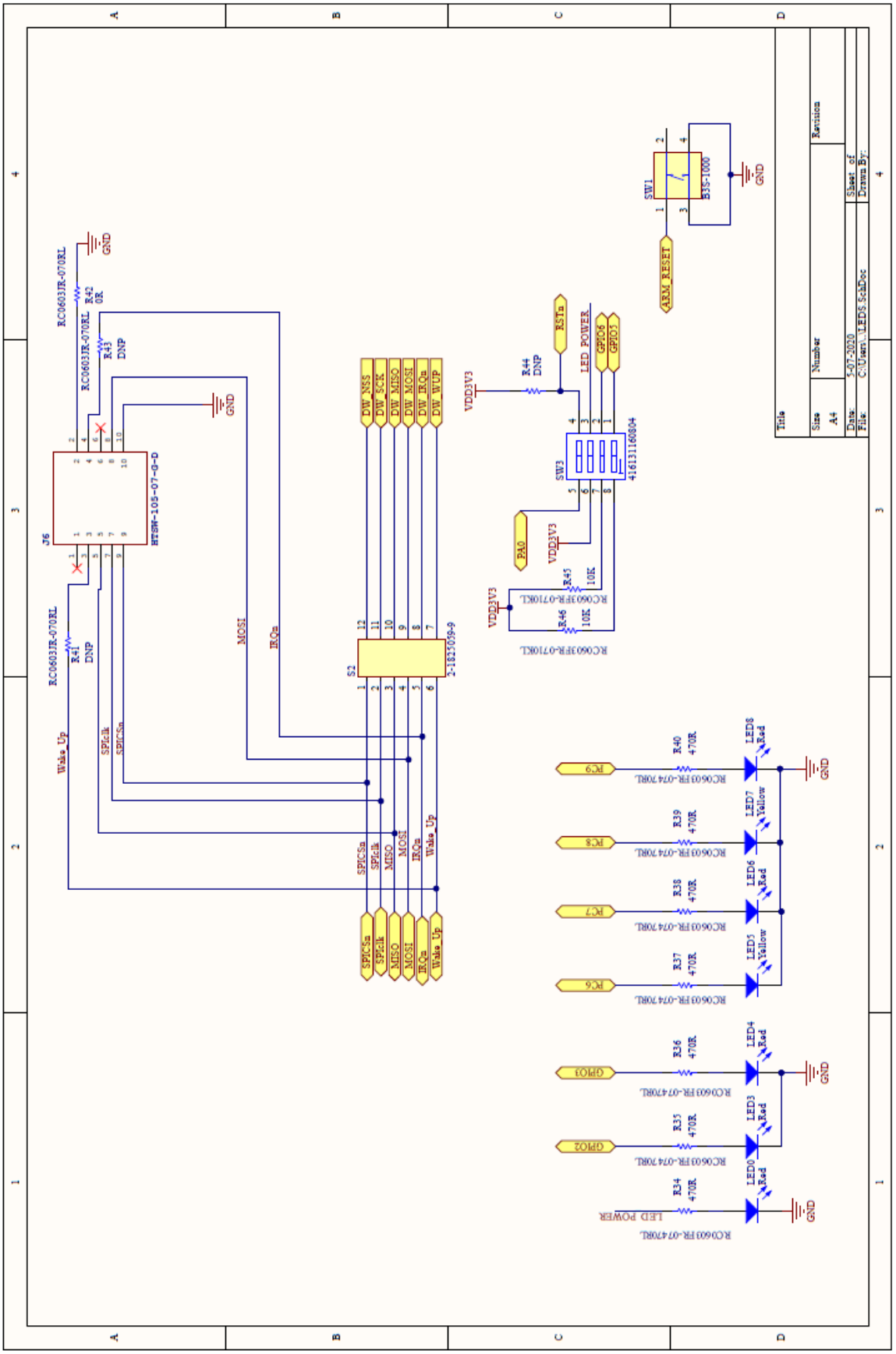

Figure A.4: Schematic regarding LEDs.

B

B.1 Measurement Results for the Reference Antenna

Table B.1: The entire measurement data for the reference antenna in the LOS setup . All values, except location and number of measurements, are in meters.

Location	Mean X	Mean Y	Error	Deviation	# of measurements
1	3.2882	0.78877	0.042535	0.01774	35
2	3.3212	0.37488	0.034805	0.016167	38
3	3.2976	0.063113	0.034219	0.019404	37
4	3.3282	-0.38697	0.036272	0.021234	37
5	3.2958	-0.80444	0.032543	0.01563	38
6	2.9651	-0.74345	0.02695	0.012686	38
7	2.9782	-0.44513	0.038122	0.018612	38
8	2.9325	0.081362	0.03703	0.017284	37
9	2.9863	0.46032	0.03541	0.017478	38
10	2.9483	0.82732	0.026128	0.013338	39
11	2.5933	0.84474	0.032942	0.014851	38
12	2.5458	0.37105	0.11117	0.060033	38
13	2.4864	-0.053179	0.028713	0.017414	38
14	2.5698	-0.43204	0.032419	0.018788	38
15	2.5783	-0.7489	0.032896	0.017657	38
16	2.2379	-1.8747	0.033251	0.016769	38
17	2.2282	-1.4796	0.031991	0.01392	38
18	2.2066	-1.143	0.02802	0.019149	38
19	2.2693	-0.87667	0.032733	0.012189	37
20	2.2066	-0.38834	0.027761	0.015267	38
21	2.1994	-0.058987	0.033494	0.01503	38
22	2.1635	0.31814	0.02841	0.016037	36
23	2.2387	0.80052	0.033653	0.016173	39
24	2.2018	1.12	0.027514	0.012979	38
25	2.226	1.4303	0.026568	0.013806	37
26	2.2337	1.8409	0.033044	0.014173	37

Table B.1: The entire measurement data for the reference antenna in the LOS setup . All values, except location and number of measurements, are in meters.

Location	Mean X	Mean Y	Error	Deviation	# of measurements
27	1.8813	1.7829	0.034437	0.019198	39
28	1.8792	1.4318	0.028565	0.011855	37
29	1.8779	1.1471	0.037588	0.020769	37
30	1.8281	0.80324	0.03401	0.015962	37
31	1.8052	0.38498	0.030448	0.01374	37
32	1.8018	-0.0072164	0.02475	0.012458	38
33	1.832	-0.4074	0.03657	0.019715	38
34	1.8513	-0.81088	0.029029	0.014308	37
35	1.8718	-1.2395	0.035682	0.019043	38
36	1.8652	-1.5474	0.034288	0.020274	38
37	1.8642	-1.8688	0.035475	0.01802	38
38	1.4828	-1.8872	0.036121	0.014307	38
39	1.4675	-1.4919	0.03816	0.019154	38
40	1.4298	-1.1083	0.031648	0.012327	38
41	1.431	-0.77872	0.030502	0.015467	39
42	1.4538	-0.38015	0.028118	0.012984	38
43	1.4354	0.011886	0.031006	0.016603	38
44	1.4496	0.39088	0.030809	0.013129	37
45	1.4791	0.74879	0.024403	0.01507	38
46	1.4959	1.1237	0.031135	0.01805	37
47	1.5198	1.4622	0.031844	0.020117	36
48	1.5154	1.782	0.030604	0.017091	38
49	1.1076	1.7382	0.039518	0.018066	37
50	1.1207	1.4083	0.034052	0.02313	39
51	1.1334	1.0395	0.033537	0.018264	36
52	1.0513	0.72493	0.035629	0.016618	37
53	0.86179	0.38901	0.039371	0.01492	37
54	0.84626	0.009344	0.033288	0.017821	37
55	0.96109	-0.37639	0.034747	0.015531	38
56	1.0423	-0.72742	0.029666	0.017158	38
57	1.0739	-1.0386	0.0364	0.021247	37
58	1.0215	-1.3925	0.03741	0.026404	38
59	1.0535	-1.7522	0.027395	0.019829	37
60	0.67444	-1.7838	0.038961	0.023911	37
61	0.70662	-1.436	0.03669	0.018992	37
62	0.68544	-1.0927	0.035571	0.019103	37
63	0.66638	-0.70738	0.030755	0.01258	37
64	0.60491	-0.35084	0.029384	0.015686	37
65	0.6308	-0.025546	0.038043	0.022759	38
66	0.6397	0.33369	0.033107	0.016649	37
67	0.66	0.66805	0.032499	0.017844	38
68	0.74744	1.0814	0.034795	0.020486	38

Table B.1: The entire measurement data for the reference antenna in the LOS setup . All values, except location and number of measurements, are in meters.

Location	Mean X	Mean Y	Error	Deviation	# of measurements
69	0.77614	1.4089	0.040078	0.02095	39
70	0.76376	1.7488	0.03484	0.015442	37
Mean	**-**	**-**	**0.0341**	**-**	**37.5857**

Table B.2: Complete measurement data for the reference antenna in the NLOS test. Note that all values, except location and number of measurements, are in meters.

Location	Mean X	Mean Y	Error	Deviation	# of measurements
1	1.911	1.8582	0.11457	0.10109	13
2	2.1003	2.2952	0.022111	0.013215	16
3	2.0027	2.9469	0.016889	0.011302	10
4	2.2325	3.3382	0.016998	2.0364e-16	4
5	NaN	NaN	NaN	NaN	0
6	2.1254	4.5107	0.04017	0.017876	4
7	NaN	NaN	NaN	NaN	0
8	2.0319	5.6958	0.019729	0.0075881	10
9	1.9683	6.2811	0.030779	0.017811	11
10	2.0054	6.8068	0.041137	0.025708	9
11	0.88677	6.9215	0.025512	0.017052	4
12	NaN	NaN	NaN	NaN	0
13	NaN	NaN	NaN	NaN	0
14	1.0794	2.2124	0.24297	6.2063e-17	4
15	0.32898	1.8659	0.02659	0.010358	5
16	-0.22219	4.2739	0.027223	0.014699	12
17	-0.32343	5.9072	0.032463	0.022956	11
18	-0.43028	7.1176	0.03641	0.02564	4
19	-1.3809	5.8505	0.029835	0.016253	13
20	-1.5315	4.1181	0.023488	0.011099	20
21	-1.3668	2.4475	0.033977	0.022727	13
Mean	**-**	**-**	**0.0459**	**-**	**7.7619**

B.2 Measurement Results for the Octagonal Antenna

Table B.3: Complete measurement data for the LOS test with octagonal antenna. Note that all measurements, except location and number of measurements, are in meters.

Location	Mean X	Mean Y	Error	Deviation	# of measurements
1	3.3067	0.82984	0.035129	0.01454	37
2	3.3452	0.38683	0.031874	0.01541	38
3	3.3265	0.042743	0.030354	0.017686	38
4	3.3395	-0.38644	0.030475	0.016588	37
5	3.3228	-0.79946	0.028331	0.015525	37
6	2.9748	-0.77786	0.031183	0.015729	38
7	2.9982	-0.44275	0.031407	0.01575	37
8	2.9358	0.060055	0.027131	0.018578	38
9	2.9849	0.41344	0.030512	0.019075	37
10	2.9632	0.81183	0.031052	0.016084	37
11	2.5476	0.82688	0.029754	0.017435	37
12	2.5691	0.41078	0.029727	0.014114	37
13	2.5422	0.065727	0.02799	0.016631	38
14	2.605	-0.47523	0.028192	0.014993	38
15	2.5696	-0.76112	0.038968	0.016165	38
16	2.2427	-1.8763	0.031882	0.015132	38
17	2.1904	-1.495	0.03525	0.020365	37
18	2.1568	-1.1526	0.031081	0.018714	37
19	2.2338	-0.84247	0.025486	0.016246	38
20	2.2269	-0.37083	0.033288	0.016171	37
21	2.2552	-0.00043309	0.034057	0.015142	38
22	2.237	0.44025	0.033725	0.016963	37
23	2.2355	0.84011	0.029378	0.015593	38
24	2.2186	1.1671	0.042264	0.017906	39
25	2.2245	1.4445	0.034593	0.015759	38
26	2.2891	1.8584	0.037666	0.016582	38
27	1.9186	1.7788	0.035889	0.02011	38
28	1.8904	1.4187	0.033898	0.015918	38
29	1.8506	1.1318	0.035047	0.015491	38
30	1.7893	0.82144	0.027599	0.017328	38
31	1.815	0.44858	0.029744	0.016915	38
32	1.8046	0.0056627	0.029038	0.016222	38
33	1.8642	-0.44257	0.027493	0.014753	37
34	1.8532	-0.81665	0.034757	0.017876	38
35	1.8339	-1.2615	0.036794	0.019827	38
36	1.7994	-1.4957	0.032329	0.01612	39
37	1.822	-1.8353	0.03302	0.017881	38

Table B.3: Complete measurement data for the LOS test with octagonal antenna. Note that all measurements, except location and number of measurements, are in meters.

Location	Mean X	Mean Y	Error	Deviation	# of measurements
38	1.5212	-1.9722	0.12172	0.065815	37
39	1.5282	-1.6706	0.035599	0.01782	37
40	1.4708	-1.209	0.037903	0.018503	38
41	1.4514	-0.83732	0.031039	0.015855	38
42	1.4459	-0.39253	0.036856	0.017742	39
43	1.3771	0.041189	0.031396	0.014506	37
44	1.2689	0.43528	0.036771	0.024586	37
45	1.4384	0.78632	0.036181	0.017539	38
46	1.4456	1.098	0.033041	0.018071	38
47	1.4959	1.4187	0.037925	0.016401	38
48	1.5374	1.7647	0.038504	0.021712	37
49	1.1039	1.7651	0.039776	0.021442	37
50	1.1301	1.3898	0.031033	0.016335	37
51	1.1379	1.0646	0.034062	0.012428	38
52	0.90596	0.74872	0.032287	0.016929	38
53	1.1001	0.44241	0.04877	0.026495	38
54	0.98718	0.044952	0.037984	0.021145	38
55	0.96969	-0.36579	0.025481	0.01415	37
56	1.0395	-0.73952	0.030887	0.016269	38
57	1.047	-1.0329	0.03711	0.019144	37
58	0.98749	-1.3585	0.040728	0.022374	38
59	0.96666	-1.5765	0.04257	0.022375	37
60	0.68043	-1.7593	0.044909	0.026582	38
61	0.69405	-1.4451	0.036203	0.019249	37
62	0.66643	-1.0829	0.029324	0.020299	36
63	0.64434	-0.70929	0.035095	0.016481	38
64	0.6011	-0.33831	0.026429	0.014567	38
65	0.62331	0.0020612	0.033076	0.016876	37
66	0.68071	0.36132	0.03158	0.013039	38
67	0.61388	0.70211	0.039756	0.018645	37
68	0.77115	1.0962	0.11394	0.079067	38
69	0.77084	1.4369	0.04238	0.028104	38
70	0.73379	1.792	0.044433	0.018944	38
Mean	**-**	**-**	**0.0363**	**-**	**37.6429**

Table B.4: Full measurement data regarding the NLOS test for octagonal antenna. Note that all values, except location and number of measurements, are in meters.

Location	Mean X	Mean Y	Error	Deviation	# of measurements
1	1.9643	1.7282	0.28469	0.12712	37
2	2.1233	2.1965	0.033446	0.018987	37
3	1.9151	2.9966	0.025476	0.011298	27
4	2.1836	3.3592	0.040858	0.022728	12
5	2.2395	3.8816	0.11521	0.073327	36
6	2.1512	4.4505	0.15308	0.071597	34
7	2.1426	5.0351	0.096262	0.075049	7
8	1.9617	5.719	0.026382	0.014129	33
9	1.9677	6.3106	0.02416	0.01635	38
10	1.9857	6.831	0.029237	0.013066	38
11	NaN	NaN	NaN	NaN	0
12	NaN	NaN	NaN	NaN	0
13	NaN	NaN	NaN	NaN	0
14	0.85425	2.3257	0	0	4
15	0.15693	1.9255	0.037281	0.019609	25
16	-0.26317	4.2888	0.034181	0.018492	37
17	-0.32201	5.9497	0.048	0.017587	30
18	-0.37421	7.2456	0.25752	0.30392	21
19	-1.3382	5.8977	0.033827	0.020294	37
20	-1.6013	4.121	0.028816	0.01487	37
21	-1.3743	2.4692	0.036933	0.021499	38
Mean	**-**	**-**	**0.0725**	**-**	**25.1429**

B.3 Measurement Results for the Vivaldi Antenna

Table B.5: Complete measurement data for the Vivaldi antenna in LOS setup. Note that all values, except location and number of measurements, are in meters.

Location	Mean X	Mean Y	Error	Deviation	# of measurements
1	3.4898	0.76961	0.037177	0.017167	37
2	3.5708	0.42459	0.044817	0.022037	38
3	3.403	-0.0057919	0.095684	0.071548	38
4	3.0749	-0.45703	0.037625	0.021726	38
5	3.1694	-0.79287	0.03752	0.021672	38
6	2.7252	-0.77097	0.030808	0.017998	38
7	2.7206	-0.4671	0.036837	0.018182	40
8	3.1402	-0.015937	0.16608	0.11189	37
9	3.3093	0.41125	0.030995	0.015309	38
10	3.1792	0.76337	0.037101	0.019223	37
11	2.6332	0.73988	0.1566	0.076402	38
12	2.8707	0.3771	0.035165	0.014605	37
13	2.6222	-0.055349	0.026197	0.015646	38
14	2.5201	-0.44895	0.03108	0.013746	38
15	2.5341	-0.73257	0.030765	0.018085	36
16	2.1248	-1.8188	0	0	4
17	NaN	NaN	NaN	NaN	0
18	2.0416	-1.1468	0.046938	0.028131	25
19	2.0488	-0.72256	0.032655	0.019524	36
20	1.9696	-0.42742	0.035294	0.015472	38
21	1.876	-0.084449	0.038353	0.016719	38
22	2.3783	0.39288	0.03105	0.016453	38
23	2.1856	0.697	0.025686	0.015066	38
24	2.0956	1.0982	0.029912	0.014254	37
25	2.0551	1.3874	0.034682	0.018921	38
26	2.1909	1.8892	0.03089	0.016849	38
27	1.7877	1.8982	0.039463	0.020793	38
28	1.7614	1.4554	0.041266	0.024292	38
29	1.6907	1.0439	0.036289	0.018924	38
30	1.7243	0.73886	0.034696	0.01965	38
31	1.5971	0.34682	0.030164	0.019483	38
32	1.8259	-0.089588	0.033931	0.014306	37
33	1.7084	-0.43093	0.027592	0.016393	37
34	1.6235	-0.85462	0.0336	0.01522	38
35	1.5113	-1.479	0.069584	0.038299	38
36	1.7684	-1.2831	0.035386	0.024244	29
37	1.7905	-1.6894	0.039258	0.021261	20
38	1.2777	-1.9647	0.015982	0.0051207	4
39	NaN	NaN	NaN	NaN	0

Table B.5: Complete measurement data for the Vivaldi antenna in LOS setup. Note that all values, except location and number of measurements, are in meters.

Location	Mean X	Mean Y	Error	Deviation	# of measurements
40	1.1464	-1.3513	0.070456	0.04148	38
41	1.2177	-0.91831	0.032943	0.018809	37
42	1.2559	-0.48373	0.029843	0.01535	38
43	1.329	0.0025319	0.032541	0.015149	38
44	1.3259	0.24723	0.029441	0.015069	37
45	1.3395	0.68047	0.031386	0.018487	37
46	1.3181	1.1474	0.032429	0.02103	37
47	1.3794	1.4742	0.031841	0.016153	37
48	1.4153	1.8003	0.031409	0.015489	38
49	1.0296	1.7747	0.041501	0.024821	38
50	0.95612	1.4067	0.037858	0.018662	38
51	0.92503	1.0475	0.037019	0.019458	38
52	0.892	0.70949	0.029742	0.01541	38
53	0.96347	0.32038	0.032042	0.020551	37
54	1.0046	-0.063534	0.029513	0.01735	38
55	0.84765	-0.49169	0.032902	0.017317	37
56	0.85728	-0.86074	0.042491	0.024184	38
57	0.96459	-1.1361	0.037611	0.021566	32
58	0.91274	-1.5395	0.038636	0.024544	33
59	0.84432	-2.0344	0.044832	0.028239	38
60	0.4307	-2.1097	0.053675	0.032622	38
61	0.46548	-1.6173	0.050821	0.024043	38
62	0.48299	-1.1106	0.037113	0.023394	38
63	0.5124	-0.66427	0.041046	0.020632	38
64	0.51459	-0.46621	0.033071	0.017155	38
65	0.62951	-0.16149	0.033374	0.01515	38
66	0.51477	0.31428	0.027356	0.016083	38
67	0.54504	0.74906	0.034281	0.017118	37
68	0.57114	1.1234	0.042898	0.022883	38
69	0.64216	1.3923	0.041854	0.026335	38
70	0.66697	1.7868	0.037664	0.022348	38
Mean	**-**	**-**	**0.0402**	**-**	**34.9714**

Table B.6: The entire measurement data for the Vivaldi antenna in the NLOS setup. Note that all values, except for location and number of measurements, are in meters.

Location	Mean X	Mean Y	Error	Deviation	# of measurements
1	2.4076	1.3494	0.03886	0.020699	25
2	2.7553	1.7916	0	0	4
3	1.9801	2.8443	0	0	4
4	2.0166	3.3399	0.024437	0.0072491	4
5	NaN	NaN	NaN	NaN	0
6	NaN	NaN	NaN	NaN	0
7	NaN	NaN	NaN	NaN	0
8	NaN	NaN	NaN	NaN	0
9	NaN	NaN	NaN	NaN	0
10	NaN	NaN	NaN	NaN	0
11	NaN	NaN	NaN	NaN	0
12	NaN	NaN	NaN	NaN	0
13	0.58389	4.1426	0.05148	0.026355	4
14	1.1187	2.3311	0.021326	0	4
15	NaN	NaN	NaN	NaN	0
16	-0.59761	4.1598	0.035219	0.017571	34
17	NaN	NaN	NaN	NaN	0
18	NaN	NaN	NaN	NaN	0
19	-1.3968	6.3166	0.017544	0.0061962	4
20	-1.5876	4.1091	0.046161	0.028035	6
21	-1.6706	2.3069	0.043879	0.017244	9
Mean	**-**	**-**	**0.0279**	**-**	**4.6667**

B.4 Measurement Results for the 10ppm Oscillator

Table B.7: The full measurement data for the Kyocera 10ppm oscillator together with the reference antenna for the LOS environment. Note that all values, except for location and number of measurements, are in meters.

Location	Mean X	Mean Y	Error	Deviation	# of measurements
1	3.29	0.71257	0.033764	0.018198	37
2	3.2544	0.39669	0.033133	0.017854	37
3	3.2388	0.031462	0.041308	0.020763	37
4	3.2849	-0.29966	0.032588	0.018339	37
5	3.2245	-0.80632	0.043727	0.016798	37
6	2.8922	-0.75195	0.030545	0.01488	37

Table B.7: The full measurement data for the Kyocera 10ppm oscillator together with the reference antenna for the LOS environment. Note that all values, except for location and number of measurements, are in meters.

Location	Mean X	Mean Y	Error	Deviation	# of measurements
7	2.9488	-0.32246	0.035934	0.019854	37
8	2.9129	0.077166	0.032582	0.015595	37
9	2.9187	0.42275	0.03096	0.016269	37
10	2.915	0.78028	0.034426	0.015937	37
11	2.5864	0.80171	0.037218	0.016464	37
12	2.569	0.43676	0.027791	0.013054	37
13	2.5947	0.10703	0.027571	0.017669	36
14	2.6089	-0.35383	0.034072	0.016307	37
15	2.5742	-0.75885	0.036377	0.013885	37
16	2.1184	-1.8739	0.036057	0.016569	35
17	2.1291	-1.5168	0.032628	0.0161	36
18	2.1568	-1.1446	0.037988	0.020287	38
19	2.1801	-0.85585	0.035435	0.022409	37
20	2.1297	-0.32933	0.030491	0.016939	36
21	2.1523	0.035267	0.028152	0.014954	37
22	2.1733	0.5101	0.030178	0.015359	25
23	2.1753	0.83882	0.033559	0.019657	37
24	2.2128	1.1744	0.031025	0.017647	38
25	2.2594	1.4761	0.030707	0.015485	37
26	2.2746	1.8261	0.033253	0.015307	37
27	1.87	1.7987	0.038755	0.021854	38
28	1.856	1.4317	0.037709	0.022227	37
29	1.8086	1.1286	0.044238	0.024492	37
30	1.8172	0.8757	0.031499	0.015663	34
31	1.7884	0.43781	0.032702	0.013682	37
32	1.7772	0.017602	0.026118	0.013267	37
33	1.7867	-0.43952	0.027733	0.011948	38
34	1.7478	-0.74097	0.038337	0.016581	37
35	1.7546	-1.1805	0.025538	0.012689	38
36	1.7343	-1.5359	0.030016	0.018087	37
37	1.7471	-1.9017	0.039714	0.018019	37
38	1.3645	-1.9129	0.03393	0.019278	32
39	1.4014	-1.5139	0.04099	0.02113	36
40	1.4041	-1.1376	0.03044	0.01368	37
41	1.441	-0.82105	0.025153	0.013615	37
42	1.3734	-0.37856	0.029804	0.016186	38
43	1.3244	0.039273	0.039965	0.022329	36
44	1.3671	0.41699	0.033604	0.017059	37
45	1.4525	0.83669	0.035747	0.023356	38
46	1.4999	1.153	0.034881	0.017554	37
47	1.4992	1.444	0.03996	0.017177	37

Table B.7: The full measurement data for the Kyocera 10ppm oscillator together with the reference antenna for the LOS environment. Note that all values, except for location and number of measurements, are in meters.

Location	Mean X	Mean Y	Error	Deviation	# of measurements
48	1.4865	1.7874	0.032509	0.019556	37
49	1.1385	1.8182	0.036012	0.0166	37
50	1.1216	1.4657	0.036993	0.019074	38
51	1.105	1.1182	0.034318	0.015174	37
52	1.0417	0.75687	0.03188	0.01592	38
53	0.94178	0.42245	0.034292	0.016707	38
54	0.90511	0.057312	0.031134	0.013358	37
55	0.93527	-0.30354	0.030709	0.016127	38
56	0.99596	-0.70289	0.028502	0.014975	37
57	1.0624	-1.0921	0.02977	0.015924	37
58	1.0173	-1.4362	0.037107	0.018108	37
59	0.99424	-1.7632	0.033881	0.016713	33
60	0.59833	-1.718	0.039562	0.019121	37
61	0.70716	-1.3613	0.04056	0.023292	37
62	0.64014	-1.0272	0.0388	0.016507	38
63	0.63006	-0.66842	0.03771	0.021147	37
64	0.60294	-0.32356	0.030108	0.019876	37
65	0.57298	0.048942	0.036052	0.018993	37
66	0.56815	0.40062	0.029565	0.017071	37
67	0.59141	0.74533	0.037373	0.021873	37
68	0.74791	1.093	0.044872	0.021669	37
69	0.7047	1.4352	0.040135	0.021373	37
70	0.73115	1.7999	0.033445	0.018369	37
Mean	**-**	**-**	**0.0342**	**-**	**36.7286**

Table B.8: Complete measurement data for the Kyocera 10ppm oscillator together with the reference antenna. Note that all values, except for the location and number of measurements, are in meters.

Location	Mean X	Mean Y	Error	Deviation	# of measurements
1	2.2716	1.5393	0.12562	0.093859	26
2	2.1019	2.2865	0.02649	0.015962	17
3	2.0117	2.9695	0.014618	0.0077835	19
4	2.2	3.3923	0.03622	0.023047	21
5	NaN	NaN	NaN	NaN	0
6	2.0984	4.5513	0.031696	0.015981	20
7	2.0758	5.1052	0.032007	0.015321	14
8	2.0697	5.7665	0.030336	0.011643	16
9	1.9803	6.3297	0.10685	0.11167	21
10	2.0233	6.8746	0.035803	0.020483	23
11	NaN	NaN	NaN	NaN	0
12	NaN	NaN	NaN	NaN	0
13	NaN	NaN	NaN	NaN	0
14	NaN	NaN	NaN	NaN	0
15	0.29921	1.903	0.19716	0.092492	28
16	NaN	NaN	NaN	NaN	0
17	-0.27465	5.859	0.02307	0.012088	8
18	NaN	NaN	NaN	NaN	0
19	-1.4226	5.8087	0.046896	0.026778	13
20	-1.5209	4.1068	0.034301	0.0098353	4
21	-1.3655	2.3264	0.028866	0.01596	5
Mean	**-**	**-**	**0.0550**	**-**	**11.1905**

B.5 Measurement Results for the 2ppm Oscillator

Table B.9: Full measurement data for the Taitien 2ppm oscillator along with the reference antenna in LOS setup. Note that all values, except for location and number of measurements, are in meters.

Location	Mean X	Mean Y	Error	Deviation	# of measurements
1	3.414	0.68025	0.029065	0.015742	22
2	3.4003	0.37777	0.032671	0.017437	33
3	3.3926	-0.017457	0.036543	0.017302	36
4	3.4501	-0.31584	0.028944	0.014662	35
5	3.399	-0.84163	0.031834	0.01804	33
6	3.0537	-0.79125	0.030178	0.015491	34

Table B.9: Full measurement data for the Taitien 2ppm oscillator along with the reference antenna in LOS setup. Note that all values, except for location and number of measurements, are in meters.

Location	Mean X	Mean Y	Error	Deviation	# of measurements
7	3.0732	-0.3441	0.030164	0.013593	37
8	3.0211	0.051435	0.029186	0.014296	38
9	3.0114	0.41599	0.029985	0.018685	36
10	3.042	0.75416	0.037411	0.020707	36
11	2.5796	0.75996	0.035256	0.018519	37
12	2.5197	0.42262	0.036241	0.017165	36
13	2.5429	0.086799	0.03393	0.015148	35
14	2.5823	-0.38368	0.029071	0.01482	37
15	2.5978	-0.78715	0.036181	0.022391	34
16	2.3056	-1.9046	0.038435	0.024864	35
17	2.2482	-1.5329	0.03018	0.015097	29
18	2.2345	-1.1551	0.040616	0.022177	35
19	2.2811	-0.86934	0.040738	0.026723	37
20	2.2158	-0.3734	0.044452	0.027455	37
21	2.1614	0.00056153	0.036037	0.019372	37
22	2.1533	0.49106	0.030604	0.014976	32
23	2.1574	0.81533	0.03503	0.023082	38
24	2.1868	1.1305	0.032199	0.017236	36
25	2.2355	1.4431	0.035143	0.019776	37
26	2.2399	1.8096	0.03468	0.021747	36
27	1.8131	1.7878	0.036061	0.022972	27
28	1.8145	1.4145	0.050251	0.021935	34
29	1.8081	1.0971	0.027251	0.015118	38
30	1.8526	0.80432	0.029685	0.016237	37
31	1.8792	0.4441	0.037663	0.018206	38
32	1.836	0.011034	0.038341	0.017461	37
33	1.7829	-0.47456	0.038162	0.015506	24
34	1.7349	-0.77889	0.038671	0.01713	31
35	1.8561	-1.2054	0.032005	0.019244	30
36	1.9121	-1.574	0.033152	0.0186	30
37	1.92	-1.9512	0.040267	0.023248	33
38	1.5759	-1.922	0.035403	0.01684	35
39	1.4898	-1.5637	0.035034	0.021771	31
40	1.4038	-1.1981	0.035197	0.014906	32
41	1.4123	-0.84897	0.03256	0.017211	29
42	1.4095	-0.39102	0.032552	0.018807	35
43	1.4127	0.013444	0.035606	0.019539	35
44	1.443	0.41356	0.030553	0.012742	37
45	1.4786	0.80038	0.028362	0.01396	37
46	1.4869	1.1083	0.027594	0.016392	36
47	1.5004	1.4184	0.040816	0.016501	37

Table B.9: Full measurement data for the Taitien 2ppm oscillator along with the reference antenna in LOS setup. Note that all values, except for location and number of measurements, are in meters.

Location	Mean X	Mean Y	Error	Deviation	# of measurements
48	1.4489	1.7826	0.036774	0.013781	37
49	1.0998	1.8032	0.039358	0.0216	37
50	1.0853	1.4547	0.044377	0.017787	37
51	1.1183	1.087	0.032433	0.012889	37
52	1.0819	0.76061	0.037179	0.018262	38
53	1.0464	0.40258	0.0336	0.016272	35
54	1.0327	0.037595	0.03498	0.015155	36
55	1.0228	-0.33874	0.032781	0.015978	32
56	1.0535	-0.73883	0.032297	0.016161	28
57	1.0437	-1.08	0.032154	0.016806	28
58	1.0417	-1.477	0.035788	0.016824	30
59	1.133	-1.8023	0.037102	0.020339	35
60	0.67736	-1.7252	0.035458	0.018627	29
61	0.66106	-1.3787	0.036963	0.013795	30
62	0.65358	-1.0602	0.031941	0.017702	34
63	0.66694	-0.70832	0.036894	0.014358	29
64	0.65561	-0.35735	0.037506	0.022492	28
65	0.62924	-0.0019904	0.035836	0.017741	36
66	0.65324	0.37305	0.03282	0.017268	37
67	0.69402	0.74973	0.031722	0.017602	37
68	0.70172	1.0979	0.041348	0.020576	37
69	0.73769	1.4434	0.035632	0.020309	37
70	0.68752	1.8259	0.043559	0.026457	38
Mean	**-**	**-**	**0.0350**	**-**	**34.1857**

Table B.10: Complete measurement data for the Taitien 2ppm oscillator together with the reference antenna in the NLOS setup. Note that all values, except for location and number of measurements, are in meters.

Location	Mean X	Mean Y	Error	Deviation	# of measurements
1	2.2485	1.5982	0.19722	0.099001	29
2	2.143	2.3006	0.037593	0.017272	34
3	2.0152	3.0134	0.02797	0.018203	27
4	2.2893	3.3793	0.042287	0.01927	29
5	2.533	3.7163	0.016493	0.012019	6
6	2.2146	4.5118	0.033082	0.022678	28
7	2.11	5.1591	0.03317	0.018971	27
8	2.0967	5.7611	0.030855	0.020027	25
9	1.9899	6.4365	0.030842	0.017031	30

Table B.10: Complete measurement data for the Taitien 2ppm oscillator together with the reference antenna in the NLOS setup. Note that all values, except for location and number of measurements, are in meters.

Location	Mean X	Mean Y	Error	Deviation	# of measurements
10	2.0597	6.9298	0.042569	0.024204	32
11	NaN	NaN	NaN	NaN	0
12	NaN	NaN	NaN	NaN	0
13	1.6094	5.8531	0.071984	0.099311	16
14	NaN	NaN	NaN	NaN	0
15	-0.045471	2.0994	0	0	4
16	-0.024236	4.5957	0	0	4
17	-0.045263	6.4298	0.17636	0.17737	13
18	NaN	NaN	NaN	NaN	0
19	-1.4395	5.7821	0.053996	0.03023	15
20	-1.5637	4.064	0.029589	0.019659	31
21	-1.2114	2.3021	0.03303	0.014988	25
Mean	**-**	**-**	**0.0504**	**-**	**17.8571**

B.6 Measurement Results for the 2ppm Oscillator together with the Octagonal Antenna

Table B.11: The entire measurement data for Taitien 2ppm oscillator together with the Octagonal antenna in the NLOS seup. Note that all values, except location and number of measurements, are in meters.

Location	Mean X	Mean Y	Error	Deviation	# of measurements
1	2.3322	1.4509	0.238	0.11849	38
2	2.1672	2.1962	0.035164	0.015434	37
3	2.0177	2.9678	0.029867	0.013638	36
4	2.368	3.3301	0.038311	0.030143	37
5	2.5797	3.6873	0.052084	0.054814	37
6	2.0872	4.6106	0.036005	0.016191	24
7	1.9971	5.2277	0.031779	0.01318	35
8	2.0328	5.7313	0.039105	0.020599	36
9	1.9976	6.373	0.032489	0.018034	37
10	1.9867	6.9071	0.042059	0.023258	34
11	NaN	NaN	NaN	NaN	0
12	1.3187	6.5514	0.0011905	0	4
13	1.3446	5.0499	0.22069	0.14605	37
14	0.87317	2.2595	0.039432	0.027081	26
15	0.16371	1.8445	0.048239	0.08737	37
16	-0.090996	4.3847	0.068304	0.044213	21

Table B.11: The entire measurement data for Taitien 2ppm oscillator together with the Octagonal antenna in the NLOS seup. Note that all values, except location and number of measurements, are in meters.

Location	Mean X	Mean Y	Error	Deviation	# of measurements
17	-0.22947	5.9239	0.10445	0.14888	36
18	NaN	NaN	NaN	NaN	0
19	-1.4991	5.7856	0.1689	0.15285	37
20	-1.5872	4.0784	0.033669	0.025737	32
21	-1.2272	2.2567	0.037975	0.019287	35
Mean	**-**	**-**	**0.0683**	**-**	**29.3333**